PRINCIPLES OF SURFACE-GUIDED PROTEIN ADSORPTION AND ASSEMBLY BEHAVIOR ON NANOPATTERNED BLOCK COPOLYMERS REVEALED AT THE SINGLE PROTEIN LEVEL

A Dissertation
submitted to the Faculty of the
Graduate School of Arts and Sciences
of Georgetown University
in partial fulfillment of the requirements for the
degree of
Doctor of Philosophy
in Chemistry

By

Tian Xie, M.S.

Washington, DC
April 1, 2019

PRINCIPLES OF SURFACE-GUIDED PROTEIN ADSORPTION AND ASSEMBLY BEHAVIOR ON NANOPATTERNED BLOCK COPOLYMERS REVEALED AT THE SINGLE PROTEIN LEVEL

Tian Xie, M.S.

Thesis Advisor: Dr. Jong-in Hahm, Ph.D.

ABSTRACT

Protein adsorption on polymeric material surfaces is a ubiquitous process that plays a crucial role in many essential fields such as medical devices, biosensors, and food processing. Understanding and manipulating protein adsorption at the nanoscopic level has become more important yet complicated with the continuous development of miniaturized biomaterials. To this end, I have employed phase-separating block copolymer (BCP) in recent studies as a convenient template to present periodically patterned nanodomains for controlling nanoscale protein patterning and understanding competitive protein adsorption behaviors. Tapping mode atomic force microscopy (AFM) was used in all the studies as a main characterization tool for direct imaging at the single protein level.

In Chapter One of this dissertation, I introduce the up-to-date background regarding protein adsorption fundamentals, protein nanopatterning templates, and protein adsorption investigation techniques. In Chapter Two, I present the distinct adsorption configurations of fibrinogen (Fg) proteins and the different organization behaviors between individual Fg molecules that are mediated by the changes in the periodicity and alignment of polystyrene-b-polymethylmethacrylate (PS-b-PMMA) nanodomains. I successfully created fully Fg-decorated BCP constructs analogous to two-dimensional Fg crystals and demonstrated the retained biofunctionality of the surface-bound Fg by using the Fg/BCP construct in Ca−P nanoparticle

nucleation/growth and microglia cell activation. In Chapter Three, I present the competitive adsorption characteristics of a model binary protein mixture of bovine serum albumin (BSA) and Fg examined on both the macroscopic homopolymer and nanoscopic BCP surfaces. I evaluated a series of adsorption and displacement processes by systematically varying the protein concentration and incubation time and reported a novel finding of nanointerfaces-induced protein residence time increase. In Chapter Four, I present a more detailed competitive adsorption study of immunoglobulin G (IgG) and Fg on PS-b-PMMA. I unambiguously revealed the adsorption, desorption, and replacement events of the same protein molecules via single protein tracking and determined the key protein adsorption pathways and dominant tendencies of sequential protein adsorption, which was further substantiated by Monte-Carlo simulations. The combined results of my research can promote the fundamental understanding of protein-surface interaction and the development of medical implants, biosensors, and tissue engineering materials.

ACKNOWLEDGEMENTS

First and foremost, I want to express my sincerest gratitude to my thesis advisor Dr. Jong-in Hahm for her constant support and guidance throughout my doctoral study. As a research advisor, she was always readily available with her profound scientific knowledge and great patience. As a professional role model, she has been inspiring me with her meticulous attitude towards science and high level of execution. I am truly fortunate and grateful to have her as my research mentor.

Additionally, I would like to give a big thanks to all the past and present group members in the Hahm group: Sheng Song, Manpreet Singh, Daniel Choi, Matt Hansen, Johnson Truong, David Cho, and Andrew Stoner for all the joyful and encouraging spirit they have brought to this family away from home. I am especially grateful to the senior group members for their help and advices along the way. I would never forget the inspiring moments and the laughter that echoed in Regents 534 when we were talking about science, life, and everything. Special thanks to Bok-eum Choi from the Yang group who shared the same office with us. Without her encouragement I would not have found what is the most precious in my life. Many thanks to my friends in the department, Fan Liu, Ransheng Ding, and Kunyu Zheng for their company and thank my roommates Mochi Liu, Xu Han, and Amit Bhandari for broadening my vision outside the field of science. I also want to thank my undergraduate students, particularly Patrick Mulcahey and Noah Kelleher, for devoting their time to my research and making all the publications possible.

I am deeply grateful to my parents for all their selfless love and understandings. I cannot thank them more for the sacrifices they have made and the care they have provided throughout my pursuit of knowledge overseas. I would never been this close to my dream without their constant

support and mentorship. I also want to thank Rongfeng Zheng for bringing courage and purpose to my life at a time when things were tough for me.

Last but not least, I want to thank the two most important teachers in my childhood, Arthur Clarke and Jules Verne, who enlightened me about science and its fascinating nature, eventually leading me to this career path.

TABLE OF CONTENTS

1 Backgrounds and Introductions 1

1.1 Protein Adsorption at Material Surfaces 1

1.1.1 Biomedical Relevance of Protein Adsorption 1

1.1.2 Properties of Protein and Material Surface that Affect Protein Adsorption 3

1.2 Protein Adsorption and Patterning at Nanoscale 8

1.2.1 The Trend of Biomaterial Miniaturization 8

1.2.2 Top-down Approaches for Protein Nanopatterning 9

1.2.3 Block Copolymers as Protein Nanopatterning and Adsorption Study Template 11

1.3 Characterization Techniques in Protein Adsorption Studies 16

1.3.1 Common Protein Adsorption Detection Methods 16

1.3.2 Atomic Force Microscopy for Protein Imaging 18

2 Surface Assembly Configurations and Packing Preferences of Fibrinogen Mediated by the Periodicity and Alignment Control of Block Copolymer Nanodomains 22

2.1 Introductions 22

2.2 Results and Discussion 23

2.2.1 Fibrinogen Structure 23

2.2.2 Polymeric Surfaces under Investigation 25

2.2.3 Adsorption Characteristics of Isolated Fibrinogen at Low Concentrations 27

2.2.4 Surface Packing of Crowded Fibrinogen at Higher Concentrations 32

2.2.5 Closer Look at Local and Extended Assembly Behavior of Fibrinogen 34

2.2.6 Effect of BCP Surface Periodicity on Fibrinogen Coverage 36

2.2.7 Effect of BCP Surface Alignment on Fibrinogen Coverage 39

2.2.8 Side-on versus End-on Surface Filling Geometry of Fibrinogen 41

2.2.9 Calcium phosphate NP Nucleation and Growth on Fg/BCP Scaffold 44

2.2.10 Fg/BCP in Microglia Cell Activation 47

2.3 Conclusions 48

2.4 Methods 49

2.4.1 Preparation of Polymeric Substrates 49

2.4.2 Preparation of Fibrinogen -Bound Substrates 52

2.4.3 Calcium phosphate Nanoparticle Nucleation and Growth 52

2.4.4 Microglia Cell Activation 52

2.4.5 Characterization 53

3 Ascertaining effects of nanoscale polymeric interfaces on competitive protein adsorption at the individual protein level 55

3.1 Introduction 55

3.2 Experimental Section 56

3.3 Results and Discussion 57

3.3.1 Physical and Chemical Characteristics of the Proteins and Polymeric Surfaces 57

3.3.2 Various Time-lapse Phases of the Binary Protein Adsorption 61

3.3.3 Time-resolved Protein Adsorption on PS and PS-b-PMMA with Varying Concentrations 66

3.3.4 Time Associated with Bovine Serum Albumin to Fibrinogen Transition on Polystyrene Versus PS-b-PMMA 73

3.3.5 Understanding the Prolonged Residence Time and The Role of Nanointerfaces 77

3.4 Summary 80

4 Revealing the Principal Attributes of Protein Adsorption on Block Copolymer Surfaces with Direct Experimental Evidence at The Single Protein Level 82

4.1 Introduction 82

4.2 Results and Discussion 83

4.2.1 Structure of Model Proteins 83

4.2.2 Atomic Force Microscopy Tracking of Individual Proteins 84

4.2.3 Two-Stage Tracking of Individual Proteins 86

4.2.4 Five Common Competitive Adsorption Events 88

4.2.5 Three Stage Tracking of Individual Proteins 90

4.2.6 Dominant Protein Exchange Direction and Adsorption/Desorption Tendency 91

4.2.7 Post-Adsorption Protein Rearrangement 93

4.2.8 Protein Mobility on Surface and Self-Association Degree 96

4.2.9 Influence of Preadsorbed Surface on Subsequent Stage Protein Adsorption 98

4.2.10 MC Simulations 102

4.3 Summary 107

4.4 Methods 108

4.4.1 Experimental Method 108

4.4.2 Simulational Method 109

5 Conclusions and Future Outlooks 111

6 Bibliography 114

LIST OF FIGURES

Figure 1. Immune response process following biomaterial implantation 2

Figure 2. Illustration of the important protein and substrate properties that determines protein adsorption. 5

Figure 3. Schematics of a diblock copolymer molecule (top) and the four available equilibrium 12

Figure 4. Schematics and atomic force microscopy images showing various polymeric surfaces before and after IgG deposition 14

Figure 5. Schematic illustration of the two main atomic force microscopy operating modes 20

Figure 6. Schematic representations showing the different protein subdomains present in fibrinogen..... 24

Figure 7. Four types of block copolymer templates employed in my fibrinogen adsorption study are analyzed with atomic force microscopy whose micrographs display the characteristic nanodomain sizes and orientations specific to (A) DSA aligned PS-b-PMMA (dsa PS-b-PMMA), (B) PS-b-PMMA with the repeat spacing of the nanodomains smaller than the length of fibrinogen (sm PS-b-PMMA), (C) PS-b-PMMA with the repeat spacing of the nanodomains comparable to the fibrinogen length (com PS-b-PMMA), and (D) PS-r-PMMA with no nanodomains..... 27

Figure 8. Atomic force microscopy panels display typical fibrinogen adsorption behaviors on the three well-defined diblock copolymer surfaces of PS-*b*-PMMA..... 29

Figure 9. Overlaid atomic force microscopy topography and phase panels display the main adsorption configurations of the surface-bound fibrinogen found on (A) com PS-*b*-PMMA, (B) sm PS-*b*-PMMA, and (C) dsa PS-*b*-PMMA..... 32

Figure 10. Atomic force microscopy panels display typical fibrinogen adsorption behaviors on the well-defined BCP surfaces upon protein deposition at higher concentrations..... 33

Figure 11. The overlaid atomic force microscopy topography and phase panels display the preferred assembly behavior of nearby fibrinogen molecules in the (left) TP and (right) SP‖ configuration on sm PS-b-PMMA 35

Figure 12. Atomic force microscopy topography panels display fibrinogen molecules adsorbed on the PS-r-PMMA surface at protein concentrations of (A) 2.5, (B) 12.5, (C) 25, and (D) 50 μg/mL 37

Figure 13. Atomic force microscopy topography images show both the large scale and zoomed-in frame views of fibrinogen molecules tightly packing on the polystyrene domains of the (A) com PS-*b*-PMMA and (B) dsa PS-*b*-PMMA surface 42

Figure 14. Atomic force microscopy topography panels show that calcium phosphate NPs preferentially nucleate and grow on the fibrinogen assembled areas of the com PS-*b*-PMMA template..... 46

Figure 15. The data shown in the atomic force microscopy phase panel display calcium phosphate NPs formed on com PS-b-PMMA without any surface-bound fibrinogen..... 46

Figure 16. Primary mouse microglial cells grown on (A) com PS-*b*-PMMA and (B) 25 μg/mL fibrinogen-deposited com PS-*b*-PMMA were immunostained for DAPI (blue), iNOS (green), and CD11b (red)..... 48

Figure 17. The colored ribbon structures show the two proteins under study, bovine serum albumin and fibrinogen 58

Figure 18. The series of representative atomic force microscopy panels display the step-by-step views of the four key protein adsorption stages examined by using a mixture of bovine serum albumin and fibrinogen exposed on the PS homopolymer surface 63

Figure 19. Fluorescence intensity obtained from noncompetitive (blue, 5 g/mL fluorescein isothiocyanate-labeled bovine serum albumin (FITC-BSA)) and competitive (red, 5 g/mL FITC-BSA + 0.5 g/mL fibrinogen) adsorption tests on PS-b-PMMA 65

Figure 20. The representative atomic force microscopy frames capture various time-dependent adsorption stages of the binary protein mixture on the PS homopolymer surface 68

Figure 21. The representative atomic force microscopy frames display various adsorption stages from the competitive bovine serum albumin /fibrinogen adsorption onto the PS-*b*-PMMA surface, profiling the time-lapse views of the initially bovine serum albumin-dominant phase transitioning to the fibrinogen-dominant phase over time at different concentrations of the bovine serum albumin/fibrinogen protein mixture 69

Figure 22. Typical atomic force microscopy panels of 500 nm × 500 nm in scan size are displayed in order to show larger views of the representative bovine serum albumin and fibrinogen adsorption behavior corresponding to each polymeric platform, protein mixture concentration, and incubation time specified in the images 71

Figure 23. Atomic force microscopy topography (top) and phase (bottom) panels of 50 g/ml fibrinogen deposited under an identical non-competitive deposition condition onto a (a) PS homopolymer and (b) PS-b-PMMA diblock copolymer surface 72

Figure 24. The dominant occurrence profiles of the bovine serum albumin and fibrinogen proteins adsorbed on the PS-*b*-PMMA block copolymer surfaces are charted as a function of time at various protein concentrations as indicated in the legend 74

Figure 25. The colored bar graphs display the transitioning stages of the protein type found on the PS-*b*-PMMA and the PS templates as a function of time 76

Figure 26. Schematic illustrations displaying the sequential protein adsorption experiments on PS-b-PMMA 86

Figure 27. Atomic force microscopy phase images of representative data sets tracking individual proteins between different deposition steps for determination of distinct adsorption events associated with each protein. 87

Figure 28. The five representative pathways that are commonly found in sequential protein adsorption events 89

Figure 29. Representative atomic force microscopy images displaying the same PS-b-PMMA areas consecutively exposed to a protein solution of IgG (1st stage), fibrinogen (2nd stage), and IgG (3rd stage) 91

Figure 30. The representative atomic force microscopy phase scans display typical protein adsorption behaviors observed from the sequential exposure of a PS-b-PMMA surface to a solution containing IgG xx(1st stage), PBS (2nd stage), and fibrinogen (3rd stage) 93

Figure 31. Individual IgG molecules on a PS-b-PMMA surface were followed between different sequential adsorption treatments and their changes in height and width were analyzed 95

Figure 32. Preadsorbed surface-associated adsorption behavior identified from the sequential protein deposition experiment of IgG followed by fibrinogen..... 99

Figure 33. The protein adsorption behaviors found on neat versus preadsorbed PS-b-PMMA surfaces are summarized..... 101

Figure 34. Monte Carlo simulation results showing the bulk concentration-dependent protein adsorption onto an initially empty 2D box 104

Figure 35. Monte Carlo simulation outcomes showing large protein adsorption onto a 2D box preadsorbed with small proteins..... 106

LIST OF TABLES

Table 1. Four Different Polymeric Surfaces Used in the Fg Adsorption Study along with Their Surface Roughness and the Repeat Spacing Values of the Nanodomains[a] 25

Table 2. Number of Fibrinogen Molecules, Surface Density of Adsorbed Fibrinogen, and Protein Surface Coverage Found on the Different Polymeric Surfaces at Various Protein Concentrations[a] 38

Table 3. Ratios among the Three Fibrinogen Configurations of TP, $SP_{/\!/}$, and $SP_{\perp}$ Measured on the Different Polymeric Templates 41

Table 4. Key physical and chemical parameters of Bovine Serum Albumin and Fibrinogen are charted.. 59

1 Backgrounds and Introductions

1.1 Protein Adsorption at Material Surfaces

1.1.1 Biomedical Relevance of Protein Adsorption

Protein adsorption on material surfaces is a ubiquitous phenomenon which has relevance in many essential fields including biomedical devices, biosensing, food processing, and marine engineering. It is also a process of complication owing to the diverse and complex nature of protein and the broad range of material surfaces. The adsorption properties of the protein, such as rate, density, configuration, and functionality play a crucial role in determining the biocompatibility of the biomaterials and the performance of the analytical biodevices.

Particularly, when a protein containing fluid (e.g., blood, cell culture media) meets a solid material (e.g., implant, biosensor), nonspecific protein adsorption is the first process that occurs. Protein rapidly saturate the surface after the contact, and cells subsequently interact with the adsorbed protein layer instead of directly interacting with the materials surface itself. Figure 1 illustrates a typical foreign body reaction process after implantation of biomaterial. As a result, the consequent cell growth and the series of immune responses are dictated by the initially adsorbed proteins.[1,2] In this regard, understanding the adsorption behavior of protein on surfaces is a fundamental key to developing biomaterials of desired biological functionalities.

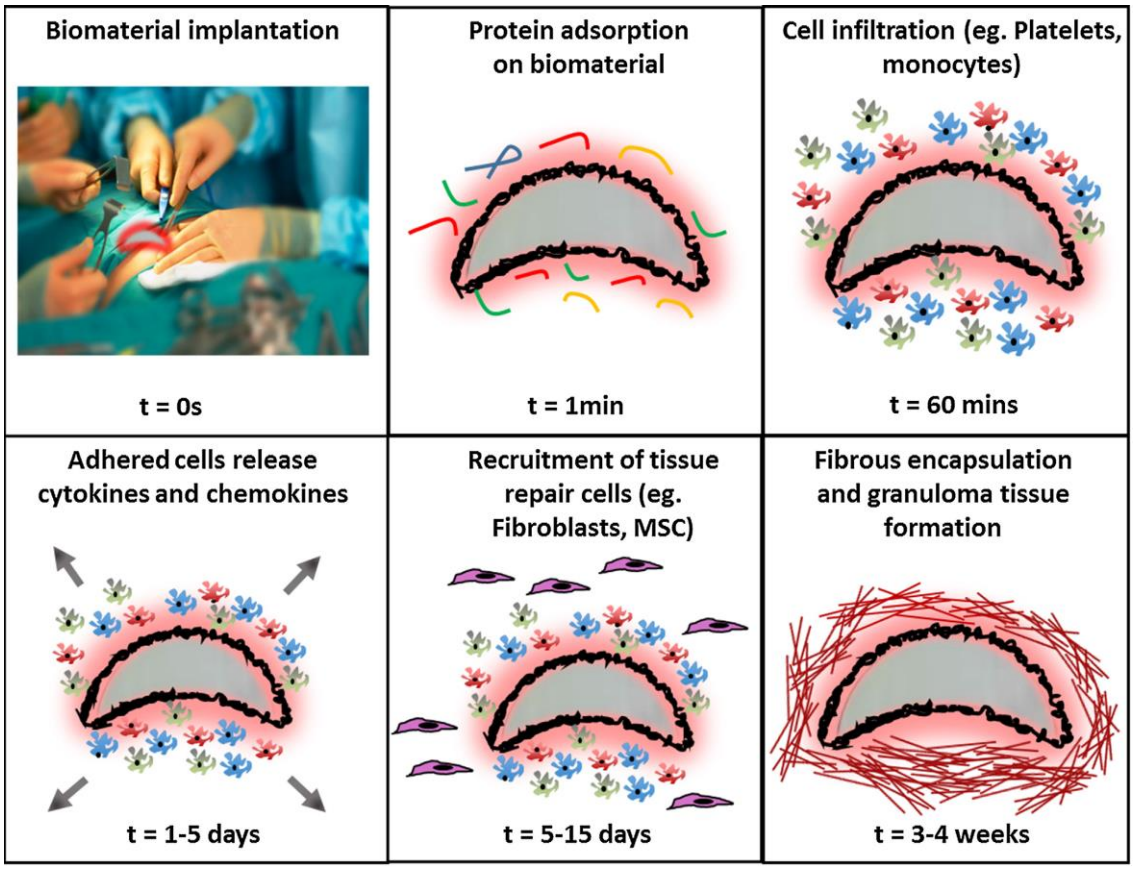

Figure 1. Immune response process following biomaterial implantation. Protein adsorption is the first step to occur at the initial contact between the biological system and the foreign material. Reproduced with permission from Ref.1.

In the past few decades, a tremendous amount of efforts has been put into controlling and manipulating protein adsorption on surfaces. A variety of materials with different protein adsorption properties have been developed. For example, materials that resist protein can be applied in most biomaterials, food packaging platforms, ultrafiltration membranes, and boat paints. On the other hand, materials that favor protein adsorption have their use in biosensing, tissue engineering, and chromatography. Surfaces with ordered chemical or physical patterns can guide the packing behavior of protein and generate protein arrays. To learn how to control and utilized these adsorption properties, one must understand the fundamental interactions between protein and the surface as well as the various factors that control protein adsorption behaviors.

1.1.2 Properties of Protein and Material Surface that Affect Protein Adsorption

As the most diverse biomolecules on earth, proteins exhibit a variety of distinctive structural and chemical characteristics. And as with constitutional complexity of the protein, the properties that determines the nonspecific interactions between protein and material surfaces is also various. Protein-surface interactions are driven by a combination of intermolecular forces including hydrophobic interaction, electrostatic interaction, hydrogen bonding, and van der Waals forces. The size, shape, surface charge, and structure stability of the protein all determine the adsorption behavior of the protein on surfaces. On the other hand, surface properties such as chemical composition, roughness, and topography as well can affect the adsorption result.

1.1.2.1 Protein Properties

Size and shape play a primary role in non-specific adsorption events for they determine the available binding sites on the protein exterior. For instance, larger proteins with more surface area typically have more sites to contact with the surface and are less likely to desorb once attached. In contrast, small proteins with higher diffusion rate are kinetically faster in the adsorption process and are easier to detach from the surface. As a result, a unique adsorption phenomenon may occur in a multicomponent protein adsorption environment: proteins that are smaller, more mobile, and more abundant tend to adsorb onto the surface first, and then are replaced by latter arriving, larger species with higher surface affinities over time. This competitive adsorption phenomenon was first observed in the 1960s by Vroman and Adams with diluted blood plasma[3,4] and is known as Vroman effect. Extensive research have been carried out in bulk scale of plasma proteins such as immunoglobulins and fibrinogen in hemostasis, thrombosis, and biomaterials.[5–9] Although the general process of Vroman exchange is well known and widely accepted, many aspects of the Vroman

effect, including the exact molecular mechanism underlying the process and the precise composition of the adsorbed protein layer from a multicomponent mixture, are still under active investigation.

Structure stability is another contributing factor that affect the adsorption behavior. proteins are macromolecules of high chemical complexity and structural flexibility. The structure and functionality of proteins are determined by their primary constituent, amino acid sequences, which are also diverse in many chemical properties (e.g., polarity, hydrophobicity, and isoelectric point). Accordingly, the uneven distribution of different amino acid residues at protein exteriors will result in a difference in local chemical environment on the protein surface and ultimately an overall amphiphilic characteristic of the protein molecule, as illustrated in Figure 2. The contact between protein and the surface will induce a free energy gain, and the amphiphilic nature of the protein will drive it to undergo conformational changes to reach a free energy minimum.[1011] Some proteins are known to unfold themselves and expose their hydrophobic cores to minimize surface energy by covering more area on the surface. [9,12–14] In this sense, proteins with less stable structure stability (i.e., "softer"), such as IgG or fibrinogen, are more likely to unfold and expose more binding sites. On the other hand, structural alteration are more difficult to happen to "harder" proteins such as lysozyme, β -Lactoglobulin, or α-Chymotrypsin.[15,16]

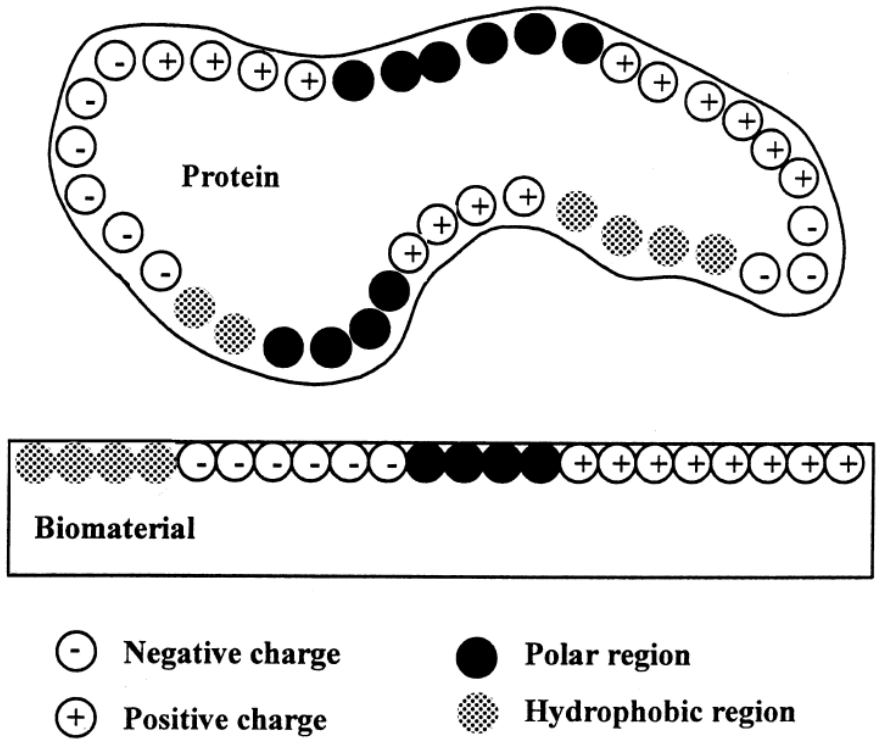

Figure 2. Illustration of the important protein and substrate properties that determines protein adsorption. Distribution of different charges and polarities on the protein surface results in an overall amphiphilic nature. Reproduced with permission from Ref. 17.

Regarding electrostatic interactions, the interaction between protein and charged surface is typically affected by the charged state of the protein. Protein surface charge is determined by the isoelectric point (pI) of the protein, which is defined as is the pH value that results in the protein having a net zero charge. Consequentially, the overall charge of the protein is sensitive to the pH of the surrounding solution. At this point, lateral interactions between charged protein themselves become important. It was found that protein adsorption is more pronounced at or near the isoelectric pH,[12,17,18] which may be due to the minimized protein-protein repulsion and the more amphiphilic charged state at protein surface. It is also found that a higher ionic strength and shorter Debye length can cause protein packing density to increase due to the hindered repulsion between like-charged proteins.[11]

A large body of protein adsorption studies have been reported from the ensemble perspective on macroscopic, homogeneous surfaces, however, protein-surface interactions at more detailed scales with more complex protein/surface systems have not been extensively investigated. Specifically, with regard to nanoscale protein adsorption, it is not known how the competitive adhesion behavior will be manifested on the surfaces of reduced dimensions and to what extent the macroscopic Vroman effect will scale down in nanoscale protein adsorption. Yet, a better understanding of the competitive protein adsorption characteristics at the nanoscale will be beneficial not only in advancing our fundamental knowledge but also in improving biomedical technology. Improved understanding of the competitive/cooperative adsorption behavior of proteins exhibited at the nanoscale may also result in new thermodynamic and kinetic information as well as the development of nanobiomaterials and nanobiosensors with novel functionalities. With this regard, I present in Chapter Three and Four my detailed investigations on the multicomponent protein adsorption behavior at nanopatterned surfaces.

1.1.2.2 Surface Properties

Surface properties play an equally important role in protein adsorption as protein properties. Surface hydrophobicity (or wettability) is one major factor that impacts protein adsorption process. In general, proteins tend to adsorb more readily to the more hydrophobic, non-polar surfaces to promote the release of surface-bound water and increase the entropy.[19–23] For hydrophilic surfaces, due to the strong water-surface interactions, a high density water layer can form on the surface. This may shield protein from approaching the surface and facilitate desroption.[24] Some has also postulated that non-polar surfaces may destabilize proteins, which promotes conformational changes and is beneficial for adsorption,[23] as mentioned in the previous section.

The topography of the surface also plays an important role in deciding protein adsorption behavior. Greater surface roughness typically leads to more surface area and present more contact

sites to the protein.[25–28] However, some studies have found that that this effect becomes less pronounced when the roughness reaches sub-protein level.[26,29–31] As for curved surfaces, the surface curvature can be another determining factor, as was demonstrated on nanoparticles[27] and nanowires.[32] In addition, at molecular scale, the steric repulsion effect from long polymer chains on the coated material surfaces can provide protein resistance properties. For example, polyethylene glycol (PEG) or polyethylene oxide (PEO) (depending on the molecular weight)[33,34] and many other polymer brushes are the common grafting polymers that are known with their protein resisting properties.[35–37]

The surface potential of a material influences the electrolyte solution that is adjacent to the surface by affecting the composition of ions and structure of water molecules, thereby determines protein adsorption.[17] Electrostatic interactions occur between charged groups and ions on the surface and the charged functional groups on the proteins, and can affect the density and conformation of the adsorbed proteins.[38–40] For example, Ca^{2+} and PO_4^{3-} are believed to be the binding sites on many bioceramic surfaces and provide major contribution to protein adsorption.[41–43]

Considering the amphiphilic and flexible nature of protein, it is reasonable to postulate that the adsorption behavior of protein would be different when meeting surface features that are comparable to the size of the protein. Therefore, surfaces that have nanotopography or nanopatterns can be a good tool to further exploit the interaction preferences of proteins. The following section of this chapter will be introducing the trending research of protein adsorption and patterning at nanoscale surfaces.

1.2 Protein Adsorption and Patterning at Nanoscale

1.2.1 The Trend of Biomaterial Miniaturization

The global market of biomaterials is expected to double in the next five years.[44] Accompanying the rapid growth of the biomaterial industry is the increasing demand for the development of biomaterials towards improved performance, high throughput, and miniaturization. In this context, a considerable amount of research interests has arisen in nanoscopic protein adsorption focusing on the behavior at the individual molecular level rather than the ensemble characteristics. Protein packing and patterning are advancing towards a more compact and ordered fashion. Meanwhile, protein adsorption behavior becomes more complex when the physical dimension of the underlying surface features becomes closer to that of the protein. Hence, the development of miniaturized 2D materials as protein adsorption templates are important as it can assist in controlling and understanding protein adsorption in greater detail.

Protein microarray is one representative example of miniaturized biomaterial which permits highly compact protein detection with boosted sensitivity and sample conservation. State of the art protein microarrays often consist of nanometer scale features and are commonly addressed as protein nanoarrays.[45–50] Ordered nanoarray have the advantage of promoting the protein payload for higher detection sensitivity as well as providing uniformity for data precision and consistency. Polymers, due to their wide range of tunable physical and chemical properties, have been used extensively as protein nanoarray templates. Many techniques including both top-down and bottom-up approaches been developed to generate nanopatterned protein arrays. This section introduces the traditional top-down approaches for protein nanopatterning as well as the novel bottom-up approach that uses advanced polymer as a template to guide protein nanopattern formation.

1.2.2 Top-down Approaches for Protein Nanopatterning

Photolithography is one of the main methods used for producing micro/nanopatterns on polymeric surfaces. Nanopatterns are created by selectively exposing a polymer-coated surface to photoirradiation and, if necessary, removing the selected areas through solvent dissolution. It is a cost-effective technique that allows surface features with good alignment and controlled topography to be generated in a large area, and high spatial resolutions down to 10 nm can be achieved with advanced polymer template or optical techniques.[51–54] Maskless photolithography through the assistance of micromirror array has also been reported.[55] However, the downsides of the photolithography techniques are the high cost and potential alteration to the electronic and optical properties of the functional polymers.

A more cost-efficient method, nanoimprint lithography (NIL), is realized by pressing a prepatterned mold against a softened or liquid polymer, and the patterned is fixed by either cooling the thermoplastic polymer (thermal NIL) or by UV-photocuring the liquid polymer precursor (UV-NIL).[56] The imprinted substrate can be further modified to acquire protein adsorption patterns. For example, Hoff et al. imprinted nanopatterns onto PMMA coated SiO_2 substrate by a silicon mold and bind proteins through specific interactions to the immobilized patterned ligands.[57] NIL has the advantage of high throughput, low cost, and a capacity of reaching high resolution of as low as 5 nm with both thermal and UV methods.[58,59]

Electron-beam lithography (EBL), is a well-developed, maskless technique that uses an electron beam to scan across the surface and can create features with sub-10 nm sizes.[60] Taking the advantage of the sensitivity of self-assembled monolayers (SAMs) to electron irradiation, thiolates SAMs can be selectively removed from metal surfaces and the exposed area can be used for biomolecule patterning.[61,62] Denis et al. created a binary surface consist of methyl-terminated

alkylsilane (CH_3) tracks with 60-90 nm widths embedded in an oligo-(ethylene glycol)-terminated alkylsilane (PEG) background through EBL and observed guided alignment and assembly behavior of collagen on this template.[63] Although EBL can conveniently pattern features with arbitrary shapes, it requires vacuum condition to operate and can be highly time consuming, which limits its potential in multicomponent and high throughput nanopatterning applications.

Direct writing techniques create patterns by delivering molecules from a nozzle or from a probe tip to the surface. In ink-jet printing, a jet of polymer solution or reactive ink is deposited onto the substrate to directly form pattern when solvent evaporates or selectively etch the surface, respectively. This versatile technique can readily provide accurate placement of pre-determined quantities of material. A detailed review of ink-jet printing of proteins was written by Delaney et al.[64] Nevertheless, since the resolution of the surface pattern is defined by the droplet size in this method, the pattern sizes are limited to the micrometer range.[65]

Dip-pen nanolithography (DPN) is another relatively new direct writing technique. It utilizes an "inked" atomic force microscope (AFM) tip to deposit molecules to the surface. The ink transports from the tip via diffusion through water meniscus that forms between the tip and the surface.[66,67] There are two methodologies for protein patterning using DPN: direct and indirect. The direct approach involves direct deposition of protein on the surface, while in the indirect approach, protein adherent molecules are first deposited. In indirect DPN, specific interactions such as electrostatic interactions[68] and coupling reactions[69] have been used to immobilize proteins onto oppositely charged surfaces without the loss of activity. Although direct DPN has the advantage of being able to generate multicomponent arrays and not requiring non-specific binding, it also poses challenges such as transporting high molecular weight protein to the surface while retaining resolution and patterning speed.[70] Overall, DPN is a versatile tool for protein

nanopatterning, which application also extend to DNA, peptide, and virus patterning on various substrates.

Many other top-down techniques such as microcontact printing (μCP) or nanocontact printing (nCP), nanografting, nanoshaving, and particle lithography have been used for protein nanopatterning, and detailed description of which can be found in several review articles.[65,70,71]

1.2.3 Block Copolymers as Protein Nanopatterning and Adsorption Study Template

While top-down methods present precision and versatility in producing protein nanopatterns, they have many disadvantages such as time consuming, high cost, and requiring multiple complex fabrication steps. On the contrary, self-assembly of block copolymers (BCP) is a bottom-up approach which provides a fast and facile way to generate nanopatterns at large scales without the need of extra surface modification. Furthermore, the phase separated block copolymers can inherently serve as a protein nanopatterning template with various nanodomain sizes, shapes, and chemical properties.

Block copolymer is a class of polymer that consist of two (or more) chemically distinct but covalently connected polymer components. Due to the immiscible nature of the monomeric segments, block copolymers can phase separate into chemically heterogeneous nanodomains of variable geometries, which include sphere, cylinder, gyroid, and lamellae (Figure 3). The nanoscopic morphology is determined by parameters including the temperature-dependent Flory–Huggins interaction parameter (χ), composition fraction of the components (f), and the degree of polymerization (N).[72,73] By tuning the thermodynamic conditions and the composition of the polymer constituents and the thermodynamic conditions, nanodomain of desired morphology can be achieved. The organization of the nanodomain patterns can be further controlled by external guides such as flow fields, electric fields, roll-casting, and directed self-assembly (DSA)[74–76]. This

convenient nature of block copolymers makes them ideal platforms for nanoscopic protein patterning and adsorption studies.[77]

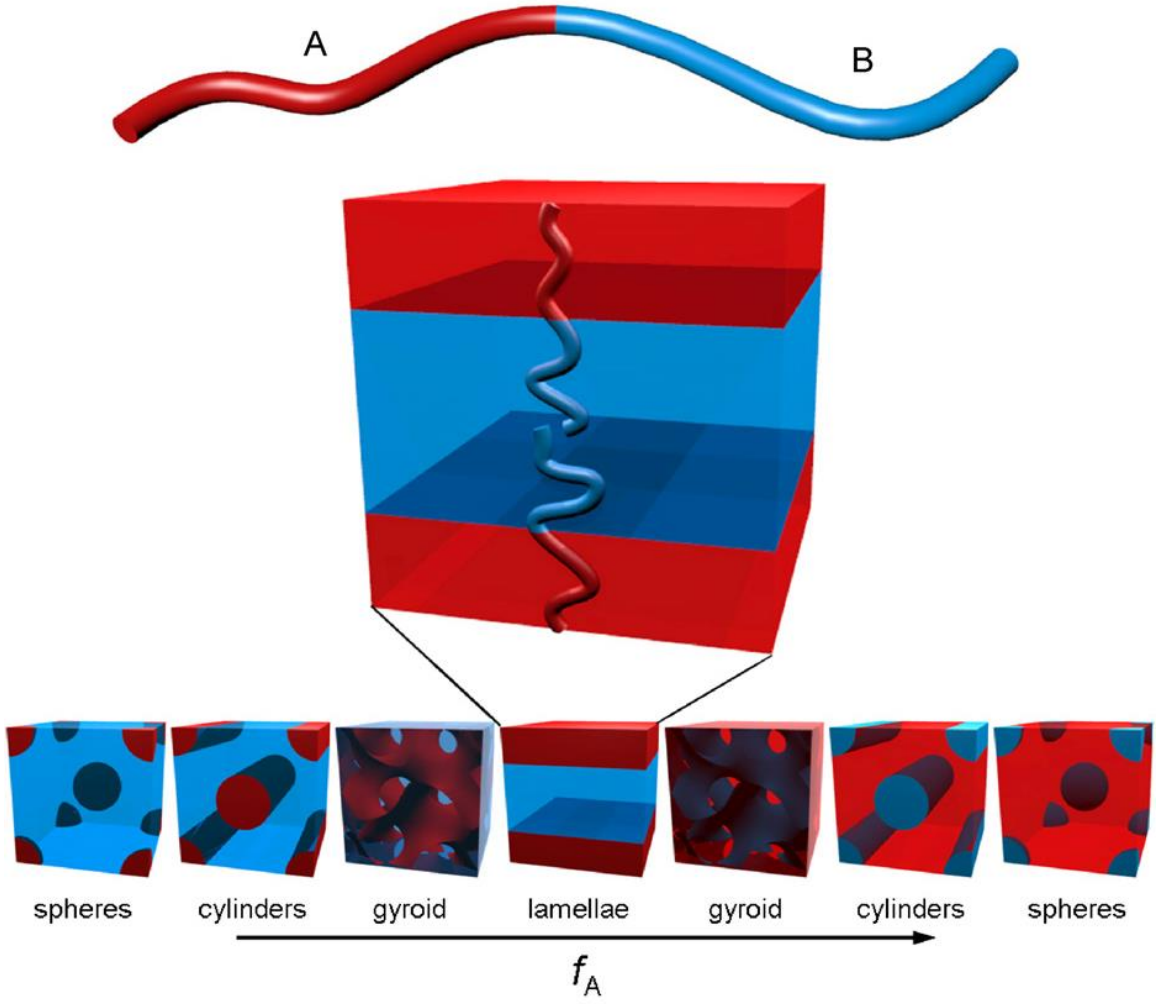

Figure 3. Schematics of a diblock copolymer molecule (top) and the four available equilibrium morphologies. Reproduced with permission from Ref. 78.

Protein adsorption on block copolymers was first investigated at individual protein level by Kumar et. al. on a 45 nm repeat spacing cylindrical polystyrene-block-polymethylmethacrylate (PS-b-PMMA) thin film. Unique adsorption phenomena were discovered. Globular proteins of IgG and BSA showed a highly selective interaction with the phase-separated nanodomains of PS-b-PMMA and adsorbed exclusive on the hydrophobic PS domain while completely avoiding the

relatively hydrophilic PMMA domain. This result agrees with the previous finding on homogeneous polymer surfaces that protein's non-specific adsorption favors the more hydrophobic surfaces.[7,79,80] In further examination, it was discovered that protein's adsorption favors the chemical interface between the two neighboring PS and PMMA nanodomains, and surface density of the protein would decrease exponentially with its lateral distance to the chemical interface in a larger scale.[81] This could be explained by the combining effect of the amphiphilic nature of the protein surface and the chemical heterogeneity displayed by the nanodomain interfaces.[82] As a result, the overall protein adsorption density would increase with the increased density of chemical interfaces presented on the surface, and protein adsorbed on the PS-b-PMMA surface was found to be indeed denser than that on the homogeneous surfaces with the same polymer components. Figure 4 displays the protein density on different polymeric surfaces with the following order: PS-b-PMMA block copolymer > PS/PMMA blend > homopolymer PS > homopolymer PMMA. Highly preserved conformation and activity (85% of that in free solution) of horseradish peroxidase(HRP) enzymes was observed on the PS-b-PMMA template.[83]

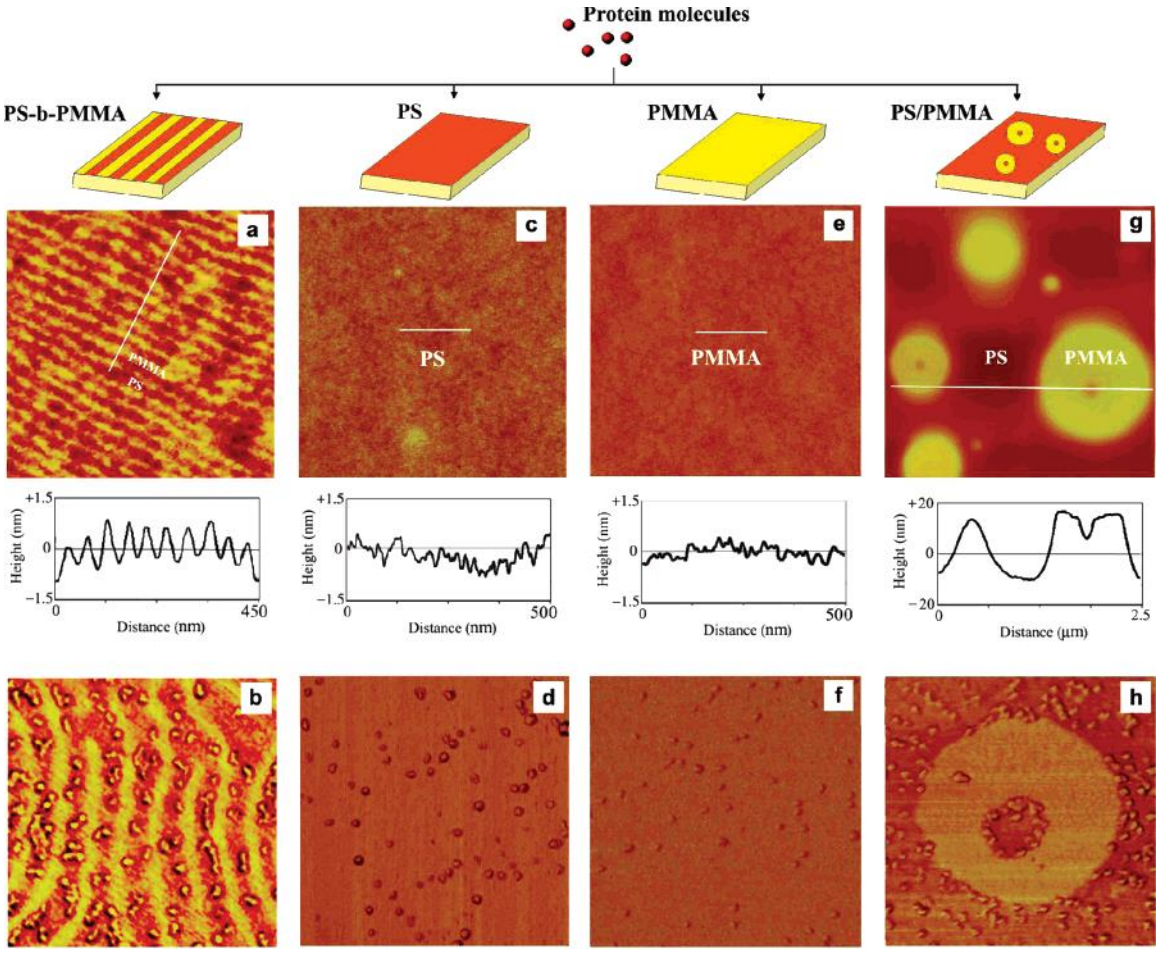

Figure 4. Schematics and atomic force microscopy images showing various polymeric surfaces before and after immunoglobulin G deposition. AFM images correspond to (a) PS-b- PMMA (750 × 750 nm2), (b) 4 μg/mL IgG on PS-b-PMMA (380 × 380 nm2), (c) PS (2 × 2 μm2), (d) 4 μg/mL IgG on PS (500 × 500 nm2), (e) PMMA (2 × 2 μm2), (f) 4 μg/mL IgG on PMMA (500 × 500 nm2), (g) PS/PMMA blend (2.5 × 2.5 μm2), and (h) 10 μg/mL IgG on PS/PMMA blend (750 × 750 nm2). Protein adsorbs preferentially on the PS (lighter colored) regions over the PMMA regions and closer to the PS/PMMA interfaces. Reproduced with permission from Ref. 81.

In contrast to the highly selective adsorption behavior of globular proteins on the block copolymers, a more neutral and concentration-dependent adsorption characteristic was observed from the investigation of elongated fibrinogen (Fg) on the same PS-b-PMMA template.[84] For this elongated protein, the strongly biased adsorption to a favored polymeric block was seen only at high protein concentrations. At low concentrations, both the preferred and non-preferred polymeric blocks played a role in the adsorption process via protein subdomain-specific interactions with different polymer segments. More specifically, Fg was found to land spanning over both PS and

PMMA domains at low adsorption density by locating the central E domain in the PMMA domain and the two distal D domains in the adjacent PS domains. Fg configuration during assembly and surface packing processes was also examined. Fg was found to take a stacked bow-shaped packing configuration on the PS domains with the major protein axis perpendicular to the long axis of the polymeric nanodomain.

However, in these previous studies, no attempts were made to control the physical dimensions and alignment of the nanodomains guiding the protein self-assembly following surface adsorption. Yet, more fundamental insights can be drawn by investigating the Fg adsorption and packing behaviors by varying the size (repeat spacing) and the alignment of the underlying polymeric nanodomains. Such changes in the physical dimensions and alignment of the nanoscale polymeric templates may enable fine-tuning of the protein−surface interactions, which can then be used to direct the adsorption and assembly nature of Fg. In addition, a precise understanding of the roles that the nanoscale polymeric surfaces play in Fg adsorption and assembly can be potentially helpful for controlling the biological consequences of the protein. For example, surface-controlled self-assembly of Fg molecules in a specific or random orientation may be further exploited to control the clotting process in a thrombin-less environment or to deter unwanted blood clotting on implant materials, respectively.[85] In this regard, Chapter Two presents my research work on Fg nanopatterning and configuration study at a series of block copolymer surfaces with varying surface nanofeatures.

In addition to the application as protein nanopatterning template, phase separated block copolymers thin films is also an ideal template for studying surface-adsorbed protein at nanoscopic level. The topologically flat yet chemically varying surface patterns on the BCP surfaces can be adjusted to the same size scale of the protein molecules (tens of nanometers). This interesting

feature that is achievable through facile BCP self-assembly mechanism not only adds a means to provide unique surface chemical environment for controlling protein adsorption behavior but can also serve as a template for assisting the tracking of individual biomolecules in the time-resolved microscopic study of the protein adsorption dynamics. I present in Chapter Three and Four my newest findings on the multicomponent protein adsorption behavior on nanopatterned block copolymer surfaces with direct molecular level evidences.

1.3 Characterization Techniques in Protein Adsorption Studies

1.3.1 Common Protein Adsorption Detection Methods

In the effort to characterize protein adsorption behavior on material surfaces, many characterization techniques have been used obtain valuable information in both qualitative and quantitative fashion.[11,86] Fluorescence base technique is one of the most popular protein detection methods in both laboratory and clinic applications. With the availability of the vast variety of fluorophores, fluorescence microscopy provides a versatile and convenient means to detect different types of proteins in complex systems. More sophisticated fluorescence techniques have been developed to further extend the detection range and acquire additional information of the protein.[87] Total internal reflection fluorescence (TIRF)[88] significantly improves the signal-to-noise ratio by confining the excitation to a narrow surface evanescent field generated by total internal reflection and selectively collect the fluorescence signal of the surface bond fluorophores while excluding background signals. This allows protein adsorption kinetic to be determined at single protein level.[89–92] Förster resonance energy transfer (FRET)[93] is another frequently used single molecular fluorescence detection technique. FRET is the non-radiative energy transfer between a donor and an acceptor fluorophore via dipole-dipole interactions. When the distance of these donor and acceptor fluorophores are close enough in the range of Förster radius (3–7nm), excitation

energy can be transferred through electronic resonance of molecular orbitals.[94] Since this energy transfer efficiency is highly sensitive to distance, it can be used to examine protein-protein interactions,[95,96] protein conformational changes,[97] and protein folding behaviors.[98] However, fluorescence base techniques usually require the introduction of fluorophores and are sometimes accompanied with high background signals. The spatial resolution of confocal microscopy-based methods is also restrained by the diffraction limit of the visible light. These all may present difficulties in quantitative measurements.

Many label-free techniques have been applied in protein adsorption studies. For example, optical-based methods such as ellipsometry (ELM),[99,100] surface plasmon resonance (SPR),[101–103] and optical waveguide lightmode spectroscopy (OWLS)[104–106] monitor the mass change on planner surfaces through different detection mechanisms: ELM measures the polarization state change of the reflected light from the surface; SPR utilizes the light excitation of surface plasmon in thin metal layers and measures the change in minimum angle of total internal reflection; OWLS couples a light beam into a waveguide film and detects the refractive index changes. By tracking these optical parameters, subtle changes in the adsorbed protein mass and layer thickness can be measured with high precision, and kinetics of the adsorption process can be inferred. Quartz crystal microbalance (QCM)[19,107] is another commonly used mass detection technique, which makes use of the mass-sensitive oscillating frequency of the crystal to detect the amount of protein loaded on the surface. These techniques are highly sensitive, easy to handle, and can monitor real-time adsorption events in aqueous media. However, there are limitations. For instance, ELM only works on reflecting surfaces with known optical properties. SPR requires the substrate to be coated with a metal layer (typically gold or silver). OWLS demands a transparent waveguiding substrate and a nonmetal coating with limited thickness. QCM is not capable of measuring the dry mass of the

adsorbates. Therefore, in practice, many of these techniques are used in complementary to other techniques to acquire more comprehensive information.

Structural and elemental composition of protein can also be analyzed to give qualitative and quantitative information of the adsorption behavior. Surface-enhanced Raman scattering (SERS) is a spectroscopy technique that uses metal surface or metal particles to enhance the Raman signal, which has been proven to be a highly sensitive, selective, and quantitative tool for protein analysis.[108–110] In addition, Raman mapping allows visualization of the adsorption area, which has be used in some protein fouling studies.[111] Elemental analysis such as X-ray photoelectron spectroscopy (XPS) take advantage of the abundant nitrogen element in proteins, which is less common in material substrates, to analyze the amount of protein adsorbed.[112] More advanced X-ray techniques such as scanning transmission X-ray microscopy (STXM) and X-ray photoemission electron microscopy (X-PEEM) have been used to obtain spatial information of both the protein and the surface features.[113–115] However, many of these spectroscopic methods are time consuming and low in spatial resolution, which makes conformational information of the protein difficult to obtain in large scale.

However, many cases of the aforementioned nanoscale investigations require a high-resolution imaging technique capable of resolving both the nanoscopic details of an underlying surface as well as the subdomain features of individual biomolecules, which resorted to the AFM technique.

1.3.2 Atomic Force Microscopy for Protein Imaging

As an offshoot technique of scanning tunneling microscopy (STM), AFM was first invented and implemented in 1986 by Gerd Binning and coworkers in attempt to extend the STM technique to image non-conductive samples. A typical AFM system consists of a micro-fabricated

flexible cantilever with a sharp tip (usually made of silicon or silicon nitride) mounted to a piezoelectric actuator and a position-sensitive photodiode detector which receives a laser beam deflected from the mirrored back of the cantilever. There are multiple operating modes of AFM, and the two primary ones are contact mode and tapping mode.

The most common AFM scanning type is contact mode. In this mode, the AFM tip that is attached to the end of a cantilever is in constant contact with the surface and is scanned across the sample through the x-y plane. Surface topography induces changes in cantilever defection of the laser beam, which is amplified by the long optical path before reaching the photodetector. A feedback loop was used to maintain a constant deflection (i.e., tip-surface interaction force) by vertically moving the scanner, and this vertical distance is then recorded to form a topographic image of the sample surface (Figure 5, left). In addition, the difference in signal from laser defection can be used as a direct measurement of the surface topography (without actual height data). Contact mode AFM is suitable for imaging hard surfaces and fixed cells at high scanning speed, however, the shear force that is created during contact imaging may sweep the adsorbed molecules to change their lateral positions or even damage delicate samples.[116–118] Hence, contact mode AFM is often unsuitable for single protein adsorption studies.

Tapping mode AFM resolves the problem of shear force by vertically oscillating the cantilever at or near its resonance frequency with an amplitude ranging typically from 20 nm to 100 nm. This results in an intermittent soft contact between the tip and the sample surface (tapping), which attenuates the root mean square (RMS) oscillation measured from deflected optical signal. As with in contact mode, a feedback loop is applied to change the vertical position of the scanner to maintain a constant RMS value, and height information at each lateral scanning position can be obtained (Figure 5, right). This method provides a means to generate high resolution 3D imaging

in both atmospheric and aqueous conditions without interfering the sample surface or the adsorbed biomolecules.[119–121] On top of the topographical information, tapping mode is also able to track phase changes of the cantilever oscillation for monitoring the magnitude of interactions between the tip and the surface. This is particularly useful when scanning flat surfaces consist of multiple chemical components, such as phase separated BCP's.[122,123]

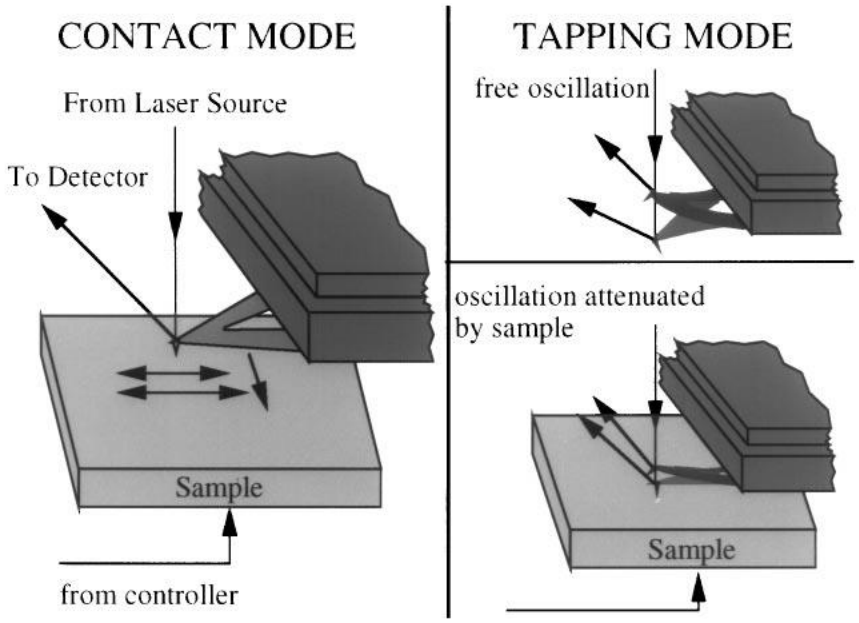

Figure 5. Schematic illustration of the two main atomic force microscopy operating modes. In contact mode (left), constant contact between the probe and the surface is maintained during raster scanning the sample. Laser defection change induced by sample topography is detected and used in a feedback loop to maintain constant contact. In tapping mode (right), the cantilever is oscillating vertically during raster scanning. The intermittent contact between the probe and the sample surface causes attenuation of the oscillation amplitude, which is used to monitor sample topography. Reproduced with permission from Ref. 124.

Comparing to the characterization techniques mentioned in the previous section, AFM offers spatial resolution sufficiently high enough for resolving simultaneously the nanometer-size individual proteins and the underlying polymeric BCP nanodomains.[82,84] AFM also has the advantage of circumventing the need for crystallization, labelling, conductive metal coating, or high vacuum/low temperature operation of protein samples.[5,125,126] For examining competitive adsorption, the direct visualization capability of AFM to be able to discern different protein species

based on their sizes and shapes may be exploited. It can be used to directly track particular proteins of interest on the same surface areas and record changes in their adsorption behaviors between different treatments. Such approach may offer definitive experimental evidence for many postulations made in protein adsorption mechanisms that are often inferred from ensemble-averaged adsorption properties[7,91,100,127] due to the current lack of direct experimental proof provided at the single biomolecule level. Due to these reasons, AFM was chosen as a main characterization tool in all the research works that I am presenting in this dissertation.

2 Surface Assembly Configurations and Packing Preferences of Fibrinogen Mediated by the Periodicity and Alignment Control of Block Copolymer Nanodomains

2.1 Introductions

In this chapter, I examine the precise effects of the changes in the periodicity and the alignment of phase-separated polymeric nanodomains on the adsorption and packing characteristics of Fg molecules during their surface assembly. The surfaces examined in this work are PS-b-PMMA with a repeat spacing of the nanodomains much smaller than the length of the Fg (sm PS-b-PMMA), PS-b-PMMA with a periodicity comparable to the Fg length (com PS-b-PMMA), a non-phase-separated random copolymer of the same chemical constituents (PS-r-PMMA), and aligned PS-b-PMMA (dsa PS-b-PMMA) formed via a method known as chemoepitaxy directed self-assembly (DSA).[75] By faithfully resolving characteristic adsorption patterns of individual Fg molecules under low to high surface coverage conditions at the single- and subprotein level, I identify the exact subdomain-specific configurations of Fg molecules with respect to the chemically alternating polymeric nanodomains. I also elucidate the preferred packing geometries between single Fg molecules at both low and high surface coverage. Through my direct visualization efforts, I unambiguously present the exact configuration and packing geometry of individual protein molecules in the extended network of assembled Fg specific to the different PS-b-PMMA templates. The outcomes of this study signify that the physical dimensions and alignment of the underlying nanoscale polymeric surface can be used to control the protein surface density, preferred adsorption configuration, protein subdomain-specific packing interaction

between Fg, and alignment direction of individual Fg in large scale organization. I further demonstrate that the BCP surface-assembled Fg molecules can serve as chemical and biological guides to selectively seed and grow calcium phosphate nanoparticles. Finally, it is demonstrated that the PS-b-PMMA-bound Fg molecules retain their biofunctionality via the analysis of Fg-activated microglia cells.

2.2 Results and Discussion

2.2.1 Fibrinogen Structure

An elongated protein of Fg, exhibiting high aspect ratios of ~10 (length to width) and ~25 (length to height),[84] is composed of three interwoven polypeptide chains of Aα, Bβ, and γ that are connected together by 29 disulfide bonds. The structure of the 340 kDa dimeric protein consists of rod-like chains spanning three spherical domains of D (at the two ends) and E (at the center). The protein exhibits a net negative charge (pI = 5.2) in a physiological pH of 7.4. The structures of Fg were first imaged by electron microscopy (EM), revealing the molecular length of 47.5 nm with roughly spherical D and E domains depicted by a trinodular model.[128] Later, more complex depictions of Fg such as 45 nm-long heptanodular and octanodular models were reported based on EM and crystallographic observations.[129–132] In more recent years, the high resolving power of AFM attained with noninvasive protein sampling conditions has been recognized as highly beneficial, and hence, AFM has been extensively used to visualize Fg in air or a biological buffer directly with no need for staining, crystallization, or vacuum drying.[133–141] The schematic representation in Figure 6A depicts the commonly discussed trinodular model of Fg consisting of the three spherical nodules embodying the two D and the E domains that are linked by coiled-coil connectors.[128] The center E region has the NH_2-termini of all polypeptide chains, while the distal D regions are formed by the COOH-termini portions of the Bβ and γ chains as well as a portion of

the Aα chain. In a more complex heptanodular model of the protein shown in Figure 6B, each D domain is further divided into two lobes stemming from the independent folding of β and γ chains that are shaped into the βC and γC lobes, respectively.[129–131,142] A small, nonhelical globular domain, serving as a binding site to plasmin, is also included in each coiled-coil arm of the complex model. The α chain is longer than the β and γ chains and extends toward the center of the molecule from the βC and γC lobes, forming a globular αC domain at its C-terminus. While considering Fg sizes from the most closely related protein preparation and measurement conditions to the Fg adsorption behavior reported in this study, the overall dimensions of Fg on PS-b-PMMA can be approximated as 45 nm along the long axis of the protein spanning the D–E–D domains with an average spherical domain height of 2.2 nm,[84] as indicated in Figure 6.

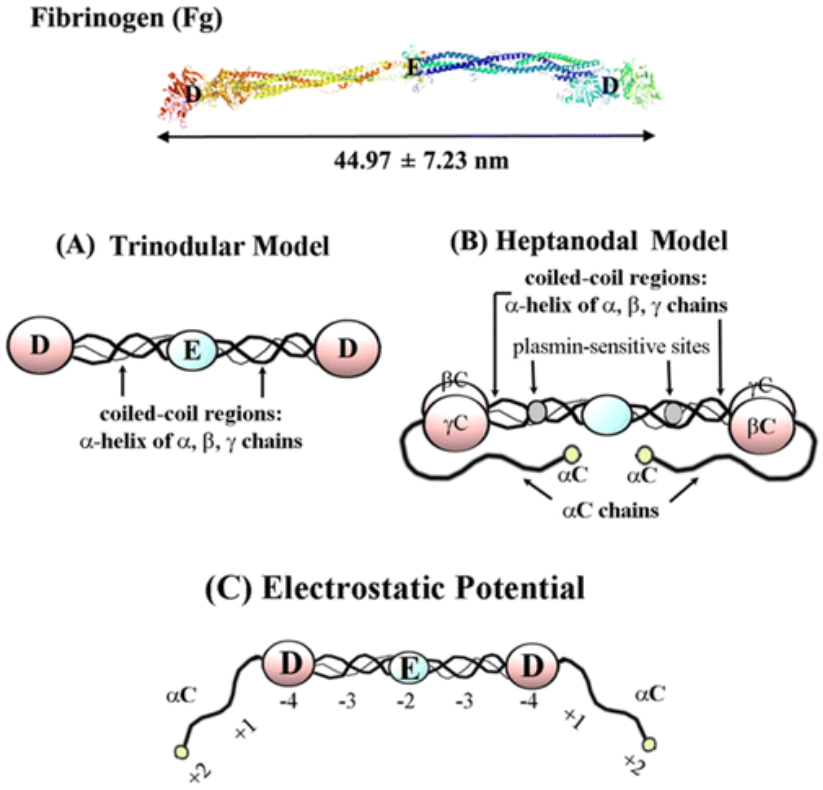

Figure 6. Schematic representations showing the different protein subdomains present in fibrinogen. The indicated value of the Fg length is taken from an earlier AFM study[84] statistically examining the protein size on a PS-b-PMMA surface. The trinodular and heptanodular structural models of Fg are displayed in panels A and B, respectively. The electrostatic potential model for Fg is shown in panel C.

2.2.2 Polymeric Surfaces under Investigation

The four types of polymeric surfaces employed in my study are listed in Table 1. Block and random copolymers with the chemical compositions of PS and PMMA are chosen owing to the widespread use of PS and PMMA in biomedical products,[143] as well as the well-known phase separation behavior of PS-b-PMMA exposing both polymer segments at the air/polymer interface in thin films.[122,144–146]The copolymer subsets of PS-b-PMMA and PS-r-PMMA in Table 1 are then specifically selected by taking into account the length scale of the repeating nanodomains (i.e., the periodicity of the associated chemical interfaces) with respect to the long axis of Fg and the degree of nanodomain alignment (i.e., nanodomain orientation within the substrate plane). The typical surface morphologies of the different polymeric substrates employed in this study were first characterized by AFM to examine the surface roughness and nanodomain structures, as shown in Table 1 and Figure 7. All four surfaces show similar values for the average (R_a) and root mean squared (R_q) roughness, indicating negligible variations relative to the physical dimensions of Fg.

Table 1. Four Different Polymeric Surfaces Used in the Fg Adsorption Study along with Their Surface Roughness and the Repeat Spacing Values of the Nanodomains[a]

			surface roughness (nm)		
surface type	**domain alignment (thin film morphology)**	**periodicity (nm)**	R_a	R_q	**panel of Figure 7**
dsa PS-*b*-PMMA	fully aligned (⊥ lamellae)	28	0.309	0.385	A
sm PS-*b*-PMMA	random, fingerprint-like (⊥ lamellae)	25	0.265	0.332	B
com PS-*b*-PMMA	random, fingerprint-like (∥ cylinders)	45	0.289	0.361	C
PS-*r*-PMMA	[b]	[b]	0.206	0.260	D

[a]Ra and Rq values correspond to the average and root mean squared roughness of the polymer surface, respectively. [b]Not applicable.

The AFM micrographs of the four types of polymeric surfaces are displayed in the topography and phase panels in Figure 7. The characteristic nanodomain sizes and alignment

specific to the dsa PS-*b*-PMMA, sm PS-*b*-PMMA, com PS-*b*-PMMA, and PS-*r*-PMMA surfaces can be seen in the paired set of AFM panels as well as in the height versus distance profile of each polymeric surface. Their representative AFM panels are shown in Figure 7, panels A, B, C, and D, respectively. The polymeric surfaces of dsa PS-*b*-PMMA and sm PS-*b*-PMMA exhibit periodic nanodomains of PS and PMMA with measured periodicities (i.e., repeat spacings) of 28 and 25 nm, respectively, which are smaller than the length of Fg. The nanodomains on dsa PS-*b*-PMMA surfaces are well-aligned in one direction via directed self-assembly whereas those on sm PS-*b*-PMMA have fingerprint-like patterns formed in random directions on the surface via thermal annealing. The nanodomains in com PS-*b*-PMMA expose a periodic spacing of 45 nm, a dimension that is comparable to the length of Fg, while exhibiting randomly oriented, fingerprint-like patterns similar to those of sm PS-*b*-PMMA. The specific types of topological defects[122] found in the sm PS-*b*-PMMA template in Figure 7B are seven dislocations and one disclination. The same classes and numbers of defects are on the com PS-*b*-PMMA template in Figure 7C. After accounting for the surface area, I can approximate the density of the topological defects on the sm PS-*b*-PMMA and com PS-*b*-PMMA surfaces as 37 μm^{-2} and 15 μm^{-2}, respectively. In contrast, no such topological detects are present on the aligned template of dsa PS-*b*-PMMA in Figure 7A. PS-*r*-PMMA surfaces represented in Figure 7D do not display any defined nanodomain structures due to the random distribution of the styrene and methyl methacrylate repeat units in the polymer chains.

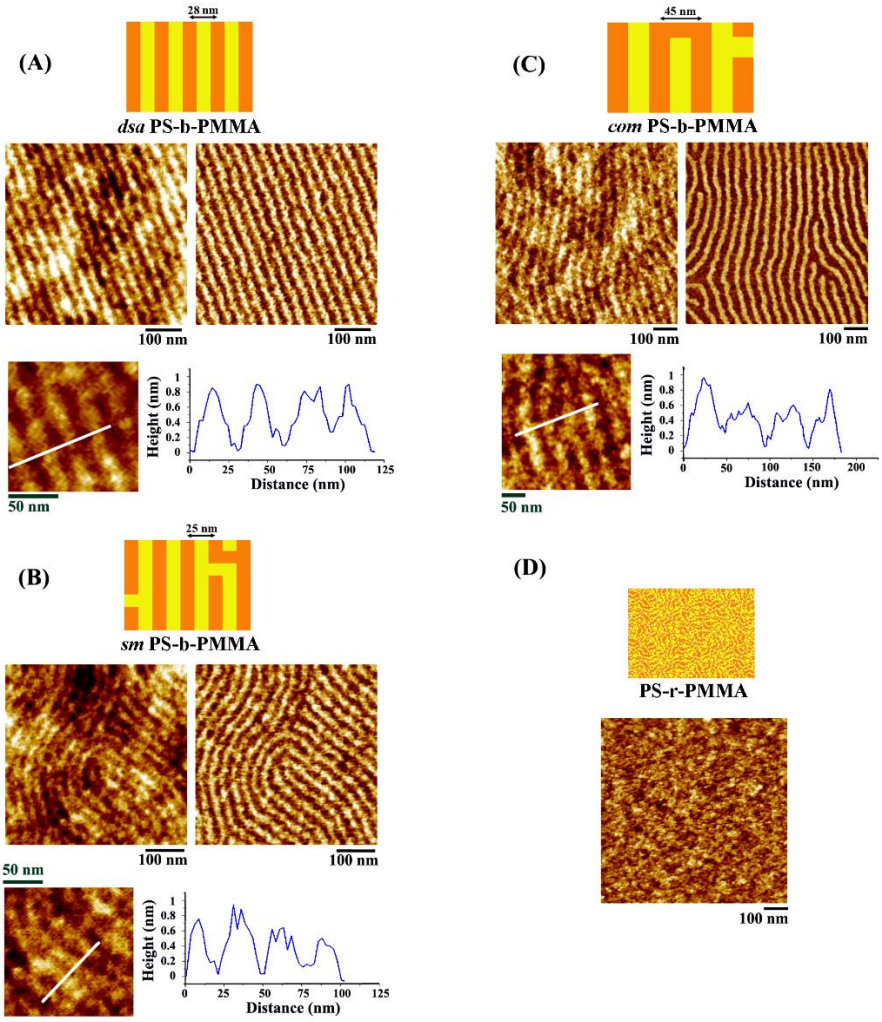

Figure 7. Four types of block copolymer templates employed in my fibrinogen adsorption study are analyzed with atomic force microscopy whose micrographs display the characteristic nanodomain sizes and orientations specific to (A) Directed self-assembly aligned PS-b-PMMA (dsa PS-b-PMMA), (B) PS-b-PMMA with the repeat spacing of the nanodomains smaller than the length of Fg (sm PS-b-PMMA), (C) PS-b-PMMA with the repeat spacing of the nanodomains comparable to the Fg length (com PS-b-PMMA), and (D) PS-r-PMMA with no nanodomains. In the paired set of AFM panels shown, the left and right frames correspond to the topography and phase scans, respectively, of the same template areas. Height versus distance profiles were measured along the white lines inserted in the enlarged topography images shown under the paired AFM panels. The line analysis results are then presented in order to show the different repeat distances of the striped nanodomains in each BCP template.

2.2.3 Adsorption Characteristics of Isolated Fibrinogen at Low Concentrations

Typical Fg adsorption behaviors on these well-characterized polymeric templates were subsequently investigated while varying the protein concentration. For all Fg data presented in this paper, I treated the different polymeric substrates with an identical protein adsorption procedure; a 10 μL volume of Fg solution of desired concentration in PBS buffer (10 mM mixture of

$Na_2HPO_4$and NaH_2PO_4, 140 mM NaCl, 3 mM KCl, pH 7.4) was administered to the substrate followed by a 20 s incubation. Subsequently, the sample surface was rinsed with an ample amount of PBS and gently dried under a stream of N_2 prior to AFM imaging. Representative AFM images acquired using concentrations of 2.5 and 12.5 μg/mL on dsa PS-*b*-PMMA and sm PS-*b*-PMMA are shown in the double-paired frames of topography and phase of the left and right sets, respectively, in Figure 8A, B. Under these protein deposition conditions, "more neutral" Fg adsorption behavior was seen on the BCP templates. The neutrality in interaction refers to the tendency of Fg to adhere to both PS and PMMA domains of the PS-*b*-PMMA surface through protein subdomain specific interactions under low concentration conditions. This phenomenon is in contrast to the entirely exclusive adsorption only onto the PS domain region of PS-*b*-PMMA revealed from other globular proteins such as immunoglobulins and serum albumins under similar surface coverage.[81,82,147] In such cases, the differences in the degree of hydrophobic interactions between the protein and the dissimilar polymeric segments were attributed to the completely discriminatory surface adsorption of the globular proteins to the favored PS segment.[148–150]For the elongated protein Fg, the interplay between the hydrophobic and electrostatic interactions existing between the protein and the polymeric segments as well as the electrostatic repulsion between the proteins can lead to the more complex protein subdomain- and concentration-specific adsorption characteristics.[82,151]

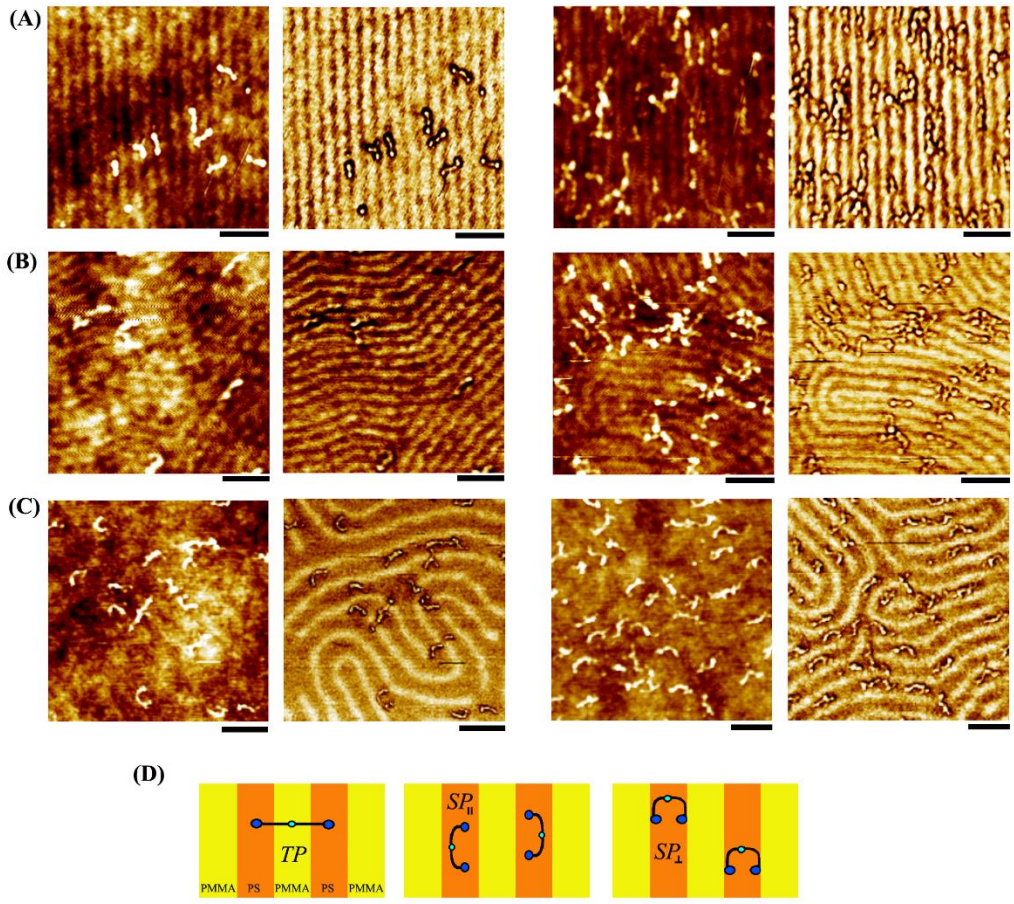

Figure 8. Atomic force microscopy panels display typical fibrinogen adsorption behaviors on the three well-defined diblock copolymer surfaces of PS-*b*-PMMA. The underlying polymeric template varied from (A) dsa PS-*b*-PMMA to (B) sm PS-*b*-PMMA and (C) com PS-*b*-PMMA. The double sets of AFM images paired on the left and right in panels A and B correspond to protein concentrations of 2.5 and 12.5 μg/mL, respectively, whereas those shown in panel C are 5 and 20 μg/mL, respectively. Within the paired set, the left and right frames are the respective topography and phase AFM scans of the same areas. The 100 nm scale bar is inserted under each frame. (D) The schematic representations show the three possible adsorption configurations of Fg (TP, $SP_{\parallel}$, and $SP_{\perp}$) with respect to the local orientation of the underlying nanodomain.

A closer look at the AFM data of Fg on dsa PS-*b*-PMMA and sm PS-*b*-PMMA in Figure 8A, B reveals two distinctive partition scenarios of surface-adsorbed Fg molecules, one with the entire Fg molecule located in the PS domain and the other with portions of the same Fg molecule found not only on the PS but also on the PMMA domain. In the former adsorption configuration, the entire protein is confined in the PS domain, and this configuration corresponds to the main axis of the protein orienting parallel to the local orientation of the nanodomain long axis. I term this configuration as $SP_{\parallel}$, denoting that the full contour of the protein lies on the single

polymeric phase of PS exhibiting a parallel alignment between the Fg molecule and the main axis of the underlying PS nanodomain. The latter adsorption configuration results in the different subdomains of the same protein molecule partitioned to either the PS or PMMA regions. This adsorption configuration is yielded from the protein main axis orienting perpendicular to the major axis of the nanodomain. This geometry is termed as TP since two polymeric phases are involved in the adsorption of the same protein and the adsorption occurs in a perpendicular geometry between the main axes of the protein and the underlying nanodomains. The primary interactions of the protein subdomain-specific partitions on the PS and PMMA nanodomains are such that the center E domain is placed in the middle of a PMMA region whereas the two distal D domains are spread out toward the neighboring PS regions on either side of the PMMA. In addition to these configurations of $SP_{\parallel}$ and TP, an additional adsorption case is monitored on com PS-*b*-PMMA with a configuration termed as $SP_{\perp}$, as shown in Figure 8C. This adsorption setting involves the entire Fg molecule placed within the PS domain but differs from the $SP_{\parallel}$ case by the perpendicularly positioned protein main axis relative to the long axis of the nanodomain. The aforementioned three cases represent the dominant scenarios observed for Fg adsorption on the three different PS-*b*-PMMA templates. For example, under all deposition conditions I tested, no Fg molecules took up the configuration of either $SP_{\parallel}$ or $SP_{\perp}$ on PMMA domains instead of on PS. No cases of Fg configured in TP were found with the E domain located in the middle of a PS domain instead of PMMA. For clarification, the three possible Fg adsorption configurations of TP, $SP_{\parallel}$, and $SP_{\perp}$ are illustrated in Figure 8D.

These Fg adsorption configurations were systematically investigated further on the surfaces of dsa PS-*b*-PMMA, sm PS-*b*-PMMA, and com PS-*b*-PMMA for similarities and differences in their protein partition behaviors. Characteristic Fg adsorption configurations were

subsequently identified for the three surfaces pertaining to the three different Fg adsorption configurations of TP, $SP_{\parallel}$, and $SP_{\perp}$. The zoomed-in AFM panels in Figure 9 display the overlaid topography and phase scans of the proteins on the three BCP templates in order to unambiguously show the main interaction geometries between single Fg molecules and the underlying PS and PMMA nanodomains. On the com PS-*b*-PMMA surface with the nanodomain periodicity that is comparable to the protein length, adsorbed Fg exhibited all three configurations of TP, $SP_{\parallel}$, and $SP_{\perp}$, as shown in Figure 9A. In comparison, the surface engagement of Fg on the other two surfaces of sm PS-*b*-PMMA and dsa PS-*b*-PMMA with their repeat spacings of approximately one-half of the protein length was only through TP and $SP_{\parallel}$, as displayed in Figure 9B, C for sm PS-*b*-PMMA and dsa PS-*b*-PMMA, respectively. In fact, it was confirmed under all protein concentrations that no surface-bound Fg molecules adopted $SP_{\perp}$ on these BCP templates with nanodomain periodicities smaller than the Fg length.

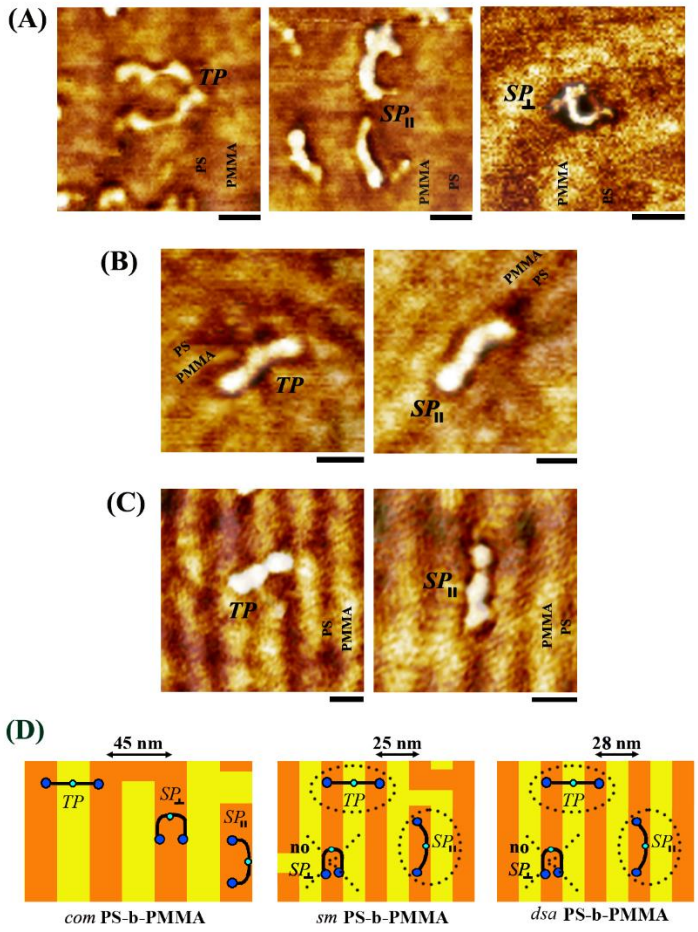

Figure 9. Overlaid atomic force microscopy topography and phase panels display the main adsorption configurations of the surface-bound Fg found on (A) com PS-*b*-PMMA, (B) sm PS-*b*-PMMA, and (C) dsa PS-*b*-PMMA. The scale bar is 25 nm. (D) On the narrower nanodomain surfaces of sm PS-*b*-PMMA and dsa PS-*b*-PMMA, only the cases of TP and $SP_{\parallel}$ were observed with no $SP_{\perp}$ configuration appearing under any protein concentration whereas, on the com PS-*b*-PMMA surface whose repeat spacing is comparable to the protein length, Fg exhibits all three configurations of TP, $SP_{\parallel}$, and $SP_{\perp}$.

2.2.4 Surface Packing of Crowded Fibrinogen at Higher Concentrations

When higher concentrations of Fg solution were deposited onto the BCP templates as shown in Figure 10, Fg molecules progressively and favorably fill in the PS regions over PMMA, starting to pack more densely into the available adsorption sites on PS. The tendency for Fg to line up on the PS domains of the sm PS-*b*-PMMA and dsa PS-*b*-PMMA surfaces can be clearly evidenced in Figure 10A, B. Fg molecules, mainly configured in $SP_{\parallel}$, arranged themselves end to end on the PS regions in striped patterns, faithfully following the underlying PS domains. All

available PS domains on the sm PS-*b*-PMMA and dsa PS-*b*-PMMA surfaces were covered by Fg molecules at the protein concentration of 50 μg/mL. I define the protein adsorption conditions under which all surface-exposed PS areas are covered by the protein as the surface saturating and monolayer forming coverage. According to this definition, the monolayer forming condition is attained on PS-*b*-PMMA when the surface coverage of the protein reaches 50% of a given total surface area, since PS domains represent approximately half of the total surface in PS-*b*-PMMA. On the com PS-*b*-PMMA surface, Fg molecules densely packed and saturated all available PS domains at a higher deposition concentration of 100 μg/mL, as displayed in Figure 10 C.

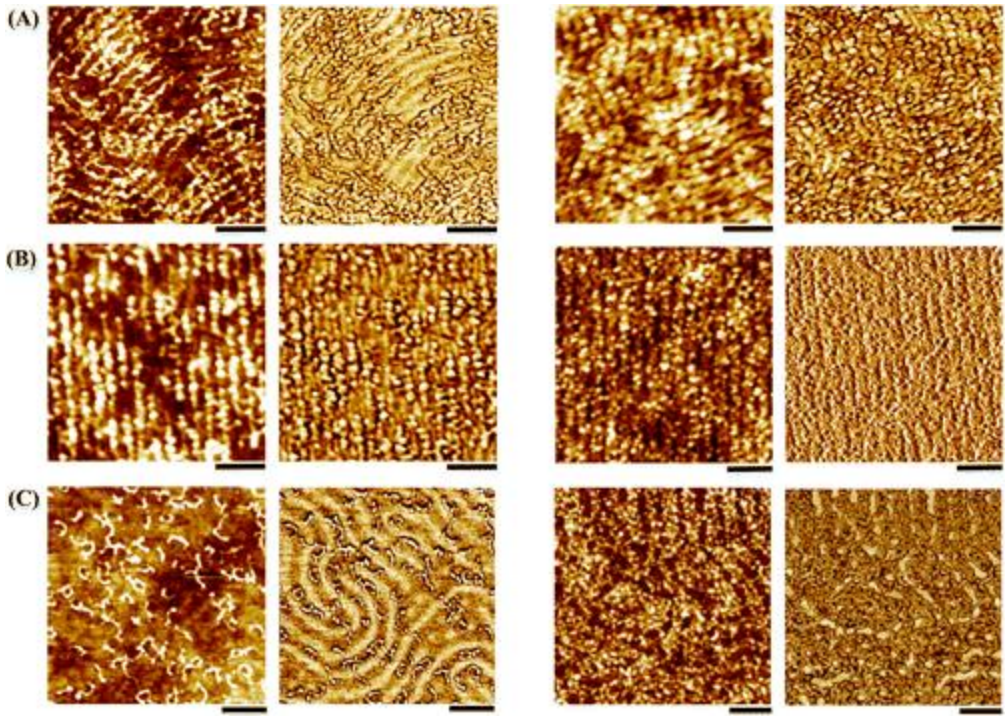

Figure 10. Atomic force microscopy panels display typical fibrinogen adsorption behaviors on the well-defined block copolymer surfaces upon protein deposition at higher concentrations. The left and right images within a set of paired AFM frames correspond to the topography and phase scans, respectively, of the same area. The scale bar corresponds to 100 nm. The underlying polymeric surfaces are (A) sm PS-*b*-PMMA, (B) dsa PS-*b*-PMMA, and (C) com PS-*b*-PMMA. The double paired frames shown in the left and right sets in panels A and B are from Fg concentrations of 25 and 50 μg/mL, respectively. The paired left and right data sets in panel C are obtained from protein concentrations of 50 and 100 μg/mL.

2.2.5 Closer Look at Local and Extended Assembly Behavior of Fibrinogen

Shifting from the earlier focus on studying adsorption behaviors of isolated Fg molecules, I further examined the assembly characteristics of several and many nearby Fg molecules transitioning from a low to high packing density on the sm PS-*b*-PMMA and dsa PS-*b*-PMMA surfaces. I observed an interesting propensity in the local assembly of several Fg molecules as well as in the large-scale packing of many Fg molecules. I determined that a staggered arrangement of Fg molecules was favored between individual proteins located at the neighboring PS domains. The organization behavior of TP- and $SP_{\parallel}$-configured Fg molecules in adjacent nanodomains is shown in Figure 11A for the sm PS-*b*-PMMA case whereas that of $SP_{\parallel}$-configured Fg molecules positioned in neighboring PS domains on dsa PS-*b*-PMMA is shown in Figure 11B. The TP-configured Fg molecules presented in the left panel of Figure 11A display their arrangement with the center E domain of a Fg molecule positioned close to the distal D domain of another Fg molecule in an adjacent PS nanodomain, leading to the skewed assembly patterns between Fg molecules as sketched in the cartoon in Figure 11A. The preferred assembly of staggered Fg molecules is also evidenced from the Fg molecules in the $SP_{\parallel}$ configuration for sm PS-*b*-PMMA (right panel in Figure 11A) and dsa PS-*b*-PMMA (both panels in Figure 11B). In these local and extended assembly processes between $SP_{\parallel}$-configured Fg molecules in an end-to-end geometry on sm PS-*b*-PMMA and dsa PS-*b*-PMMA, the E domains between nearby Fg molecules across neighboring PS rows are not in line with one another. In fact, the positions of Fg molecules in each PS row are slightly shifted in registry with respect to one another, forming a distinctive slope across the staggered Fg molecules between different PS domains. This characteristic staggered assembly behavior can be clearly seen when connecting the same protein subdomain region in single lines spanning across different PS nanodomains, as marked in Figure 11B. The vertical

position shift between two Fg molecules, each located in neighboring PS rows, is estimated to be about 12 nm.

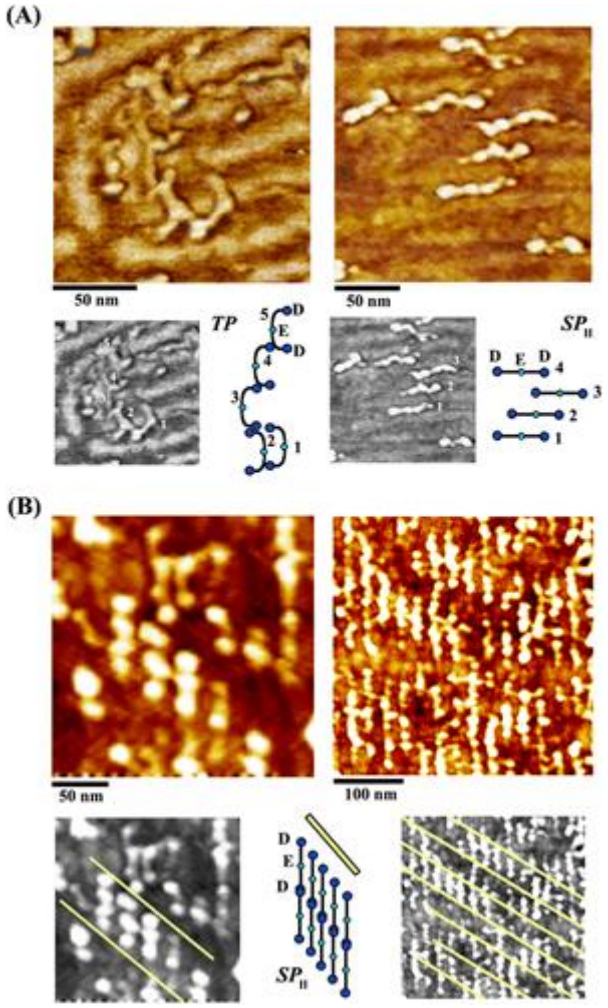

Figure 11. (A) The overlaid atomic force microscopy topography and phase panels display the preferred assembly behavior of nearby fibrinogen molecules in the (left) TP and (right) SP‖ configuration on sm PS-b-PMMA. As a guide to the eye, Fg molecules are numbered in the gray panel shown under the AFM image. The organization layout of the marked Fg molecules is then depicted in the cartoon for each case. (B) The AFM topography images represent the typical Fg packing behavior observed on dsa PS-b-PMMA. The yellow lines inserted in the gray panels show the characteristic slope formed by the neighboring Fg molecules in SP‖ packed on nearby PS domains.

From the standpoint of biomedical relevance, it is known that a specific arrangement of Fg molecules is required for blood clotting.[131,148,149,152,153] An extended organization process of Fg molecules in the formation of a fibrin network has been extensively studied in hemostasis and coagulation. The first step of the blood coagulation cascade is understood to be the conversion of

Fg to fibrin. Thrombin mediates this initial process by cleaving two Arg–Gly bonds in the Aα and Bβ chains of the E domain, generating fibrinopeptides A and B (FpA and FpB), as well as exposing the active sites of Gly-Pro-Arg-Pro (A-knob) in the Aα chain and Gly-His-Arg-Pro (B-knob) in the Bβ chain.[148,149,153]Subsequently, fibrin is assembled via nonconvalent interactions with these active sites in the E domain of Fg and their complementary binding sites known as hole "a" and hole "b" in the D domains of neighboring Fg molecules.[150,154]This process establishes D–E contacts between neighboring Fg molecules in a half-staggered manner, yielding protofibrils with Fg molecules arranged in two rows. Eventually, αC chains play an important role for these protofibrils to assemble into a three-dimensional network of fibrin clots. More recently, it has also been reported that similar extended arrangements of Fg molecules and fibrin prototypes can be induced through surface-controlled activation, without undergoing the thrombin-mediated process.[85,155]In my study, investigating Fg assemblies on dsa PS-*b*-PMMA provided insight into the protein organization behavior by allowing Fg molecules to neatly pack into aligned polymeric rows. The organization of Fg molecules on the dsa PS-*b*-PMMA surface in Figure 11B appears to be similar to the protein arrangements proposed in the above-discussed studies, although the exact stacking between Fg molecules in adjacent rows occurs in a quarter-staggered than half-staggered manner.

2.2.6 Effect of BCP Surface Periodicity on Fibrinogen Coverage

The Fg adsorption behavior on the random copolymer surface of PS-*r*-PMMA is shown in a series of AFM topography panels in Figure 12. PS-*r*-PMMA contains random length units of PS and PMMA that are arbitrarily distributed on the surface with their length scale on the molecular level, significantly smaller than the length of Fg. I observed that overall for the same protein concentration, fewer Fg molecules were adsorbed on the random copolymer templates than on the

other three block copolymer systems. In order to substantiate the protein surface density and the associated protein surface coverage on various polymeric surfaces, statistical analyses of surface-adsorbed Fg molecules were performed on the random as well as the three block copolymer samples by examining at least 20 independent locations of 1 μm^2 in size. The resulting statistical outcomes are tabulated in Table 2 for the number of adsorbed Fg molecules and the respective surface coverage of Fg.

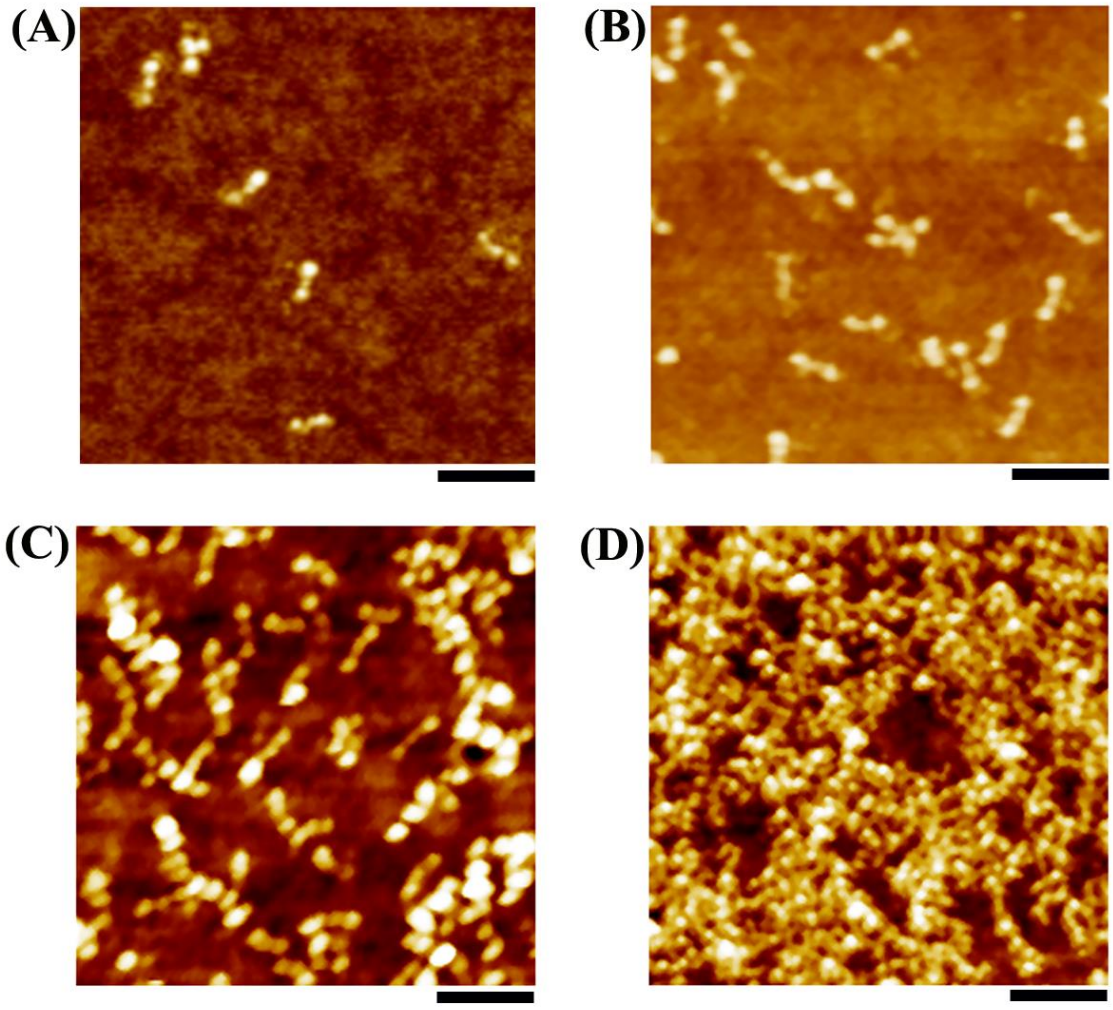

Figure 12. Atomic force microscopy topography panels display fibrinogen molecules adsorbed on the PS-r-PMMA surface at protein concentrations of (A) 2.5, (B) 12.5, (C) 25, and (D) 50 µg/mL. The scale bar under each AFM frame corresponds to 100 nm.

Table 2. Number of Fibrinogen Molecules, Surface Density of Adsorbed Fibrinogen, and Protein Surface Coverage Found on the Different Polymeric Surfaces at Various Protein Concentrations[a]

pattern type	Fg concn (μg/mL)	no. of Fg molecules/μm^2	density of adsorbed Fg (mg/m^2)	surface coverage (%)
dsa PS-*b*-PMMA	2.5	21.5 ± 4.8	0.011 ± 0.002	1.8 ± 0.4
	12.5	131 ± 18.7	0.066 ± 0.009	10.8 ± 1.5
	25	459 ± 74	0.23 ± 0.037	37.8 ± 6.1
sm PS-*b*-PMMA	2.5	14.6 ± 3.5	0.007 ± 0.002	1.2 ± 0.3
	12.5	141 ± 18.8	0.071 ± 0.009	11.6 ± 1.6
	25	349 ± 43	0.17 ± 0.022	28.8 ± 3.5
com PS-*b*-PMMA	5	80 ± 8.5	0.04 ± 0.0043	6.6 ± 0.7
	20	221 ± 19.4	0.11 ± 0.0097	18.2 ± 1.6
	50	360 ± 30.4	0.18 ± 0.015	29.7 ± 2.5
PS-*r*-PMMA	2.5	17 ± 4	0.0085 ± 0.0020	1.4 ± 0.3
	12.5	73 ± 7	0.037 ± 0.0035	6.0 ± 0.5
	25	277 ± 19.4	0.14 ± 0.0097	22.9 ± 1.6

[a]I define 100% surface coverage as the adsorption condition under which the entire surface area of the underlying polymeric template is completely covered by the adsorbed Fg, regardless of the chemical make-up of the nanodomain.

The more preferred surface adsorption of Fg onto the sm PS-*b*-PMMA and dsa PS-*b*-PMMA relative to the PS-*r*-PMMA surface observed in the analysis indicates that the presence of chemical interfaces on the size regime comparable to the protein length scale promotes protein adsorption compared with the same constituent chemical repeat-units distributed in a much smaller length scale relative to that of the protein. In earlier studies involving globular proteins, their distance-dependent adsorption behavior was elucidated as a function of the position to the nearest PS/PMMA interface.[81] Proteins such as immunoglobulin G and fibronectin preferred to adsorb on the PS domain region close to the PS/PMMA interface.[81–83,156,157] This effect was studied by varying the surfaces from diblock to blend to homopolymer, which systematically increased the size scale associated with the distance between the nearest PS/PMMA interfaces on each surface.[81] It was found that protein adsorption was favored the most when the distance between the nearest PS/PMMA interfaces was commensurate with the size of the protein. My observation

reported in this study confirms that the role of size-compatible chemical interfaces in promoting surface adsorption of proteins is not limited to globular proteins but extends to the elongated protein of Fg. By comparing the Fg adsorption between the chemical interfaces present on the diblock versus random copolymers, my data also substantiate that the optimal protein adsorption condition can be obtained by tuning the periodicity of the chemical interfaces to be compatible to the protein size length, and not by simply shrinking the size scale of the distribution of constituent chemical repeat units as was the case for PS-*r*-PMMA.

2.2.7 Effect of BCP Surface Alignment on Fibrinogen Coverage

I subsequently investigated the alignment effect of the polymeric nanodomains by comparing Fg adsorption characteristics between the BCP templates of similar repeat spacing but in aligned versus random fingerprint-like nanodomain patterns. Fg favored adsorption onto the aligned dsa PS-*b*-PMMA relative to the randomly oriented sm PS-*b*-PMMA. While this effect was not apparent at lower protein concentrations of 2.5 and 12.5 μg/mL, it was more pronounced as the concentration was increased to 25 μg/mL. Although the nanodomain periodicities are similar on the two BCP templates, more PS/PMMA interfacial areas can be found on the sm PS-*b*-PMMA surface becaise it presents a higher number of topological defects in the nanodomains than those on dsa PS-*b*-PMMA due to the formation of dislocations and disclinations.[122] This may keep the surface-bound Fg density on sm PS-*b*-PMMA higher than that on dsa PS-*b*-PMMA at lower protein concentrations, but the amount of protein molecules involved in the surface adsorption is not sufficiently high under these concentration regimes for the increased chemical interfaces on sm PS-*b*-PMMA to result in a significant difference in protein density. The net effect, therefore, kept the surface-bound Fg densities on the two surfaces similar to each other for these low concentrations. In contrast, at higher concentrations, the protein–polymer surface interaction is

mediated by the growing role of protein–protein interactions. In these cases, the surface adsorption of the protein is not only influenced by its own configuration with respect to the underlying polymeric nanodomains but also by the arrangement of other adsorbed protein molecules in the vicinity. On the well-aligned dsa PS-*b*-PMMA surface, a larger number of Fg molecules could be accommodated in the end-to-end geometry on the straight PS domains. Comparatively on the sm PS-*b*-PMMA surface with random nanodomain orientations, such space-packing capacity via the end-to-end stacking of the proteins was often limited by those molecules configured in TP, which occurred at a higher frequency than on the aligned polymeric surface for the same protein deposition conditions. The stacking continuity of Fg molecules in an end-to-end manner was often terminated or disrupted at these sites.

In order to substantiate this observation, I carried out a statistical analysis of Fg configurations found on dsa PS-*b*-PMMA, sm PS-*b*-PMMA, and com PS-*b*-PMMA. The occurrence events of the three Fg adsorption configurations, $SP_{\parallel}$, $SP_{\perp}$, and TP, are catalogued in Table 3. As discussed earlier, the most notable difference between the Fg adsorption configurations on the three BCP surfaces was the absence of $SP_{\perp}$ on the nanodomain templates with a periodicity smaller than the Fg length. The fraction of TP *versus* $SP_{\parallel}$ compared for a given concentration was much higher on sm PS-*b*-PMMA than on dsa PS-*b*-PMMA. When I assessed the Fg adsorption configurations among the three surfaces, other trends also began to emerge. Overall, a higher proportion of TP than SP was found on dsa PS-*b*-PMMA and sm PS-*b*-PMMA at lower protein concentrations, which turned into a $SP_{\parallel}$-dominant scenario with increasing concentrations. In fact, a similar phenomenon of a TP to SP transition was also observed from com PS-*b*-PMMA. However, the com PS-*b*-PMMA surface allowed Fg molecules to shape into both $SP_{\parallel}$ and $SP_{\perp}$ configurations at a higher concentration. Within the SP-configured Fg molecules on

com PS-*b*-PMMA, the occurrence frequency of $SP_{\perp}$ became greater with increasing protein concentrations.

Table 3. Ratios among the Three Fibrinogen Configurations of TP, $SP_{\parallel}$, and $SP_{\perp}$ Measured on the Different Polymeric Templates

		Fg configuration		
pattern type	**Fg concn (μg/mL)**	**$SP_{\parallel}$ (%)**	**$SP_{\perp}$ (%)**	**TP (%)**
	2.5	47.4	0	52.6
dsa PS-*b*-PMMA	12.5	65	0	35
	25	77.5	0	22.5
	2.5	48.1	0	51.9
sm PS-*b*-PMMA	12.5	54.4	0	45.6
	25	62.2	0	37.8
	5	60	0	40
com PS-*b*-PMMA	20	60	15	25
	50	52	28	20

2.2.8 Side-on versus End-on Surface Filling Geometry of Fibrinogen

The dominant surface-filling geometries of $SP_{\perp}$ and $SP_{\parallel}$ from tightly packed Fg molecules found on com PS-*b*-PMMA and dsa PS-*b*-PMMA, respectively, were further examined. The AFM data in Figure 13 present the distinctly different surface packing behavior of Fg and its preferred stacking configuration associated with com PS-*b*-PMMA and dsa PS-*b*-PMMA at their respective monolayer forming conditions. At monolayer forming conditions on com PS-*b*-PMMA, Fg molecules packed themselves with the entire D–E–D protein domains confined within the PS domains of com PS-*b*-PMMA in a side-to-side geometry, while orienting the protein long axis perpendicular to the nanodomain major axis. This side-on packing behavior of $SP_{\perp}$ Fg molecules prevalent on com PS-*b*-PMMA is clearly displayed in the AFM panels shown in Figure 13A. In contrast, the dominant Fg configuration on dsa PS-*b*-PMMA surface was $SP_{\parallel}$ with increasing protein concentration and surface coverage. Under monolayer forming conditions, Fg molecules predominantly configured in $SP_{\parallel}$ organized themselves in straight lines on the well-aligned PS

domains of dsa PS-*b*-PMMA. Within a given PS domain, the D–E–D axis of the protein was parallel to the nanodomain main axis, whereas the staggered stacking nature of the same protein subdomains could be seen between the Fg molecules assembled across neighboring PS domains. This end-on packing behavior of $SP_{\parallel}$ Fg molecules is displayed in the AFM images in Figure 13B. The average end-to-end distance of the staggered $SP_{\parallel}$-packed Fg molecule (D–E–D) is approximately 47.5 nm, which is comparable to Fg lengths reported in X-ray and EM studies.[129,130,132,150,158] The data show that the use of PS-*b*-PMMA with periodicity much smaller than or comparable to the length of Fg can lead to different Fg scaffolds with the protein backbone aligned parallel or perpendicular, respectively, to the nanodomain major axis. Hence, my results demonstrate that the orientation of Fg molecules can be effectively tuned during their self-assembly by controlling the physical dimensions of the underlying BCP templates.

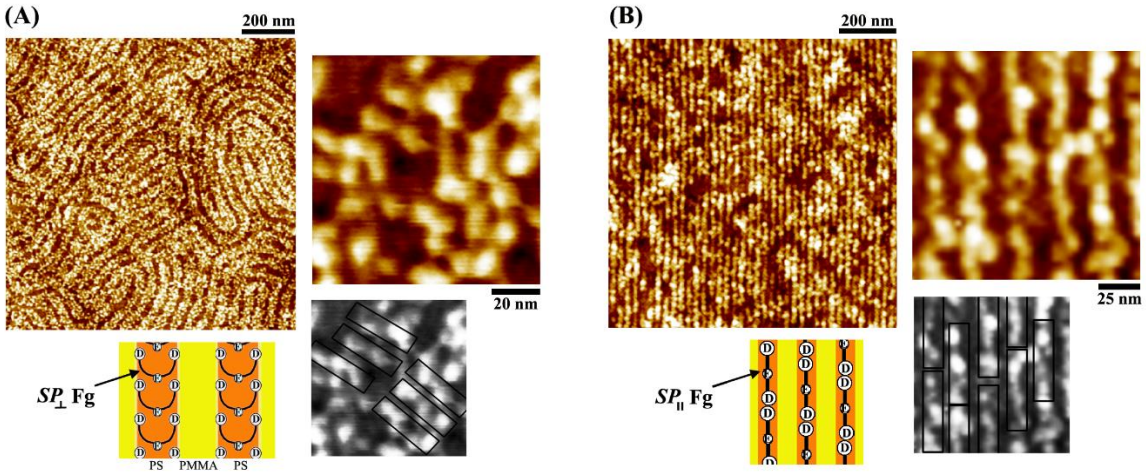

Figure 13. Atomic force microscopy topography images show both the large scale and zoomed-in frame views of fibrinogen molecules tightly packing on the PS domains of the (A) com PS-*b*-PMMA and (B) dsa PS-*b*-PMMA surface. The Fg concentrations used to produce the surface saturating coverage were 100 μg/mL for (A) and 50 μg/mL for (B). Under monolayer forming conditions, $SP_{\perp}$-configured Fg molecules stack themselves on the com PS-*b*-PMMA template in a side-on packing geometry. In contrast, $SP_{\parallel}$-configured Fg molecules line up end to end in a single file on each row of the PS domains of dsa PS-*b*-PMMA, yielding an end-on packing geometry. As a guide to the eye, boxes surrounding individual Fg molecules are inserted in the gray panel under the magnified AFM panel.

I note that the particular experimental conditions used in this study involved Fg adsorption from relatively dilute concentrations. Regardless of the isolated or interacting cases discussed so far, the experimental conditions yielded, on average, an adsorption of less than 1% of the total Fg molecules in the bulk solution. Therefore, in my measurements, the surfaces were examined at a very early point in time before they were fully covered by Fg. I have previously determined that ~2 mg/m^2 of adsorbed Fg was needed to produce a completely saturated adlayer of the protein on the PS-*b*-PMMA. Under this condition, the topography of the adsorbed proteins no longer showed the characteristic fingerprint patterns of the underlying diblock polymeric nanodomains.[84] Although evaluated on surfaces other than PS-*b*-PMMA, similar surface coverage values of ~1.4–4 mg/m^2 were previously reported for Fg adsorption onto silicon, silica, stainless steel, Ni–Ti alloy, and pure Ti.[159–162] Ellipsometry, *in situ* total internal reflection fluorescence microscopy, and *ex situ* wavelength dispersive spectroscopy were employed in these studies that investigated Fg adsorption at a pH and ionic strength similar to what were used in my experiments. Hence, the isolated and packed Fg configurations on the various PS-*b*-PMMA templates reported in my work shed light on the Fg adsorption behavior at the very dilute concentration regime, far from the equilibrium region considered in a typical adsorption isotherm plot.[19,159]

To date, only a limited number of studies are available for visualizing the exact assembly structures of Fg or fibrin monomers.[141,163,164] In one endeavor, early stages of fibrin-clot formation were investigated by transmission electron microscopy, and it resolved various fibrin structures such as monomers through tetramers, protofibrils, and fibers.[164] Another recent research effort has employed AFM to image the arrangement of the αC regions during the network formation of fibrin protofibrils and fibers.[141] Demonstrated by these stimulating efforts, further studies enabling direct and clear visualization of Fg molecules and the spatial assembly of individual Fg molecules can

be highly beneficial in understanding the structural and functional consequences of Fg molecules and their biological derivatives. In my study focusing on the ultrahigh resolution AFM imaging of the local and extended assembly of Fg molecules at the single protein and protein subdomain level, I unambiguously present the exact configuration and packing geometry of individual protein molecules in the large-scale network of assembled Fg specific to different PS-*b*-PMMA templates. I provide direct evidence of the polymeric surface-specific adsorption configurations of single proteins at early adsorption stages as well as the assembly features between individual proteins leading to large scale surface packing. In doing so, I provide insight into protein adsorption and organization not only for a few limited sets of Fg molecules in isolated areas under a low surface loading condition, but also for a large number of Fg molecules cooperatively organized in monolayer forming conditions on PS-*b*-PMMA.

Further expanding on these endeavors, biological functionalities of the BCP-bound Fg were examined in order to demonstrate the usefulness of the Fg/BCP scaffolds in potential biological applications such as assembling nanoparticles and activating cells on these Fg/BCP constructs. Self-assembled Fg molecules forming a monolayer on the PS domains of com PS-*b*-PMMA were used for assessing these capabilities, first for nucleating bioceramic nanoparticles (NPs) and second for activating microglial cells.

2.2.9 Calcium phosphate NP Nucleation and Growth on Fg/BCP Scaffold

I employed the Fg/com PS-*b*-PMMA construct in the nucleation and growth of calcium phosphate (Ca–P) NPs. Ca–P materials such as hydroxyapatite represent biomedically important materials, often used to coat the surface of implant biomaterials in order to increase their biocompatibility and to accelerate integration with living tissues.[165] Conventionally, these Ca–P coatings are applied to implant materials via specialized multistep routes such as physical vapor deposition,

ion-beam or radio frequency sputtering, dip coating, and plasma spraying.[166–170] The high temperature and gas phase processes associated with these techniques cannot be easily adapted for use under ambient conditions or made readily compatible with incorporation of biological molecules. In several earlier studies, Ca^{2+} ions were successfully nucleated on carboxylic moieties on the surface,[171–173] which further led to nucleation and growth of Ca–P particles. In addition to the carboxylic acid groups present in Fg, both high and low affinity Ca^{2+}binding sites are known to be present in Fg. Hence, I examined whether the Fg/com PS-*b*-PMMA scaffold can serve as an alternative to the conventional Ca–P coating processes via a bottom-up approach to grow Ca–P NPs, whose experimental conditions to initiate the nucleation and growth of Ca–P NPs can be well-suited for easy operation at room temperature and incorporation of biomolecules. The AFM data in Figure 14 clearly show that Ca–P NPs preferentially adhere on the Fg monolayer assembled on the PS domains of the com PS-*b*-PMMA template. In the topography data of AFM, Figure 14A, the Ca–P NPs formed after 5 min incubation of the Fg/com PS-*b*-PMMA construct in the Ca–P growth solution are seen as white spheres protruded on the Fg layer with a particle size of approximately 20 nm in diameter. The NPs grew over time to larger sizes reaching diameters of 50–100 nm with a prolonged incubation of 7 h, as displayed in Figure 14B. On the control substrate of com PS-*b*-PMMA without the presence of adsorbed Fg, the selective nucleation behavior of Ca–P NPs on the Fg-decorated PS domains of com PS-*b*-PMMA was not observed. Rather, Ca–P NPs were found to nucleate on both the PS and PMMA domains of the blank com PS-*b*-PMMA template without Fg, as displayed in Figure 15. These outcomes suggest that my self-assembly based, Fg/PS-*b*-PMMA approach can be used to prepare Ca–P layers on various implant materials by simply interfacing the different material types and shapes with a thin layer of Fg/PS-*b*-PMMA. The demonstrated application of Fg/PS-*b*-PMMA scaffolds in Ca–P NP growth may be able to

provide a simple and straightforward means for aiding biocompatible coating processes by permitting mild operation conditions in ambient and aqueous environments.

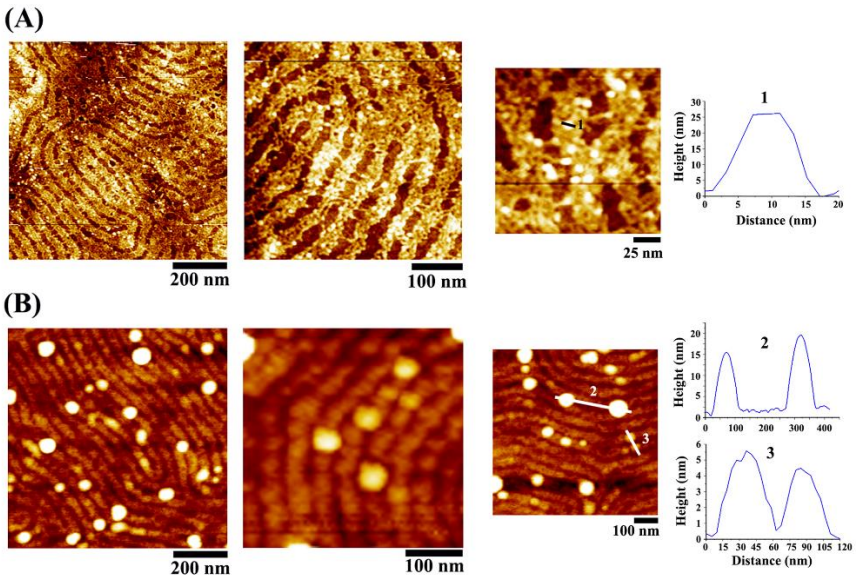

Figure 14. Atomic force microscopy topography panels show that calcium phosphate nanoparticles preferentially nucleate and grow on the Fg assembled areas of the com PS-*b*-PMMA template. Data provided in panels A and B pertain to the Fg/com PS-*b*-PMMA incubation conditions of 5 min and 7 h in the Ca–P growth solution. The typical particle sizes are shown in the line analysis data provided for the two different incubation periods.

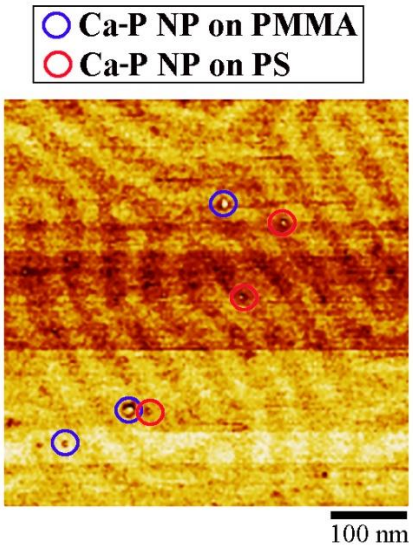

Figure 15. The data shown in the AFM phase panel display Ca-P NPs formed on com PS-b-PMMA without any surface-bound Fg. The nucleation of Ca-P NPs occurs both on PS and PMMA domains of the blank PS-b-PMMA template in this case. The Ca-P NPs formed on the PMMA and PS domain are marked with the blue and red circle in the image, respectively.

2.2.10 Fg/BCP in Microglia Cell Activation

I carried out an additional experiment to confirm the ability of surface-bound Fg molecules to retain their biofunctionality upon adsorption to PS-*b*-PMMA. The model cell chosen for this test was microglia, which represents the primary immune cells of the central nervous system. Although Fg has been primarily examined for its roles in blood coagulation, many studies indicate that Fg also plays a pivotal role in inflammatory response and host defense as a classic acute-phase reactant.[174–177] In relation to the role of Fg in microglia cell activation, it is known that immobilized Fg can dramatically affect microglia activation, which leads to changes in cell size, morphology, and function.[178–180] Binding sites for Fg's cellular receptors regulating the inflammatory process have been characterized.[178,181] Therefore, I assessed the biofunctionality of PS-*b*-PMMA immobilized Fg in microglia cell activation by culturing microglia cells on Fg-treated com PS-*b*-PMMA scaffolds as well as on untreated com PS-*b*-PMMA substrates. After cell culture was completed under identical environments on the control (com PS-*b*-PMMA) and test (Fg/com PS-*b*-PMMA) substrates, the microglia cells were immunostained to compare the degree of activated cells on the com PS-*b*-PMMA substrates with and without immobilized Fg.

The fluorescence panels shown in Figure 16 display representative images of immunostained microglia cells observed on the com PS-*b*-PMMA (Figure 16A) and Fg/com PS-*b*-PMMA (Figure 16B) plates. Pronounced fluorescence emissions of green and red signals were observed from the Fg/com PS-*b*-PMMA relative to the untreated com PS-*b*-PMMA plate. CD11b, the β-integrin marker of microglia, is responsible for the red emission, and the increased expression of CD11b of the cells on Fg/com PS-*b*-PMMA is associated with microglial activation.[182] The red emission is due to activated microglia expressing inducible NO synthase (iNOS) for producing an excessive amount of NO.[183] Similar to the signal from CD11b, the fluorescence emission from

iNOS was also found to be markedly higher in the cells grown on Fg/com PS-*b*-PMMA. From these microglia cell culture outcomes, I verify that Fg molecules, even in the PS-*b*-PMMA surface-bound state, retain their biological functionality.

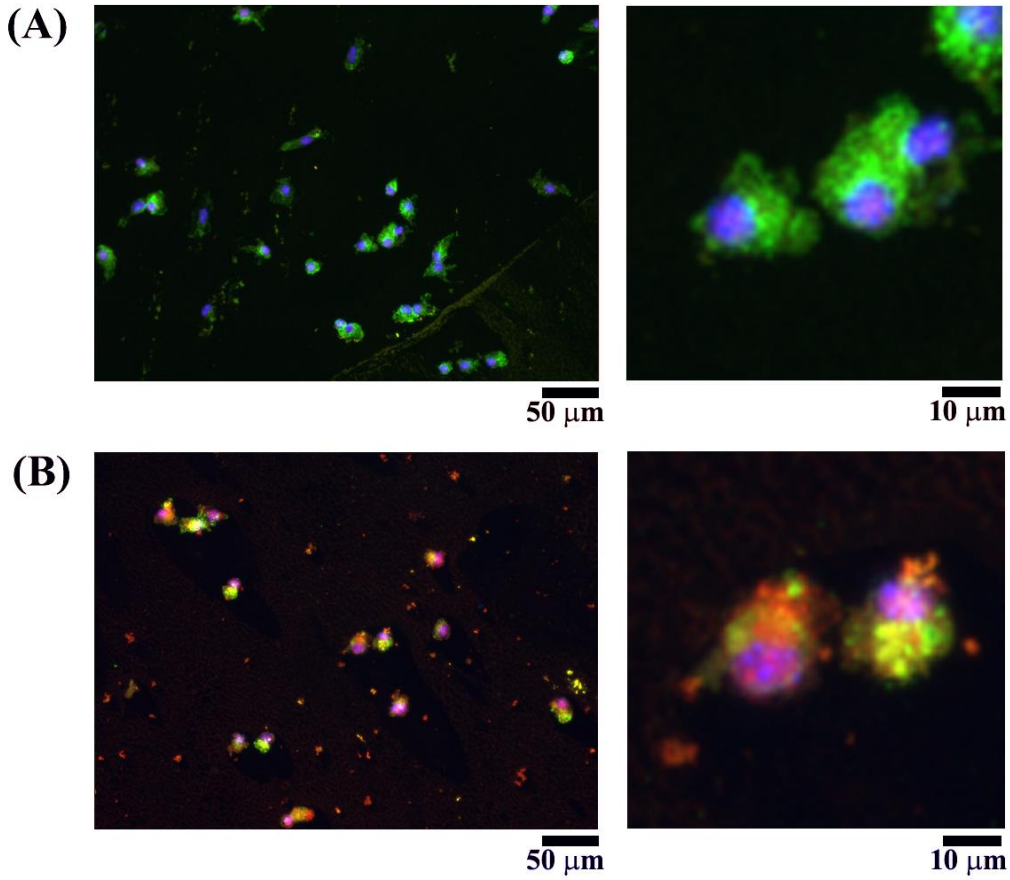

Figure 16. Primary mouse microglial cells grown on (A) com PS-*b*-PMMA and (B) 25 μg/mL Fg-deposited com PS-*b*-PMMA were immunostained for DAPI (blue), iNOS (green), and CD11b (red). The resulting fluorescence panels of the immunostained microglia show that Fg proteins are biofunctional in activating the cells, even after their surface adsorption to com PS-*b*-PMMA.

2.3 Conclusions

I have revealed the distinct adsorption configurations and the characteristic organization behaviors of Fg proteins affected by the periodicity and orientation of the chemically alternating nanodomains on various BCP surfaces. Precise effects of nanodomain periodicities as well as nanodomain alignments were examined not only for the adsorption of several Fg molecules in

isolation but also for the assembly of many Fg molecules in large scale surface packing. By unambiguously and faithfully resolving each Fg molecule, as well as the nanosized features on various block copolymer surfaces, the exact subdomain-specific configurations of Fg molecules and the preferred packing geometries between different Fg molecules were elucidated at both low and high surface coverage via direct visualization. I further demonstrated that the surface-bound Fg molecules could serve as chemical and biological guides to selectively seed bioceramic NPs. I also showed that Fg molecules retained their biological functionality in activating microglial cells even in their surface-immobilized state. My efforts will provide valuable and timely insight into controlling specific adsorption and packing behaviors of the biomedically important protein of Fg by tuning their effective surface adsorption and assembly characteristics through modulating the periodicity and orientation of the underlying polymeric nanodomains. My approach to create the resulting Fg construct has the advantages of straightforwardly providing well-defined protein density, periodicity, orientation, and retained biofunctionality.

2.4 Methods

2.4.1 Preparation of Polymeric Substrates

2.4.1.1 com PS-b-PMMA

com PS-*b*-PMMA surfaces were prepared from PS-*b*-PMMA diblock copolymer (71% PS by weight) with an average molecular weight of 71.4 kDa and a polydispersity of 1.06, which was obtained from Polymer Source Inc. (Montreal, Canada). An ultrathin film of com PS-*b*-PMMA was generated by spin coating a 2% (w/v) solution of the specified PS-*b*-PMMA in toluene at 3500 rpm for 1 min on precleaned Si surfaces. The com PS-*b*-PMMA substrate was subsequently annealed in an Ar atmosphere at 220 °C for 8 h with a transient ramp-up rate of 5 °C/min and a cooling rate of 2 °C/min. This thermal annealing process induced phase separation of the PS and

PMMA chains in com PS-*b*-PMMA, yielding periodically alternating and chemically varying nanodomains known as half-cylinders and exposing repeating stripes of PS and PMMA blocks at the air/polymer interface with repeat units of 45 nm (PS to PS distance).

2.4.1.2 PS-r-PMMA

A 1.0 wt % solution of poly(styrene-*r*-methyl methacrylate-*r*-glycidyl methacrylate) (PS-*r*-PMMA)[184] with a STY/MMA/GMA mole ratio of 58:40:2, a molecular weight of 12.4 kDa, and a polydispersity of 1.31 was prepared by dissolving the random copolymer (95 parts by weight) and *p*-nitrobenzylsulfonic acid tosylate (p-NBT, 5 parts by weight) thermal acid generator in PGMEA (10000 parts by weight). The solutions were passed through a 0.2 μm polytetrafluoroethylene (PTFE) filter prior to spin coating the solution onto a Si wafer at 2000 rpm. The PS-*r*-PMMA coated wafer was baked at 205 °C for 2 min and cooled to room temperature. The PS-*r*-PMMA was then given a solvent rinse by exposing the sample to a pool of PGMEA for 30 s followed by spin drying at 2000 rpm for 30 s to remove any excess random copolymer that was not cross-linked or grafted to the wafer surface.

2.4.1.3 sm PS-b-PMMA

A 1.2 wt % solution of lamellar PS-*b*-PMMA (50% PS by weight, obtained from Polymer Source Inc.) was made in propylene glycol monomethyl ether acetate (PGMEA) and passed through a 0.2 μm PTFE filter. The resulting solution was spin coated at 3000 rpm for 30 s on a Si substrate precoated with a nonpreferential underlayer of PS-*r*-PMMA as described above. After spin-coating the sm PS-*b*-PMMA ultrathin film on top of this underlayer-treated Si substrate, the sample assembly was annealed at 255 °C for 2 min followed by immediately cooling to room temperature. Under these thermal annealing conditions, the BCP domains formed a random fingerprint pattern of a perpendicular lamellae morphology with lamellar domains of PMMA and

PS both present at the air/polymer interface. The pitch of the lamellae was 25 nm (PS to PS distance).

2.4.1.4 dsa PS-b-PMMA

Aligned lamellar nanodomains of alternating PS and PMMA were obtained using a chemoepitaxy DSA process (the so-called LiNe DSA flow) described elsewhere.(24) Briefly, a cross-linkable polystyrene (xPS) solution (EMD Performance Materials, AZEMBLY NLD-128) was spin coated on top of a SiN/amorphous carbon (α-C) stack and baked at 315 °C for 5 min under a N_2environment. An ArF immersion resist was then coated on the xPS/SiN/α-C stack, exposed with a 193 nm immersion scanner, and developed with a standard developer of 0.26 *N*-tetramethylammonium hydroxide (TMAH) solution. This process subsequently generated grating patterns with a periodicity of 84 nm. The patterned resist on the xPS/SiN/α-C stack was then etched via reactive ion etching to remove the xPS layer that was not covered by the resist. The remaining resist was subsequently removed by 0.26 N TMAH. As a result, 8 nm-thick xPS gratings with 84 nm pitch were generated on top of the SiN/α-C stack. On the pattern of the xPS gratings, a poly(styrene-*r*-methyl methacrylate) brush material with 51% STY content (AZEMBLY NLD-127) was coated and baked at 250 °C for 5 min followed by a PGMEA rinse to remove any nongrafted brush material. This process resulted in the formation of alternating stripes of xPS and the neutral brush material. Next, a lamellar PS-*b*-PMMA BCP solution in PGMEA (AZEMBLY PME-120) was spun on the prepattern at 2000 rpm for 30 s followed by annealing at 250 °C for 10 min. The resulting substrate was immediately cooled to room temperature to obtain the aligned gratings of alternating PS and PMMA lamellar domains. The pitch of the aligned lamellae was 28 nm (PS to PS distance).

2.4.2 Preparation of Fibrinogen -Bound Substrates

Human plasma Fg was received from VWR Scientific Inc. (West Chester, PA) in a lyophilized form and reconstituted in PBS buffer (10 mM mixture of Na_2HPO_4 and NaH_2PO_4, 140 mM NaCl, 3 mM KCl, pH 7.4). The reconstituted protein solution was then diluted to various concentrations ranging from 2.5 μg/mL to 100 μg/mL. A 10 μL volume of Fg solution with a desired concentration was deposited on the polymeric substrate under study for 20 s. The sample surfaces were carefully rinsed with PBS multiple times and gently dried under a stream of N_2 prior to AFM.

2.4.3 Calcium phosphate Nanoparticle Nucleation and Growth

Reagent-grade chemicals of $CaCl_2{\cdot}2H_2O$, $Na_3PO_4{\cdot}12H_2O$, and $NaHCO_3$ were received from EMD Millipore Corp. (Billerica, MA). Ca–P NPs were prepared by using a method similar to what was previously reported.[173,185] Briefly, 2.5 mM $CaCl_2$ solution was mixed in a volume ratio of 1:1 with another solution prepared with 2.5 mM Na_3PO_4 and 18 mM $NaHCO_3$. The mixed solution containing the calcium and phosphate sources was then deposited on the Fg-treated com PS-*b*-PMMA plate and left for incubation at 37 °C up to 7 h in a humidity-controlled chamber. After incubation with the Ca–P solution, the sample surface was subsequently rinsed with an ample amount of deionized water and dried under N_2 stream before AFM imaging.

2.4.4 Microglia Cell Activation

C57/Bl6 mice were used in accordance with the approved protocols established by the Institutional Animal Care and Use Committee (IACUC) of Georgetown University. Primary microglia cultures were prepared from P3–P7 cortices similar to the previously reported procedures.[186] Both mixed glia cultures and isolated microglia were maintained in Dulbecco's modified Eagle's medium (DMEM) containing glutamine (Corning), 10% fetal calf serum (Sigma-

Aldrich), 100 U/mL penicillin/streptomycin (GIBCO), and 0.25 μg/mL amphotericin B (GIBCO). Untreated and Fg-treated com PS-*b*-PMMA substrates were placed at the bottom of well plates into which microglia cells were subsequently seeded at a density of 10^5 cells/well. To analyze the effect of immobilized Fg on microglia activation, cells were left to incubate on the control and test substrates for 24 h in the same media described above. Microglia cells on the substrates were fixed for 10 min in 4% paraformaldehyde and incubated for 1 h in a blocking buffer containing 5% normal goat serum and 0.3% Triton X-100 made in PBS. To further prepare the cells for immunostaining, rat anti-CD11b (AbD Serotec) and mouse anti-iNOS (BD Pharmingen) were incubated overnight at 4 °C in the same blocking buffer. After washing the cells with PBS three times for 10 min per cycle, the secondary antibodies of Alexa 488-labeled goat anti-rat immunoglobulin G (Life Technologies) and Alexa 594-labeled goat anti-mouse immunoglobulin G (Life Technologies) as well as 300 nM DAPI (Sigma) were added for 2 h. Three consecutive PBS washes were then repeated three times; the Fg-treated and untreated com PS-*b*-PMMA plates containing microglia cells were mounted on coverslips with Fluoromount-G (SouthernBiotech) before fluorescence detection.

2.4.5 Characterization

Both the individual Fg proteins and the nanoscopic details of the underlying polymeric templates were profiled by performing high resolution AFM imaging. Subsequently, for the AFM images, the topography and phase scans were performed with a MultiMode 8 AFM interfaced with a Nanoscope V controller (Bruker Corp., Santa Barbara, CA), operating in a soft tapping mode at a scan speed of 1 Hz or lower using silicon tips with a typical resonant frequency of 60–70 kHz and a spring constant of ~1 N/m. Immunostained microglia cells were imaged using a Zeiss Axio Imager A2M microscope (Carl Zeiss, Inc., Thornwood, NY) equipped with an AxioCAM HRm

digital camera. The reflected fluorescence excitation was produced by a 120 W mercury vapor lamp (X-Cite 120Q). Three different filter modules allowed for the cell characterization of the blue, green, and red emission from the DAPI-labeled nuclei (325–390 nm excitation and 420–470 nm collection), Alexa 488-labeled CD11b (450–490 nm excitation and 510–540 nm collection) and Alexa 594-labeled iNOS (540–552 nm excitation and 575–640 nm collection), respectively. Images were acquired in a dark room setting using a 2 s exposure for Alexa 488 and 594 and a 150 ms exposure for DAPI through EC Epiplan-NEOFLUAR 50× (numerical aperture, NA = 0.8) and 20× (NA = 0.5) magnification objective lenses. Images were analyzed using the processing software AxioVision (Carl Zeiss, Inc.) and ImageJ (a Java-based program).

3 Ascertaining effects of nanoscale polymeric interfaces on competitive protein adsorption at the individual protein level

3.1 Introduction

In this study, I undertook the challenge of revealing competitive protein adsorption processes specific to a nanosized surface regime using a model, binary protein mixture. Specifically, I examine the competitive protein adsorption characteristics of a dual-component protein system of bovine serum albumin (BSA) and fibrinogen (Fg) and further elucidate the time- and concentration-dependent protein adsorption profiles on both chemically uniform and alternating polymeric surfaces at the individual protein level. I determine that the time-dependent transition behaviors of surface-bound proteins differ significantly on the polymeric surfaces of polystyrene (PS) homopolymer *versus* polystyrene-*block*-polymethylmethacrylate (PS-*b*-PMMA) diblock copolymer. The two polymeric systems represent adsorption cases in the absence of nanointerfaces for PS, *i.e.* presenting a chemical uniform surface at the macroscopic level, and in the presence of periodic nanointerfaces for PS-*b*-PMMA, *i.e.* presenting chemically alternating domains separated by PS: PMMA interfaces at the nanoscale. The desorption inertia, the extent to which the originally bound protein component resists its displacement due to other proteins in the bulk phase, is found to be much larger for a nanoscale, chemically alternating surface of PS-*b*-PMMA when compared to a similar adhesion scenario involving a chemically uniform surface of PS. Specifically, BSA, which preferentially binds to both surfaces at early times, is displaced by Fg much more slowly in the PS-*b*-PMMA relative to the PS case. This effect is evidenced by a significantly delayed appearance of the turnover window from BSA to Fg on the PS-*b*-PMMA surface.

This temporally extended, residence time of the initially bound protein species on PS-*b*-PMMA pertains uniquely to a nanoscale platform whose surface consists of periodically repeating, chemical

interfaces on the size scale of individual proteins. I explain the origin of this significant retardation to the onset of a protein exchange process on the surface which is characteristically observed in nanoscale competitive adsorption. My study marks the first endeavor to illuminate competitive protein adsorption processes specific to a nanoscale size regime, revealing the differences in the competitive protein adsorption processes occurring on polymeric surfaces with and without periodic nanointerfaces on the size scale of individual proteins. Such information will be highly beneficial to the functional design and application of biomaterials and biodevices with reduced dimensionality.

3.2 Experimental Section

Polymer substrates of PS and PS-*b*-PMMA were prepared from the homopolymer and diblock copolymer granules received from Polymer Source Inc. (Montreal, Canada). The average molecular weight of PS and PS-*b*-PMMA (71% PS by weight) is 152 kDa and 71.4 kDa, respectively, with the polydispersity of 1.06. Both chemically uniform (PS homopolymer) and alternating (PS-*b*-PMMA diblock copolymer) surfaces were made by spin coating 2% (w/v) polymeric solutions at 3500 rpm for 1 min on Si which was pre-cleaned with a series of solvents using ethanol, acetone, and toluene. Phase separation of PS-*b*-PMMA was subsequently achieved *via* thermal annealing in an Ar atmosphere at 240 °C for 6 h with a transient ramp-up rate of 5 °C $min^{-1}$and a cooling rate of 2 °C min^{-1}. This process yielded periodically alternating and chemically varying nanodomains known as half-cylinders and exposed repeating stripes of PS and PMMA blocks at the air/polymer interface with repeat units of 45 nm (PS to PS distance).[122,126] BSA and human plasma Fg were purchased from VWR Scientific Inc. (West Chester, PA). The lyophilized powders of BSA and Fg were reconstituted in PBS buffer (10 mM mixture of Na_2HPO_4 and NaH_2PO_4, 140 mM NaCl, 3 mM KCl, pH 7.4) and diluted to varying concentrations ranging from 0.025 to 5 μg ml^{-1}. A series of binary protein solutions was made by aliquoting and mixing BSA and Fg solution of desired concentrations. The concentrations of BSA/Fg

presented in this study are 5/0.5 μg mL^{-1}, 2.5/0.25 μg mL^{-1}, 1/0.1 μg mL^{-1}, 0.5/0.05 μg mL^{-1} and 0.25/0.025 μg mL^{-1}. The concentration ratio between BSA and Fg in the bulk solution was kept as 10:1 throughout my competitive adsorption study in order to mimic the typical range of the concentration ratio of the two proteins found in plasma. A volume of 10 μL of the binary protein solution was then delivered to the polymeric substrates and subsequently placed in a humidity-controlled chamber and left for incubation for periods ranging from 5 s to 48 h. After the incubation period, the sample surfaces were carefully rinsed with 120 μL PBS multiple times, followed by a gentle drying under a stream of N_2 before AFM imaging. Both the individual BSA and Fg proteins as well as the nanoscopic details of the underlying polymeric templates were profiled by performing high-resolution AFM imaging. Subsequently, time-lapse images for a given mixture of concentrations were acquired by imaging multiple, identically treated, samples with varying incubation times. For the AFM images, the topography and phase scans were performed with a MultiMode 8 AFM interfaced with a Nanoscope V controller (Bruker Corp., Santa Barbara, CA), operating in a soft tapping mode at a scan speed of 1 Hz or lower using silicon tips with a typical resonant frequency of 60–70 kHz and a spring constant of 1–5 N m^{-1}.

3.3 Results and Discussion

3.3.1 Physical and Chemical Characteristics of the Proteins and Polymeric Surfaces

SA is a heart-shaped protein with a molecular weight of approximately 66 kDa and is negatively charged at a physiologically relevant pH (pI = 4.8).[187–190] SA is comprised of three structurally similar helical domains of I, II, and III, and each domain can be divided into two subdomains of A and B.[191] The physical dimensions of SA are roughly 1.9 nm × 14 nm in height and diameter, respectively, as shown in Figure 17. Fg is a highly elongated protein also exhibiting negative charges (pI = 5.2) in a physiological environment and is composed of three interwoven polypeptide chains of Aα, Bβ and γ

that are connected together by 29 disulfide bonds.[6,187,192] The structure of the 340 kDa dimeric protein consists of rod-like chains spanning roughly spherical domains of D (at the two ends) and E (at the center). The height and length (spanning D–E–D domains) of Fg are approximately 2.3 nm × 55.5 nm, respectively, as shown in Figure 17. The physical and chemical characteristics of SA and Fg proteins are summarized in Table 4.

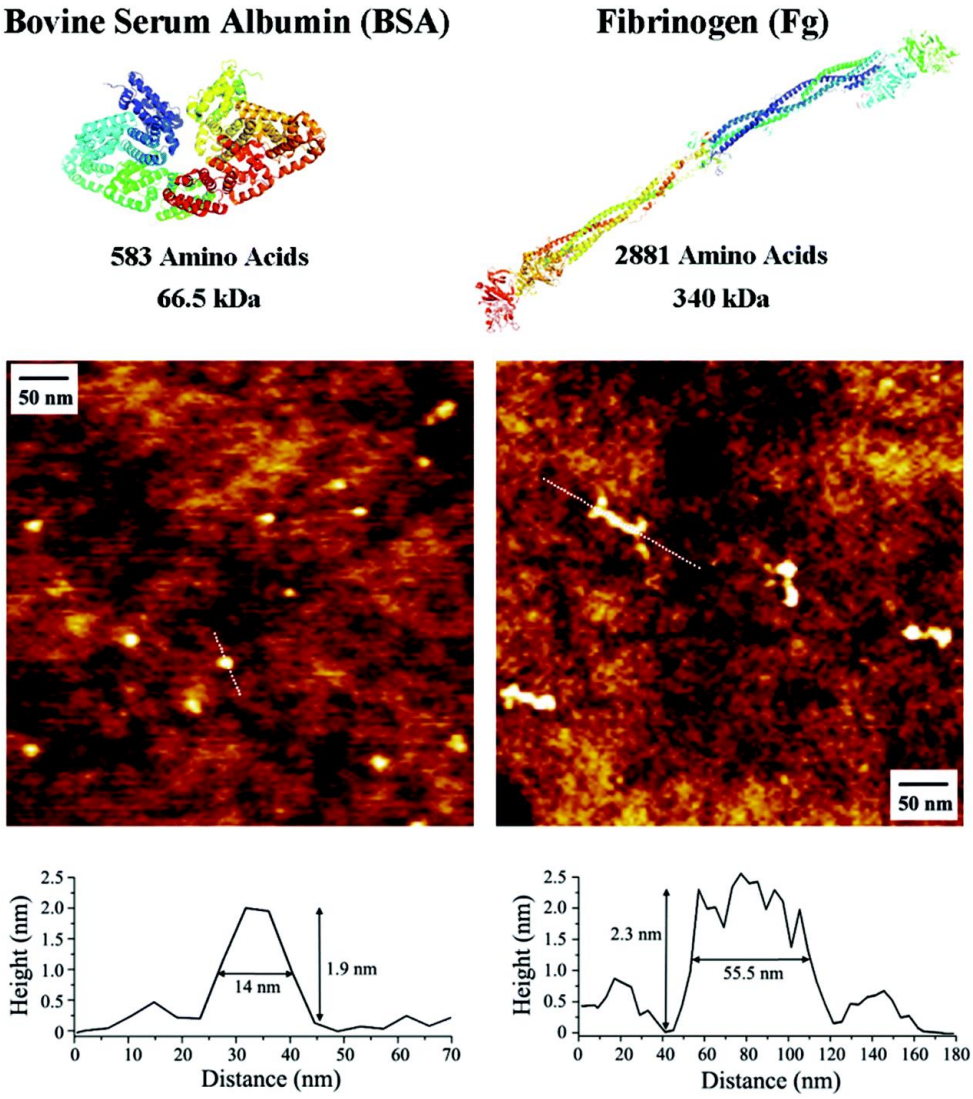

Figure 17. The colored ribbon structures show the two proteins under study, bovine serum albumin and fibrinogen. The spatial distributions of the amino acid chains of BSA and Fg are depicted to display its heart- and rod-shaped form, respectively. The AFM topography images display the typical sizes and shapes of individually resolved proteins adsorbed on PS foe isotropic BSA (left panel) and highly anisotropic Fg (right panel). Typical line analysis results of the proteins measured along the white lines in the AFM panels are found in the height versus distance profile for BSA (left) and Fg (right).

Table 4. Key physical and chemical parameters of Bovine Serum Albumin and Fibrinogen are charted

Protein	Molecular weight	Diffusion coefficient	Isoelectric point	Number of amino acid residues	Crystal cell dimension[a]	Physical size[b]	Concentration in plasma
SA (PDB no: 1E7I)	66 kDa	$6.1 \times 10^{-7} cm^2 s^{-1}$	4.8	~580	*a*, *b*, *c* = 215.7, 45.1, 142.4 Å	1.9 nm × 14 nm	~40 mg ml−1 ~600 μmol
Fg (PDB no: 3GHG)	340 kDa	$2 \times 10^{-7} cm^2 s^{-1}$	5.2	~2880	*a*, *b*, *c* = 135.24, 94.87, 300.81 Å	2.3 nm × 55.5 nm	~2.5 mg ml−1 ~7.5 μmol

[a]The values are taken from the protein data bank (PDB, http://www.rcsb.org) entry corresponding to the specified PDB number for SA and Fg. [b]The physical size was determined by my AFM measurements from the proteins adsorbed on PS.

BSA and Fg were chosen as the two model components in my binary protein adsorption study based on the wealth of knowledge on their bulk-scale and ensemble-averaged adsorption onto solid surfaces.[19,27,84,90,91,100,102,103,125,147,193] In addition, the large shape difference between BSA and Fg makes the identification of the two protein components straightforward *via* topographical inspection with AFM. A significant body of previous research in the area of biomaterials has provided insight on the adhesion phenomenon of BSA and Fg. Using techniques such as infrared spectroscopy,[19,27] fluorescence-based techniques,[90,91,125,193] SPR,[102,103] QCM,[19,99] XPS,[194] and AFM,[84,100,126,147] the collective adsorption characteristics of single component proteins as well as those of multicomponent protein mixtures have been examined for time-dependent surface adhesion profiles and orientational changes of the surface-bound proteins. In particular, BSA and Fg adhesion onto polymers have been probed on biomedically relevant substrates such as PS, PMMA, polyethylene (PE), polyethylene glycol (PEG), polyethylene oxide (PEO), and polydimethylsiloxane (PDMS),[89,126,195–199] although the majority of these previous studies pertained to chemically uniform, macroscopic scale, polymeric surfaces. Regardless of the number of protein components in the system under investigation, these prior studies have also concentrated on the collective adsorption characteristics from a large number of proteins, rather than resolving the sequence of adsorption events at the individual protein level. Different from

the majority of the aforementioned past studies, my work presented in this paper focuses on the examination of individual proteins at relatively low surface coverage up to a monolayer. This condition was stipulated to perform high resolution AFM imaging while faithfully resolving individual BSA and Fg proteins in their surface-bound state as well as the nanoscopic topological variations of the chemically alternating PS-*b*-PMMA surface.

PS homopolymer and PS-*b*-PMMA diblock copolymer are used in this study as the control and test surfaces, respectively, for the binary protein adsorption. Both PS and PMMA are widely exploited as biomedical substrates and products,[143] and their biotechnological relevance makes them suitable for my in-depth protein adhesion study. In addition, PS-*b*-PMMA diblock copolymer provides self-assembling, nanoscale patterns with a repeat spacing on the order of several tens of nanometers.[143,199] The surface consists of periodic and well-defined nanoscale surface patterns with distinctive PS and PMMA regions.[122,145] Therefore, the PS-*b*-PMMA diblock copolymer offers a high density of chemical interfaces defined by the PS and PMMA nanodomains on its surface, unlike the PS homopolymer surface where no chemical interfaces are present. With the use of the PS and PS-*b*-PMMA platforms, similarities and differences in the binary protein adsorption attributes that are correlated with the presence of nanoscopic features and chemical interfaces on the surface can be revealed.

The characteristic topographies of BSA and Fg on polymeric surfaces are shown in their corresponding AFM panels on the left and right in Figure 17, respectively. Owing to this large difference in shape anisotropy, BSA and Fg can be easily distinguished on the polymeric surfaces by simple visual inspection, especially for low surface coverage regimes, even though both protein species are simultaneously present on the surface.

3.3.2 Various Time-lapse Phases of the Binary Protein Adsorption

For competitive adsorption of the binary protein mixture on the polymeric surfaces, the two proteins were first combined into a mixture and then delivered onto the control and test platforms. The concentration ratio of the two proteins in the binary mixture was kept constant as BSA: Fg (10:1) in all my experiments, mimicking the typical range of the concentration ratio of the two proteins in plasma. This ratio yields BSA:Fg of approximately 50:1 in terms of the number of protein molecules in the bulk solution. By subsequently conducting time-lapse AFM measurements, I have identified various stages of competitive protein adsorption with increasing interaction time between the proteins and surface. The key stages of the competitive adsorption that are readily identifiable at the individual biomolecular level are the BSA-dominant phase, the Fg onset phase, the Fg turnover phase, and the Fg-dominant phase. In terms of the surface-bound protein counts of BSA and Fg, each of these four phases shows an approximate BSA:Fg ratio of less than 10:1 (BSA dominance), 10:1–5:1 (Fg onset), 5:1–1:10 (Fg turnover), and greater than 1:10 (Fg dominance) in my AFM panels. Figure 18 illustrates the progressive adsorption frames of the binary protein mixture on the control and test polymeric platforms. On both PS homopolymer and PS-*b*-PMMA diblock copolymer, the protein component predominantly adsorbed onto the surface initially was identified as BSA, with little to no Fg in view. Examples of this BSA-dominant phase are presented in Figure 18A(i) for the PS and in Figure 18B(i) for the PS-*b*-PMMA case. With increasing incubation time, more and more Fg molecules started to arrive and adhere to the polymeric surfaces, and both BSA and Fg were easily found on the surface. At this stage, BSA molecules were still abundantly found on the surface, but at least one out of ten protein molecules bound on the surface was revealed as Fg. Such Fg onset phase is displayed in Figure 18A(ii) and Figure 18B(ii) for the PS and PS-*b*-PMMA, respectively. Upon prolonged incubation with the protein mixture, the frequency of Fg molecules continued to increase on the surface, whereas the relative number of BSA

was reduced further. In this Fg turnover phase, at least one out of five surface-bound proteins were identified as Fg. The AFM panels corresponding to this stage are found in Figure 18A(iii) for the PS and Figure 18B(iii) for the PS-*b*-PMMA case. With further extended incubation, Fg molecules predominantly occupied the polymeric surfaces. Representative AFM frames of the Fg-dominant phase are displayed in Figure 18A(iv) for the PS and Figure 18B(iv) for the PS-*b*-PMMA platform. The percent surface coverage of the adsorbed proteins in the AFM panels of Figure 18A and B is approximately 3.5% (Figure 18A, i), 3.9% (Figure 18A, ii), 11.72% (Figure 18A, iii), and 47.6% (Figure 18A, iv) for the PS case and 2.7% (Figure 18B, i), 5.2% (Figure 18B, ii), 13.0% (Figure 18B, iii), and 39.8% (Figure 18B, iv) for the PS-*b*-PMMA case. As a frame-of-reference, the template morphologies of the two polymeric substrates with no adsorbed proteins can be seen in the AFM images provided in Figure 18(C).

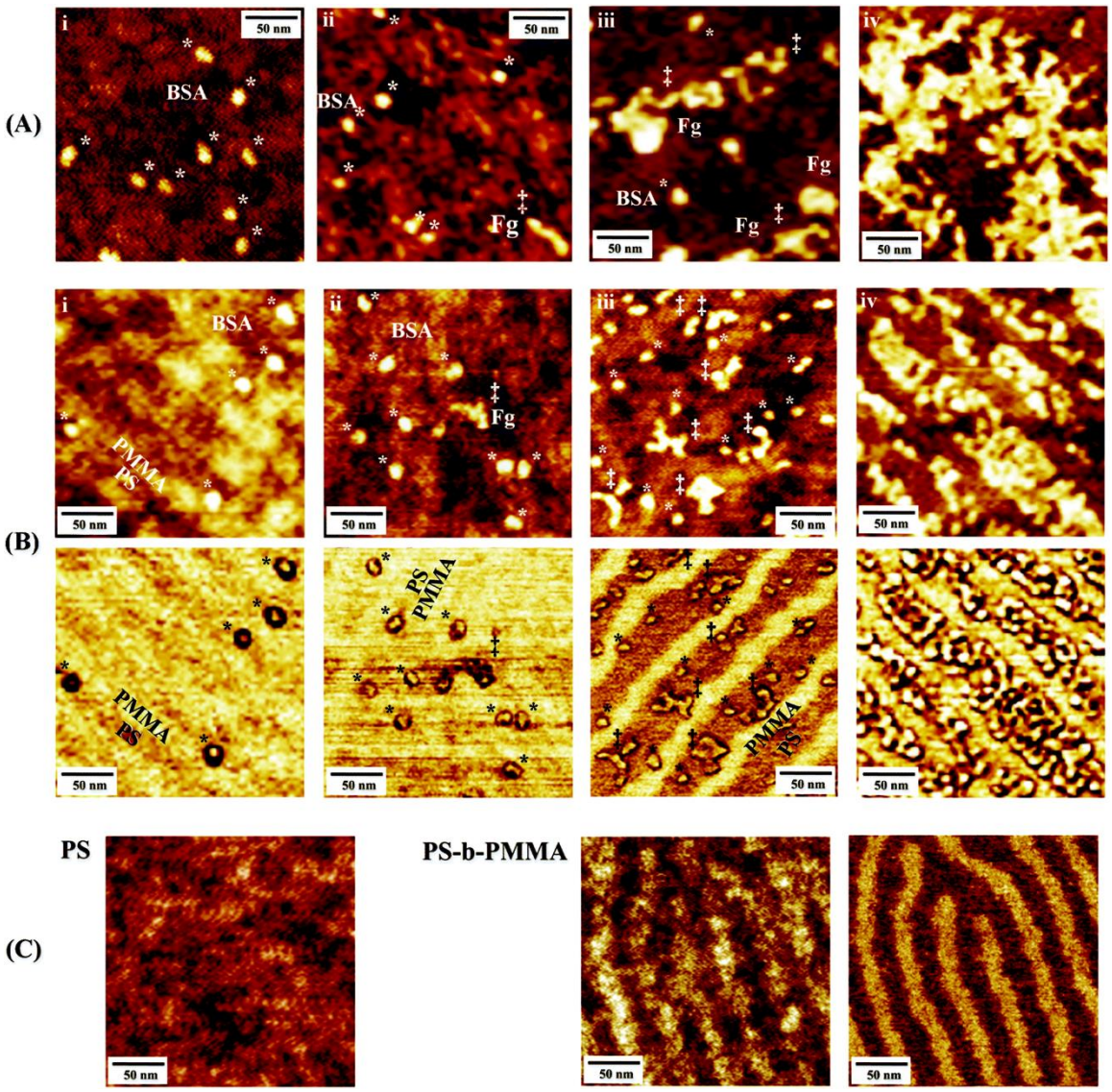

Figure 18. (A) The series of representative atomic force microscopy panels display the step-by-step views of the four key protein adsorption stages examined by using a mixture of bovine serum albumin and fibrinogen exposed on the polystyrene homopolymer surface. The protein mixture containing 1 μg per mL BSA and 0.1 μg per mL Fg was incubated on the PS homopolymer surface for 1 min (i), 5 min (ii), 30 min (iii), and 4 h (iv). (B) The sequence of AFM images illustrates the progressive snapshots of the competitive protein adsorption evaluated on the PS-*b*-PMMA diblock copolymer surface. The PS-*b*-PMMA surface was exposed to the 1 μg per mL BSA and 0.1 μg per mL Fg mixture for 2 h (i), 3 h (ii), 4 h (iii), and 16 h (iv) to allow for competitive protein adsorption. The AFM images in (A) and (B) illustrate the typical behavior of competitive protein adsorption changing from the BSA-dominant phase (i), to the Fg onset phase (ii), to the Fg turnover phase (iii), and to the Fg-dominant phase (iv). As a guide to the eye for distinguishing the two types of proteins, examples of individual BSA and Fg proteins are marked with * and ‡ in the AFM images, respectively. The phase scans corresponding to each topographic panel in (B) are also displayed in the bottom row in order to present the two protein components as well as the two alternating domains of PS and PMMA underneath the proteins. (C) The AFM images of the PS homopolymer (topography panel) and PS-*b*-PMMA diblock copolymer (left for topography and right for phase panels) surfaces without any bound proteins are displayed.

Instead of the adsorption scenario of the initially bound BSA being displaced by Fg over time, an alternative situation of delayed but increased Fg adsorption may also lead to the progressive transition shown in the time-lapse images of Figure 18. In this hypothetical situation, Fg adsorption would occur delayed in time onto the surface partially covered by BSA and, without involving any BSA displacement, Fg molecules would predominantly accumulate with higher affinity than BSA on the available surface sites. I carried out an additional AFM and fluorescence tests to examine this possible scenario. I first determined the change in the average numbers of surface bound BSA and Fg molecules over time *via* direct AFM imaging. For the mixture of 2.5 μg per mL BSA and 0.25 μg per mL Fg deposited for 20 s on a PS homopolymer, the average number of the PS-bound BSA and Fg was found to be 150 ± 8 and 4 ± 2 protein molecules per μm^2, respectively. After prolonged incubation of 90 min, the surface density of the protein changed to 68 ± 5 for BSA and 75 ± 6 for Fg. This observation clearly indicates that BSA is desorbing from the surface over time under the competitive adsorption environment. I additionally examined the degree of surface-bound BSA at different incubation times by replacing the unlabeled BSA with fluorophore-tagged BSA (Figure 19). The resulting fluorescence intensity on the PS-*b*-PMMA surface showed an increased signal over time under a noncompetitive adsorption environment involving only the labeled BSA. On the other hand, a slight decrease in intensity was seen under a competitive adsorption involving both the labeled BSA as well as unlabeled Fg. Corroborating the earlier protein density results, this observation also points to the fact that the initially bound BSA is being replaced over time in a simultaneous multi-component adsorption setting. Hence, my experimental data presented in Figure 18 are progressive snapshots taken from competitive adsorption in which Fg replaces the initially bound BSA with increasing time, rather than depicting the alternative case of delayed Fg adsorption in the environs of permanently bound BSA.

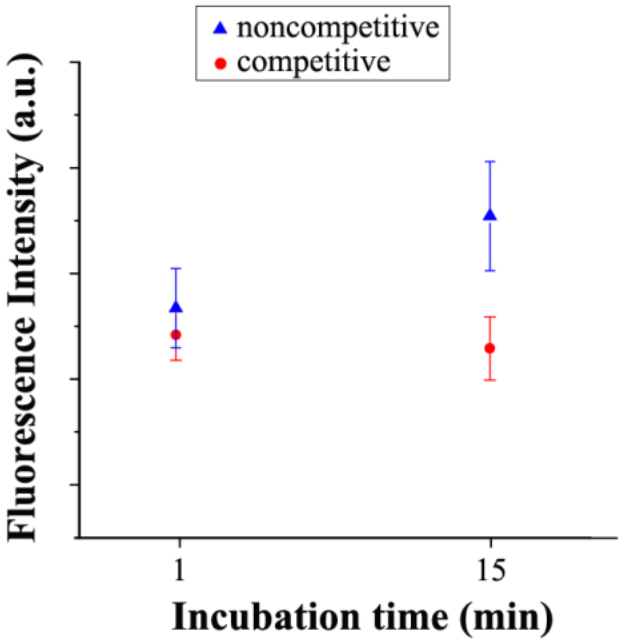

Figure 19. Fluorescence intensity obtained from noncompetitive (blue, 5 g/mL fluorescein isothiocyanate-labeled bovine serum albumin (FITC-BSA)) and competitive (red, 5 g/mL FITC-BSA + 0.5 g/mL Fg) adsorption tests on PS-b-PMMA. For the noncompetitive case, the fluorescence intensity of FITC-BSA increases over time as more BSA molecules accumulate on the surface. On the contrary, the fluorescence of FITC-BSA decreases slightly with time in the competitive adsorption setting due to the displacement of surface-bound BSA by Fg.

The sequential scenarios presented in Figure 18 for both the PS and PS-*b*-PMMA surfaces show that the smaller, more abundant BSA readily adsorbs from the bulk solution onto the polymeric surfaces and, over time, is displaced by the larger, less abundant species of Fg. These outcomes on the PS and PS-*b*-PMMA surfaces confirm that the Vroman effect is indeed seen not only from the chemically uniform surfaces at the macroscopic scale but also from those surfaces whose chemical compositions alternate at the nanoscale. In my time-dependent protein exchange behavior, the protein species of a lower molecular weight (BSA) is displaced by the higher molecular kind (Fg) over time. The initial adsorption of the more abundant, lighter weight BSA proteins is due to the fact that the mass transfer rate of a solute protein molecule is directly related to the solute concentration and inversely proportional to the solute molecular weight. The faster diffusion of the more concentrated, smaller proteins leads to the initial adsorption on the surface. However, larger proteins are considered to be more surface active as they contain more surface binding domains. Proteins with higher molecular weights can be more

flexible in their chain rearrangement and conform to a more energetically favored conformation, which can lead to irreversible adsorption. Therefore, in the Vroman sequence,[3,4,6,8,200–202] the initially adsorbed smaller proteins are expected to be displaced over time by other larger, more strongly interacting proteins. As expected, my results on the macroscopic PS homopolymer surface corroborate the Vroman effect. At the same time, my investigation carried out similarly on the PS-*b*-PMMA block copolymer surface reveals that this Vroman effect is indeed in effect for the nanoscale competitive protein adsorption case as well.

3.3.3 Time-resolved Protein Adsorption on PS and PS-b-PMMA with Varying Concentrations

After carefully examining the different competitive protein adsorption scenarios at different time periods for the macroscopic surface of PS homopolymer (Figure 20) and comparing to that of the nanoscale PS-*b*-PMMA case (Figure 21), I have identified an intriguing effect regarding the time scale associated with the Vroman effect. Figure 20 displays AFM topographic panels which correspond to the typical view frames of the proteins bound on the PS homopolymer surface at the specified times and BSA/Fg concentrations as annotated in each panel. For the relatively high concentration mixture of 5 μg per mL BSA and 0.5 μg per mL Fg, the PS surface contained quite a few Fg molecules already after 5 s in addition to BSA. After 1 min, the homopolymer surface was covered with many Fg and comparatively much fewer BSA molecules than before, with Fg making up more than 90% of the surface-bound proteins. The PS surface was covered then entirely with a dense network of Fg after 5 min. For a lower concentration mixture of 1 μg per mL BSA and 0.1 μg per mL Fg, the transition from BSA to Fg occurred more slowly. For this combination, the PS surface was predominantly decorated with BSA even after 1 min and then transitioned to show some individual and small patches of Fg molecules after 5 min. A network of intertwined Fg started to form after 4 h, but the surface coverage of Fg was still below a monolayer. As expected, the surface coverage of the protein molecules was

lower with the decreased concentration of the binary mixture when examined after the same duration of incubation time. For the adsorption runs from the mixture of even lower concentrations of 0.25 μg per mL BSA and 0.025 μg per mL Fg, the presence of BSA was still persistent on the PS surface even after 30 min which slowly transitioned after 3 h to the stage with both BSA and Fg proteins appearing on the surface. After 16 h, Fg molecules increased in number and tended to assemble close by one another on the PS surface, forming small clusters from several Fg strands. The surface coverage at this concentration was still far from a monolayer even after 16 h.

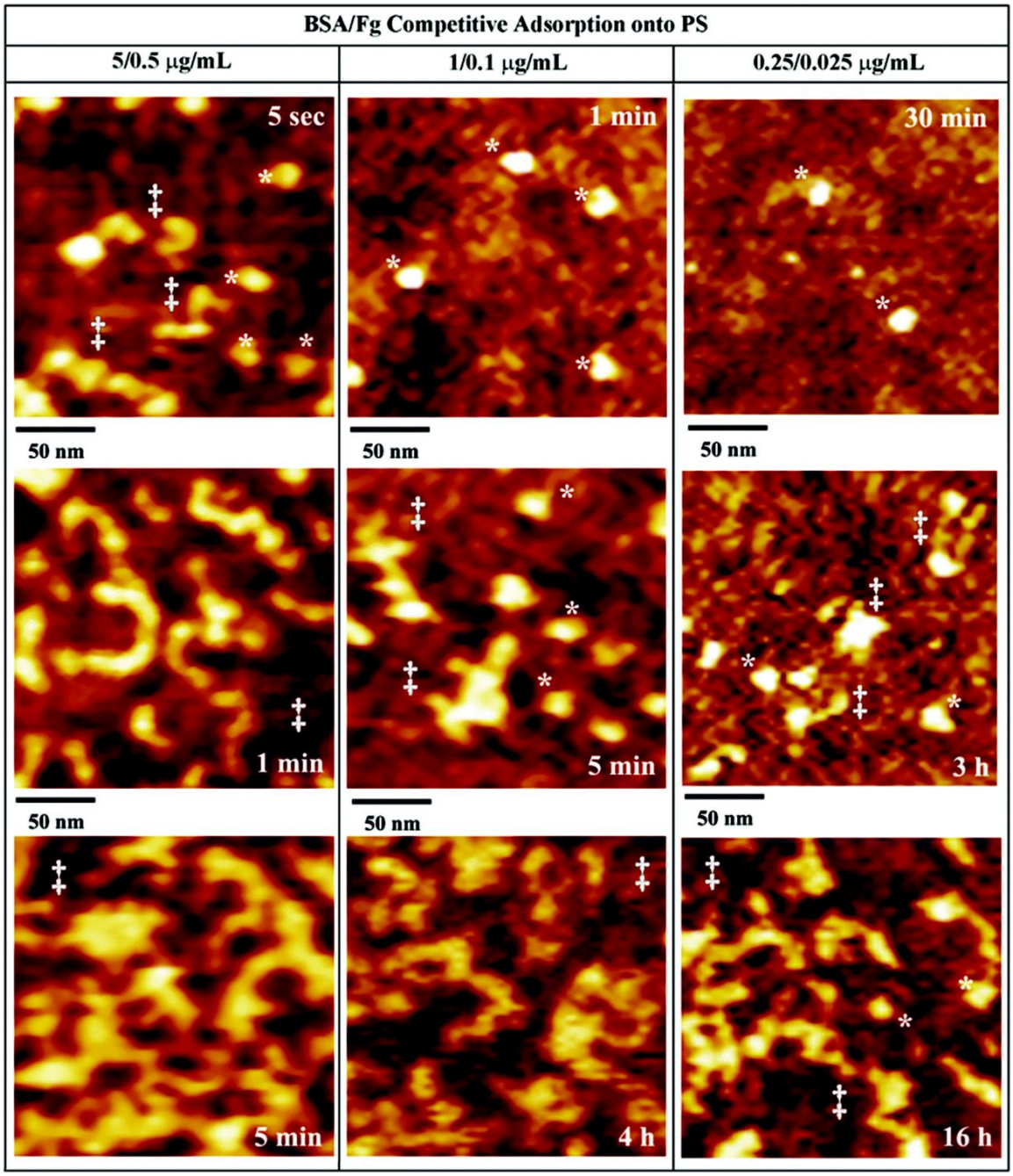

Figure 20. The representative atomic force microscopy frames capture various time-dependent adsorption stages of the binary protein mixture on the polystyrene homopolymer surface. The images show the progression of the initially BSA-dominant phase (top panels) transitioning to the Fg-dominant phase (bottom panels) observed when using different concentrations of the BSA/Fg protein mixture. As a guide to the eye for distinguishing the two types of proteins, examples of individual BSA and Fg proteins are marked with * and ‡ in the AFM images, respectively.

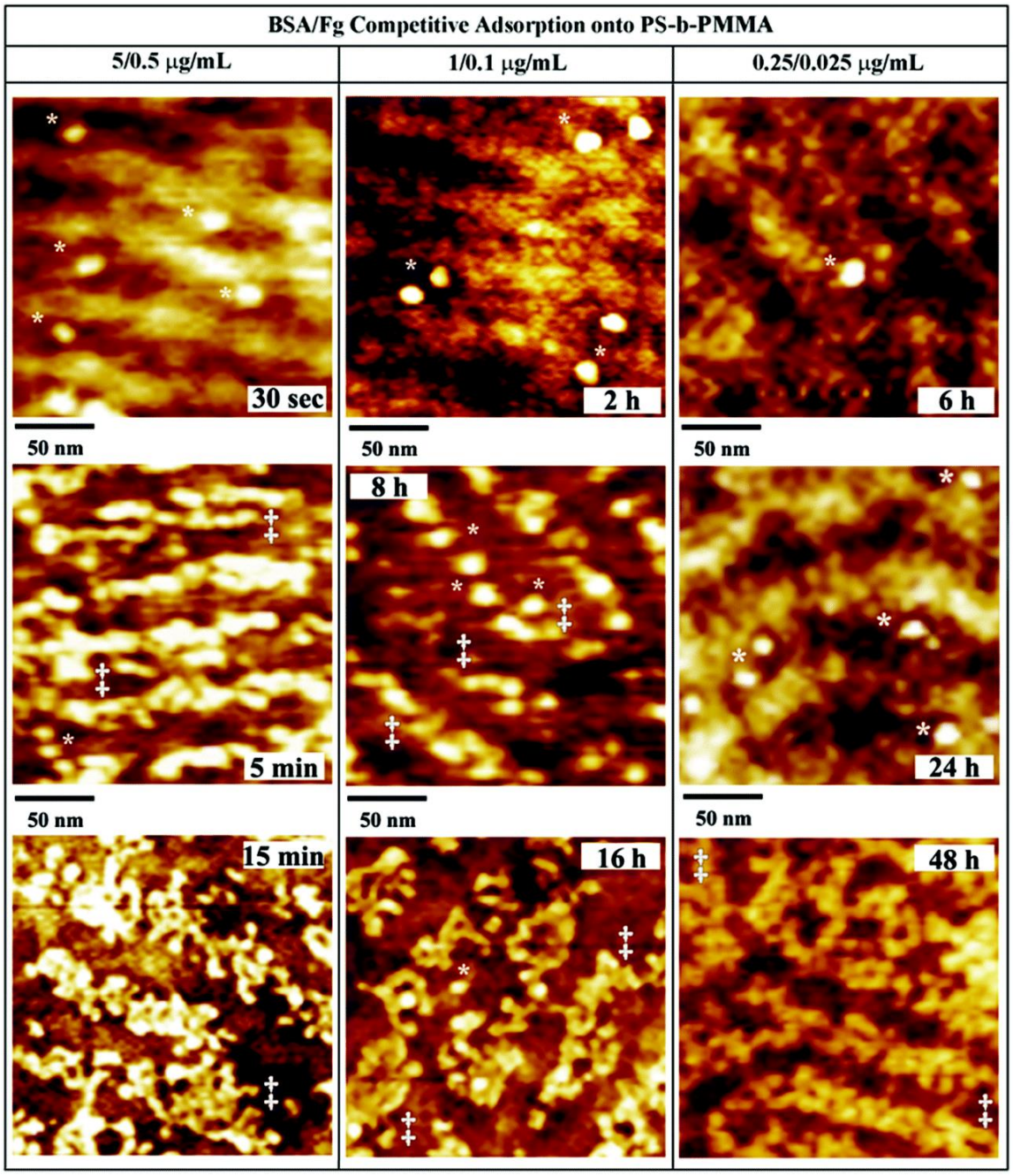

Figure 21. The representative atomic force microscopy frames display various adsorption stages from the competitive bovine serum albumin/fibrinogen adsorption onto the PS-*b*-PMMA surface, profiling the time-lapse views of the initially bovine serum albumin-dominant phase transitioning to the fibrinogen-dominant phase over time at different concentrations of the bovine serum albumin/fibrinogen protein mixture. Examples of individual BSA and Fg proteins are indicated with * and ‡ in the AFM images, respectively.

Similar time-lapse AFM measurements and analyses were subsequently carried out on the nanoscale PS-*b*-PMMA surface for comparison. The resulting data from the same three sets of BSA/Fg

concentrations on the PS-*b*-PMMA surface are shown in the topographic panels in Figure 21. At the BSA/Fg concentration of 5 μg mL^{-1} and 0.5 μg mL^{-1}, the nanoscale surface was still covered largely by BSA after 30 s. The dominantly appearing BSA molecules were found only on the preferred PS domain of the PS-*b*-PMMA due to the greater hydrophobic interaction of the PS domain with BSA. At 5 min, the PS regions were favored by both BSA and Fg, while showing a substantially increased number of Fg molecules and less BSA molecules than before. After 15 min, the PS domains of the PS-*b*-PMMA surface were filled with more Fg molecules, which then became the dominant species on the surface. For the mixture of 1 μg per mL BSA and 0.1 μg per mL Fg, the BSA-dominant phase was still detected even after 2 h, and the surface slowly turned to increase the Fg footprints after 8 h. However, even at 8 h, the surface was still highly rich with BSA. At 16 h, the PS-*b*-PMMA surface reached an adsorption state in which a larger fraction of the proteins on the PS domain was identified as Fg. At the even lower mixture concentration of 0.25 μg per mL BSA and 0.025 μg per mL Fg, the BSA to Fg transition on the surface transpired even later than the earlier two concentration sets. Most of the proteins on the PS-*b*-PMMA surface were BSA at 6 h and 24 h, only increasing the number of BSA proteins found on the surface with longer time. It was only after 48 h that the PS domain on PS-*b*-PMMA was fully covered largely by Fg. Similar to BSA, Fg adsorption exclusively populated the PS domains of the PS-*b*-PMMA under my competitive adsorption setting and the PMMA regions were completely free of any protein adsorption.

The AFM panels shown in Figure 22 are the zoomed-out views of each sample examined by utilizing the different polymeric platforms, protein mixture concentrations, and incubation times specified in the images. When further comparing the points in time associated with the displacement of BSA by Fg occurring on the PS homopolymer *versus* PS-*b*-PMMA diblock copolymer surfaces, a striking difference was noted from the comparative time-lapse images tracking the two proteins on the

two polymeric surfaces in Figure 22. In contrast to the competitive adsorption timeline evaluated on the PS surface, my experimental results on the PS-*b*-PMMA indicate that the time to reach the BSA to Fg turnover state is significantly increased on the PS-*b*-PMMA surface. This increase in nanointerface-engaged residence time of the initially bound BSA was monitored in all concentration cases of the BSA/Fg mixture when evaluating the competitive protein adsorption scenarios occurring on the PS-*b*-PMMA platform relative to those on the PS.

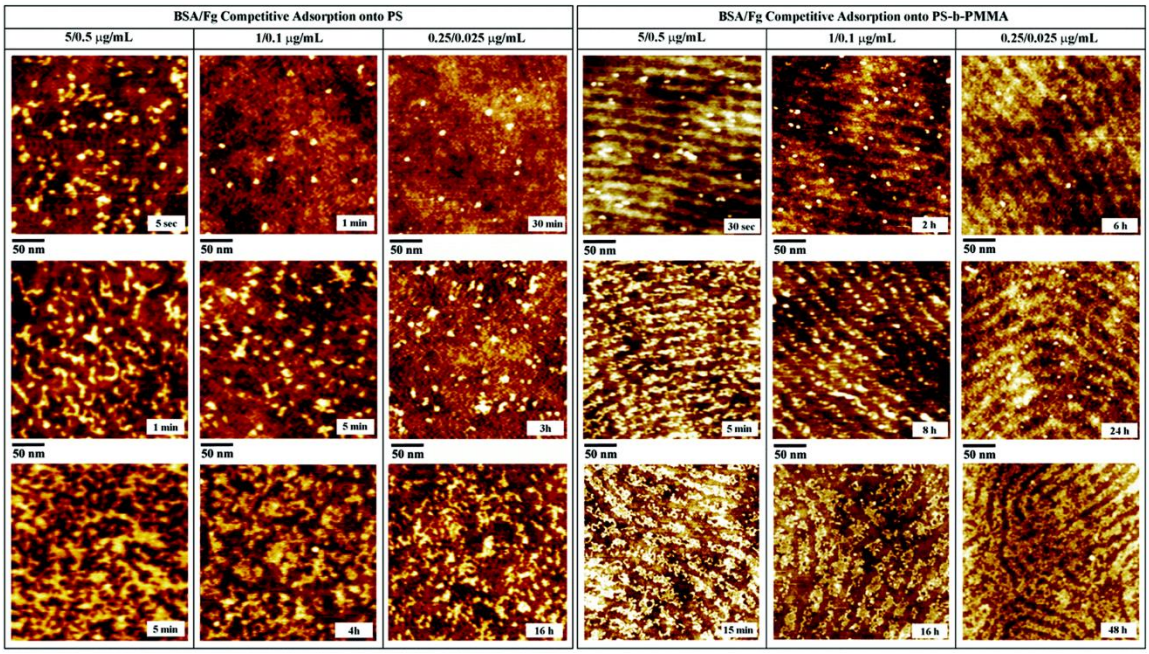

Figure 22. Typical atomic force microscopy panels of 500 nm × 500 nm in scan size are displayed in order to show larger views of the representative bovine serum albumin and fibrinogen adsorption behavior corresponding to each polymeric platform, protein mixture concentration, and incubation time specified in the images. Under all scenarios of my competitive protein adsorption experiments, the Fg-rich surface phase occurs after significantly delayed time on the PS-*b*-PMMA relative to the PS case.

I also assessed Fg adsorption on the two polymeric templates separately under a non-competitive adsorption setting (Figure 23). I found that Fg adsorption is more favored on the PS-*b*-PMMA with the PS: PMMA nanointerfaces relative to the chemically uniform PS surface examined under an identical biodeposition condition. Similar observations of preferred protein binding on diblock copolymer relative to homopolymer surfaces were reported on surfaces with nanoscopic[45,84,203] and macroscopic[204] chemical interfaces. This phenomenon may be explained by the inherent chemical

nature of a protein surface where various amino acid residues on the protein exterior are known to exhibit varying degrees of hydrophobicity/philicity and electrostatic charges. Relative to the chemically uniform PS surface, the PS: PMMA interfacial areas of the diblock copolymer can serve as more favorable and stable binding sites towards a greater fraction of amino acids on the protein exterior. Hence, the slower BSA to Fg turnover time observed on the PS-*b*-PMMA surface in my competitive adsorption study is likely due to the increased BSA residence time on the PS-*b*-PMMA surface presenting the nanointerfaces, rather than by a potentially reduced affinity in Fg adsorption on the diblock copolymer relative to the homopolymer surface.

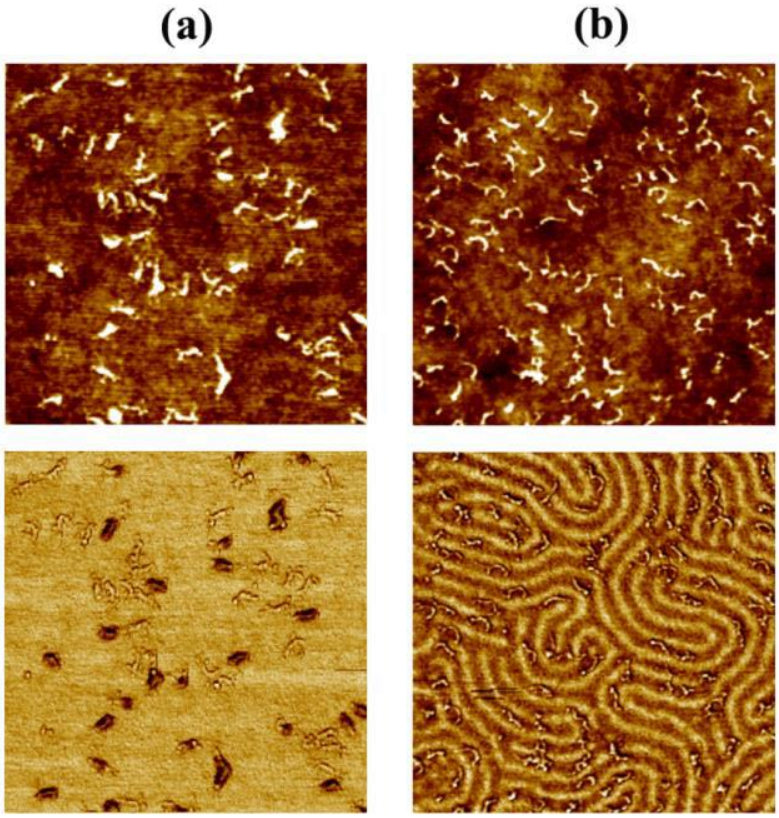

Figure 23. Atomic force microscopy topography (top) and phase (bottom) panels of 50 g/ml fibrinogen deposited under an identical non-competitive deposition condition onto a (a) Polystyrene homopolymer and (b) PS-b-PMMA diblock copolymer surface. All images are 800 x 800 nm^2 in scan size. The surface density of bound Fg molecules is approximately two-fold higher on the PS-b-PMMA relative to that on the PS, indicating a greater Fg adsorption affinity to the diblock surface presenting PS: PMMA nanointerfaces relative to the chemically uniform PS.

3.3.4 Time Associated with Bovine Serum Albumin to Fibrinogen Transition on Polystyrene Versus PS-b-PMMA

The unique phenomena observed on the nanoscale diblock copolymer surface relative to the macroscale homopolymer were further ascertained by charting the surface-bound protein composition over time. The resulting time-dependent exchange profiles of surface-bound proteins on the control and test surfaces are presented in Figure 24. Although only the limited numbers of the representative AFM panels are shown in Figure 20 through 22, extensive and systematic AFM measurements were additionally carried out on both the PS and PS-*b*-PMMA surfaces at a substantial number of sampling points under varying adsorption conditions. The concentrations of the BSA/Fg protein mixture tested in my extended competitive adsorption study at the nanoscale were 5/0.5, 2.5/0.25, 1/0.1, 0.5/0.05, and 0.25/0.025 μg mL^{-1} for PS-*b*-PMMA. To compare the results with those on a macroscale surface, the BSA/Fg concentrations of 5/0.5, 1/0.1, and 0.25/0.025 μg mL^{-1} were selected for PS. The incubation time of the protein mixture was varied spanning from 5 s to 48 h with over 20 different time points used for my time-lapse AFM investigations.

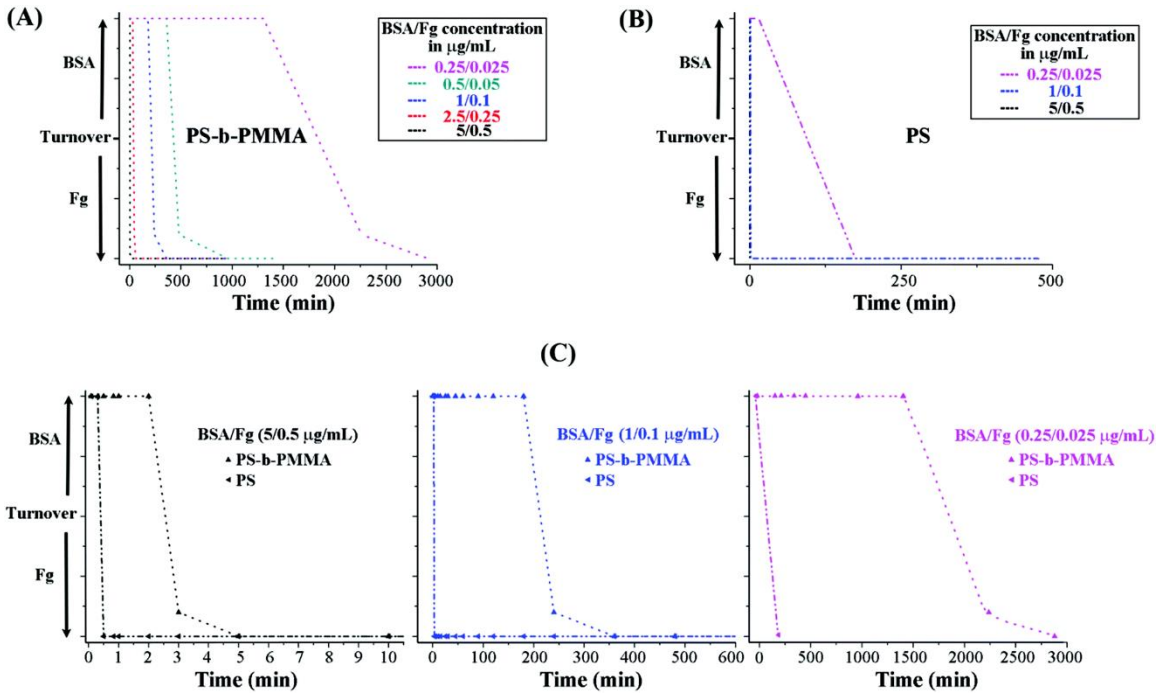

Figure 24. (A) The dominant occurrence profiles of the bovine serum albumin and fibrinogen proteins adsorbed on the PS-*b*-PMMA block copolymer surfaces are charted as a function of time at various protein concentrations as indicated in the legend. (B) Protein occurrence profiles found on the PS homopolymer surfaces are plotted as a function of time at three different concentrations shown by using the same color-coded plots as (A). (C) The three sets of graphs directly compare the time-dependent frequency profiles of the surface-bound protein types found on the PS-*b*-PMMA diblock and PS homopolymer surfaces for given concentrations. The early time data are shown for easy comparison of the competitive adsorption behaviors on the two different polymeric templates.

The plots shown in Figure 24(A) were taken from the competitive adsorption data on the PS-*b*-PMMA surface by using the five different BSA/Fg mixture concentrations as annotated. As a comparison, the plots shown in Figure 24(B) are those on PS. The three graphs in Figure 24(C) illustrate the differences in time spanning the BSA to Fg transition observed from the PS-*b*-PMMA (chemically alternating at the nanoscale) *versus* the PS (chemical uniformity persistent at the macroscale) polymers at different protein concentrations, while clearly illustrating the earlier time data. Upon evaluating the large set of concentration- and time-dependent AFM images on both polymeric surfaces, the turnover from BSA to Fg on the PS homopolymer surface was determined to occur even before 5 s for the BSA/Fg concentration of 5/0.5 μg mL^{-1}, between 1–5 min for 1/0.1 μg mL^{-1}, and between 30–180 min for 0.25/0.025 μg mL^{-1}. On the nanoscale PS-*b*-PMMA surface, on the other hand, the turnover from

BSA to Fg took place between 2–3 min for the BSA/Fg concentration of 5/0.5 μg mL^{-1}, 30–45 min for 2.5/0.25 μg mL^{-1}, 3–4 h for 1/0.1 μg mL^{-1}, 6–8 h for 0.5/0.05 μg mL^{-1}, and 24–36 h for 0.25/0.025 μg mL^{-1}. The time to reach a Fg-dominant phase with only Fg covering all exposed PS domains of PS-*b*-PMMA was determined as 15 min, 1 h, 16 h, 24 h, and 48 h for the five sets of BSA/Fg concentrations, respectively.

The timescale associated with the displacement of the initially adsorbed BSA molecules was determined to be much larger on the nanoscale domains of the PS-*b*-PMMA diblock copolymer relative to the PS homopolymer, which implies a significant slowdown of the onset of the Vroman effect in nanoscale competitive adsorption. This effect, confirmed with the extended set of data shown in Figure 24, is also substantiated in the colored bar graphs shown in Figure 25(A). The bar graph displays the transitioning stages of the protein type found on the PS-*b*-PMMA and the PS templates as a function of time. The early time data are clearly seen in the graphs of Figure 25(B) and can be straightforwardly used to compare between the macroscopic and nanoscale adsorption cases at the three denoted concentrations. The BSA-dominant, BSA/Fg turnover, and Fg-dominant phases are marked in blue, gradient purple, and orange, respectively. The time associated with the transition from BSA to Fg can be revealed by simply identifying the location of the gradient purple block along the vertical axis in these bar graphs. The dependence of protein concentration on the BSA to Fg turnover time is also plotted in Figure 25(C). The turnover time is inversely proportional to the protein mixture concentration on both the PS-*b*-PMMA diblock and PS homopolymer surfaces.

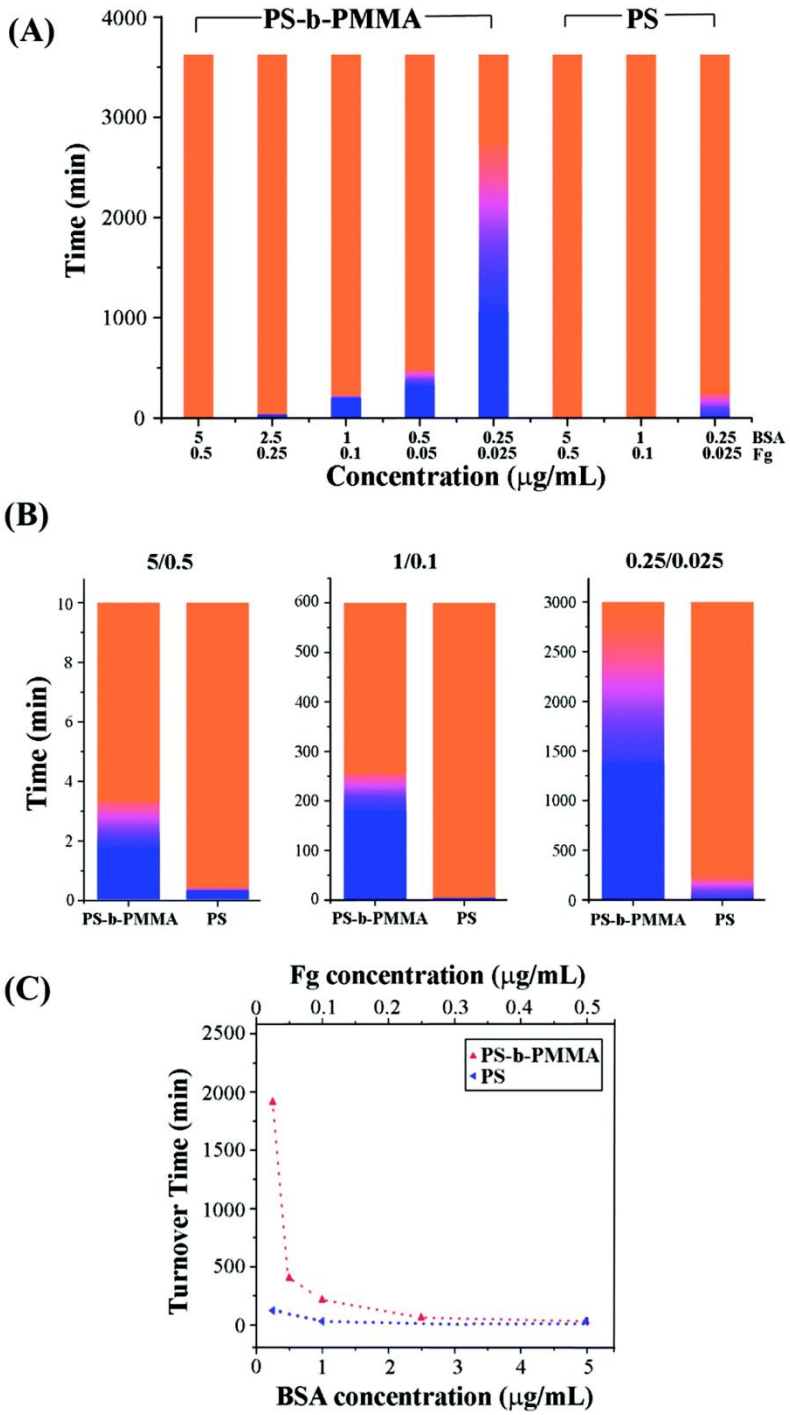

Figure 25. (A) The colored bar graphs display the transitioning stages of the protein type found on the PS-*b*-PMMA and the polystyrene templates as a function of time. BSA-dominant phase, the Fg onset/turnover phases, and the Fg-dominant phase are identified in blue, gradient purple, and orange, respectively. (B) The early stage behaviors of the BSA to Fg transition are captured clearly to display the apparent difference in time marking the Fg turnover phase between the two polymeric templates at the specified protein concentrations. (C) The times corresponding to the average turnover point from BSA to Fg are plotted as a function of the protein concentration. The red and blue data points are taken from the PS-*b*-PMMA diblock and the PS homopolymer surfaces, respectively.

3.3.5 Understanding the Prolonged Residence Time and The Role of Nanointerfaces

The large displacement inertia of the originally adsorbed proteins on the PS-*b*-PMMA relative to the PS surface indicates that the initially bound BSA proteins are more stable on nanosized surfaces, resisting their desorption into the bulk solution over time. This increased stability of the already surface-bound protein molecules and, hence, the prolonged residence time on the nanoscale template may be explained by the more energetically favored surface adsorption environment facilitated by the high density of the PS: PMMA interfaces provided by the repeating blocks of PS and PMMA. Proteins which are highly amphiphilic in surface chemical compositions and properties are known to prefer the surface regions with chemical interfaces, and this effect is best realized when the size scale of the chemical interfaces is commensurate with the size of the individual proteins themselves, *i.e.* tens of nanometers.[81,82] This interface-preferring adsorption of proteins was previously reported by us and others.[81,82,114,147,204,205] Proteins in those studies selectively are reported to adsorb on the preferred polymeric domain, *e.g.* immunoglobulin G (IgG) found only on the PS regions of the PS-*b*-PMMA and PS/PMMA blend. It has been shown that the protein molecules such as SA, IgG, and fibronectin (Fn) predominantly favor the PS areas closer to the PS:PMMA interface, when their binding affinity within the favored PS domain was further examined with respect to the distance from the interface.[81]In these cases, the PS regions away from the interfaces were left largely unoccupied when the surface coverage of the proteins is low and these initially unoccupied PS areas away from the interfaces become populated by the proteins when loading more proteins to the surface.[81,147,156]

The presence of the densely repeated PS: PMMA chemical interfaces in the PS-*b*-PMMA support may promote more stable and stronger adhesion of the protein to the underlying surface by satisfying the surface interaction needs of assorted amino acid residues with varying hydrophobicity/philicity present on the exterior part of the protein molecule. When such needs are met,

it will be harder to desorb and displace the protein molecules once they are surface-bound, effectively making the protein inert to other competing desorption or displacement events and leading to the extended residence time of the initially bound proteins. On the other hand, the attachment strength between the same protein molecule to the chemically uniform PS homopolymer will be weaker since the chemically homogeneous environment will limit its favored interactions with relatively smaller number of amino acids and restrict protein conformations on the surface. Therefore, proteins on the PS platform will be more susceptible to desorption incidents into the bulk solution, providing ample opportunities for other proteins to adsorb in its place.

The presence and absence of the chemical interfaces in the PS-*b*-PMMA *versus* PS templates, respectively, may also result in two different adsorption scenarios from the electrostatic interaction point of view. On the PS surface, the faster and more abundant BSA molecules will arrive at the surface to a saturation coverage. Further surface adhesion of BSA will be deterred due to the strong repulsion between the adjacent BSA molecules that are negatively charged at pH 7.4. This condition may induce faster BSA desorption events followed by the replacement *via* Fg whose equilibrium binding constant is six- to seven-fold higher than that of BSA on a hydrophobic surface.[19] On the other hand, such repulsive interactions among BSA molecules may be reduced on the PS-*b*-PMMA surface since the preferred adsorption domains of PS hosting surface bound BSA molecules are physically separated by the neighboring PMMA domains devoid of any proteins. This environment may yield a longer retention time of the initially bound BSA molecules on the PS-*b*-PMMA. Further work is underway to ascertain dominant mechanistic pathways associated with the large increase in the nanointerface-engaged residence time of the initially bound proteins.

Although it is known that factors such as increased surface roughness and higher surface area to volume can affect protein adsorption, earlier protein adsorption studies have reported varying

outcomes from employing roughened platforms and increased surface areas. For example, the adsorption of SA and Fn on a bioceramic material with an average surface roughness of 32 nm was higher than that with a 142 nm roughness.[29] On the other hand, another study reported that the nanometer-scale roughness variation ranging from 5 to 60 nm did not result in any changes in the adsorbed amount and the structural stability of lysozyme.[31] I note that the phenomenon observed in this study pertains to the PS-*b*-PMMA surface with an average roughness of 0.32 nm which does not differ greatly from the roughness value of 0.23 nm from the PS surface.[84] When comparing the difference in the substrate roughness to the size of the individual proteins, my polymeric surfaces can be considered to be very smooth adsorption platforms. In addition, both BSA and Fg exhibit a higher binding preference to the PS regions of the PS-*b*-PMMA. When compared to the PS homopolymer surface with 100% of the exposed surface area being PS, the diblock copolymer presents only about 50% of the exposed surface in the chemical form of PS and consequently offers a much less effective surface area for protein binding. Yet, my competitive adsorption study shows that the binding of the initially bound proteins is much stronger on the PS-*b*-PMMA surface than that on PS. From these reasons, the effect found in my experiments is believed to have originated from the chemical interfaces repeatedly presented on the nanoscale PS-*b*-PMMA surface, not from the factors associated with increased surface roughness or specific surface area. Hence, the physical-chemical uniqueness of the PS-*b*-PMMA diblock copolymer surface, simultaneously providing chemical heterogeneity and reduced dimensionality, is imperative in inducing the prolonged residence time of the initially bound proteins in competitive protein adsorption.

From the fundamental research standpoint, my experimental findings provide deeper insight into competitive protein adsorption behavior that can encompass nanoscale size regimes. I ascertain the similarities and dissimilarities in the time-dependent protein adhesion characteristics that manifest on

macroscopic *versus* nanoscopic polymeric supports. From the biotechnological viewpoint, my work reveals that the use of nanomaterials in biomaterial and biosensor applications, specifically the employment of solid surfaces providing chemical interfaces in the size range of several tens of nanometers, can result in reduced dimensionality- and chemical interface-driven, surface-bound proteins' resistance to desorption by other competing protein molecules in bulk solution. This phenomenon can be utilized in creating protein-stabilizing supports for implant materials and in tissue engineering, as well as further be exploited to produce antifouling biomedical detection and delivery devices resistant to nonspecific adsorption of undesired proteins.

3.4 Summary

In summary, the competitive adsorption characteristics of the model binary protein mixture containing BSA and Fg have been examined on the PS homopolymer and the PS-*b*-PMMA diblock copolymer by clearly resolving the nanoscale topological details of the individual proteins as well as those of the underlying polymeric templates. The well-known protein exchange process over time was observed from both the macroscopic and nanoscopic polymeric surfaces, in which the initially bound BSA molecules on both the homopolymer and diblock copolymer surfaces were later replaced by Fg. The key stages of the overall turnover processes from the BSA- to Fg-covered phases were identified at various protein concentrations and incubation times by acquiring extensive time-lapse images at the individual protein level from a large set of protein-bound surfaces. The time-dependent protein displacement events on the chemically uniform and alternating polymeric surfaces in the absence and presence of nanoscale chemical interfaces, respectively, were then systematically compared. In contrast to the macroscopic, chemically uniform PS surface, a unique phenomenon was identified on the nanoscale PS-*b*-PMMA surface pertaining to a large increase in the nanointerface-engaged residence time of the initially bound BSA. The pronounced retardation to the onset of the protein displacement

process and the inertia of the originally bound protein in the presence of other competing protein molecules in the bulk solution were explained by the existence of the periodic PS and PMMA chemical interfaces on the size scale equivalent to the individual proteins. The nanospaced chemical interfaces provide more stable and stronger attachment sites for both hydrophobic and hydrophilic binding moieties on the exterior of the protein, rendering the once-adsorbed protein more inert to the competing events of desorption and displacement on the nanoscale template. The insights gained from this study on competitive protein adsorption on nanoscale surfaces, particularly the significant slowdown of the time-dependent protein exchange process commonly known as Vroman effect, will be valuable in developing biomaterials, biosensors, and biomedical devices with reduced dimensionality functioning in highly miniaturized formats.

4 Revealing the Principal Attributes of Protein Adsorption on Block Copolymer Surfaces with Direct Experimental Evidence at The Single Protein Level

4.1 Introduction

In this chapter, I ascertain competitive protein adsorption behaviors that occur sequentially onto the nanoscale BCP surface of polystyrene-block-polymethylmethacrylate (PS-b-PMMA) by using IgG and Fg as model protein components. The same sets of individual IgG and Fg as well as PS-b-PMMA nanodomains are faithfully tracked and unambiguously resolved at the individual protein level by acquiring a time-lapse series of high-resolution AFM frames from the same surface locations. I record the adsorption/desorption/displacement events of each protein on PS-b-PMMA. I also provide experimental proof for protein behaviors such as post-adsorption protein rearrangement, lateral mobility on surface, tendency for cooperative/noncooperative assembly, occurrence frequency for different adsorption pathways, and directionality in protein exchange. In addition, I elucidate preadsorbed surface-associated behaviors in which the subsequent stage protein adsorption is influenced by the amounts of prebound proteins on the surface, rather than the bulk concentration of the newly adsorbing proteins. By means of Monte-Carlo (MC) simulations of a simple model, I further corroborate with the experimental outcomes of preadsorbed surface-dependence and rationalize main adsorption events in terms of the model parameters. My findings in this study will be important for building the much-needed knowledge base on competitive protein adsorption. By providing definitive experimental evidence on sequential protein adsorption onto nanoscale surfaces, my results may also open up better

mechanistic understanding of protein adsorption processes to aid in the development of new BCP-based biomaterials and biosensors.

4.2 Results and Discussion

4.2.1 Structure of Model Proteins

IgG is made up of four polypeptide chains, comprising two identical light chains (L chains, 25 kDa each) as well as two identical heavy chains (H chains, 50 kDa each), forming a Y-shaped structure with a molecular weight of 150 kDa.[206,207] The dimensions of IgG are estimated to be 14.5 nm by 8.5 nm by 4.0 nm based on X-ray crystallographic data.[206] Compared to IgG, Fg is highly elongated in its shape, exhibiting a length-to-width anisotropy of ~10:1.[84] The 340 kDa dimeric protein of Fg is composed of three interwoven polypeptide chains of Aα, Bβ and γ that are linked by coiled-coil connectors. The structure of Fg contains rod-like chains spanning two distal domains of D and one centrally located domain of E. Fg was first imaged by electron microscopy (EM), revealing its molecular length of ~47 nm with roughly spherical D and E domains.[128] Later, more intricate Fg structures were revealed based on crystallographic, EM, and AFM data, which additionally show split D domains and αC chains stemming from each D domain.[129,130,192]

These two proteins were chosen as the model systems due to their importance in basic biology research/biomedical applications, the large difference in their shape anisotropy, and the pre-existing bulk adsorption data. IgG and Fg are abundant proteins in blood and, hence, materials coated with these proteins play a central role in the fields of biosensors and implants.[6,7,202,208] Therefore, extensive literature on the bulk and macroscopic scale adsorption of IgG and Fg onto different solid surfaces exist in biomaterials, thrombosis, and hemotology.[5,7,8,77,101,127,208–212] Surface-adsorbed IgG and Fg molecules are also frequently employed in basic research and

biotechnology in the form of protein arrays, solid-state biosensors, and protein patches.[212–215] In addition, the large shape difference between the globular IgG and the elongated Fg renders straightforward identification of the two proteins using AFM. For IgG bound on PS-b-PMMA, the overall shape can be viewed as sphere-like with its dimensions approximated by AFM as 15 nm in diameter and 2.5 nm in height.[147] For Fg on PS-b-PMMA examined by AFM, the overall length of the boomerang-shaped protein can be approximated as 45 nm (spanning the D-E-D domains with folded αC) with an average spherical domain height of 2.2 nm.[84]

4.2.2 Atomic Force Microscopy Tracking of Individual Proteins

Using these model proteins, I examined characteristic adsorption behaviors upon sequential introduction of the protein species to the BCP surface. All data reported in this study correspond to sequential protein adsorption behaviors at very low surface coverage regimes, below a monolayer-forming condition. AFM imaging was carried out repeatedly on the same PS-b-PMMA surface locations between each protein deposition stage. Any changes on the surface were faithfully recorded to reveal those from the same sets of proteins before and after sequential treatments. Specific activities that the individual proteins underwent such as adsorption, desorption, and replacement were then identified. The schematic illustrated in Figure 26(A) depicts the overall AFM tracking process of the same PS-b-PMMA area exposed to different protein species or neat buffer in a multistep process of solution deposition. The underlying PS-b-PMMA template used in this study exhibits fingerprint-like patterns of 45 nm in repeat spacing.[147] The fingerprint patterns expose alternating PS and PMMA nanodomains. In all AFM data presented in this study, the PS and PMMA nanodomains appear as darker (orange) and lighter (yellow) regions, respectively. The nanodomain patterns on the BCP surface serve as convenient markers to return to the same areas for protein tracking. AFM panels shown in Figure 26(B) and

(C) are representative series of topographic and phase scans captured before and after Fg introduction to a PS-b-PMMA surface pretreated with IgG. The paired AFM images in Figure 26(B) and (C) were acquired from the same PS-b-PMMA location before and after the Fg treatment. It can be seen clearly from the zoomed-in phase panels in Figure 26(C) that the PS-b-PMMA surface changed from initially containing only short, round particles of IgG (left frames) to displaying more of long, boomerang-shaped Fg molecules (right frames). The AFM tracking of individual proteins enabled me to directly visualize specific sequential adsorption events that each protein undergoes, whose conclusive evidence was not experimentally available before. Furthermore, this approach allowed determination of predominant adsorption trends and pathways in sequential protein adsorption based on direct observations of individual protein behaviors. Those characteristics are detailed herein.

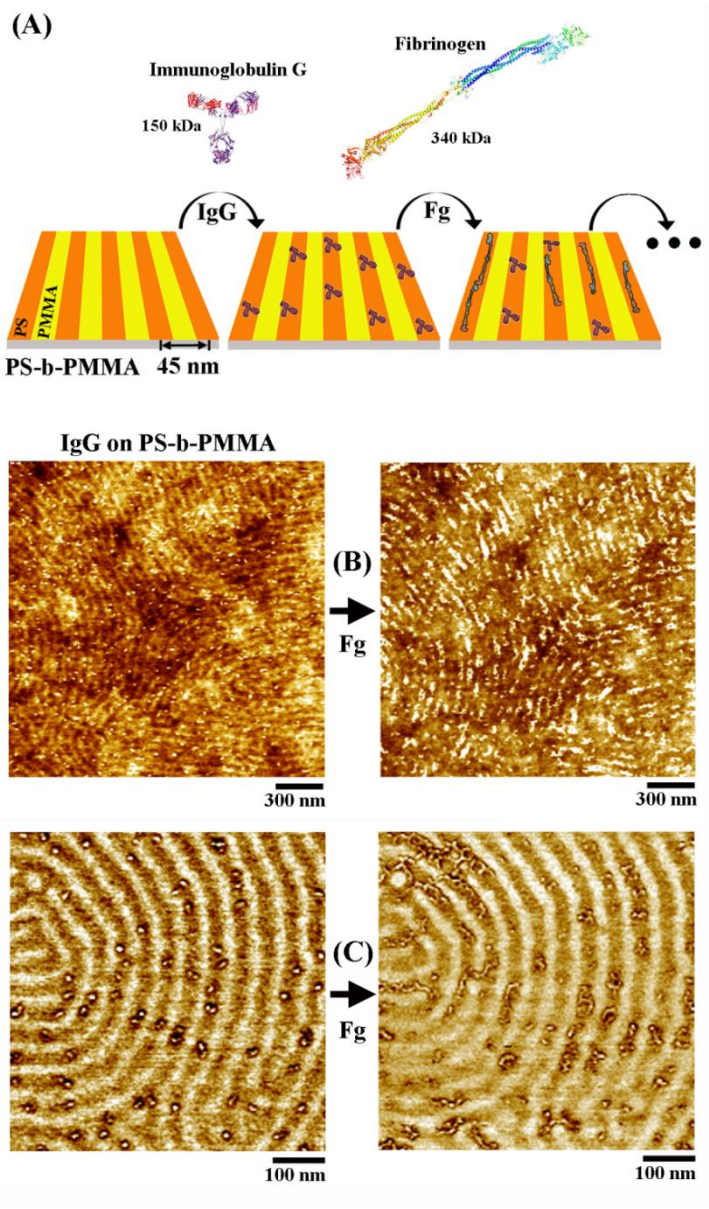

Figure 26. (A) Schematic illustrations displaying the sequential protein adsorption experiments on PS-b-PMMA. AFM imaging was carried out on the same BCP nanodomain regions after each treatment step involving either a protein or neat buffer solution. Individual proteins from the same surface areas were tracked to study consecutively occurring events such as protein adsorption, desorption, and replacement. (B-C) A representative series of AFM panels showing my typical AFM tracking data obtained from the same surface sites. The panels in (B) and (C) correspond to the BCP surface after introduction of an IgG solution to a clean PS-b-PMMA template (left column) and the same PS-b-PMMA location after exposure to a Fg solution (right column). AFM images in (B) are topographic panels and those in (C) are phase images.

4.2.3 Two-Stage Tracking of Individual Proteins

Sequential adsorption events on PS-b-PMMA were further scrutinized and analyzed to determine the exact changes associated with individual proteins. AFM data in Figure 27(A) display typical

phase frames of initial IgG deposition followed by a second deposition step of Fg. Examples of tracking distinct adsorption events associated with discrete IgG molecules are provided in the high-magnification panels of Figure 27(B) and (C). Specifically, Figure 27(B) follows the different activities of the four IgG molecules adsorbed initially on a PS-b-PMMA surface. The ensuing Fg deposition led to the replacement of two IgG molecules with three newly bound Fg molecules. Another example in Figure 27(C) shows a different scenario, in which the two initially adsorbed IgG molecules remained on the surface upon Fg introduction and two new Fg molecules appeared by taking up surface sites unoccupied by IgG.

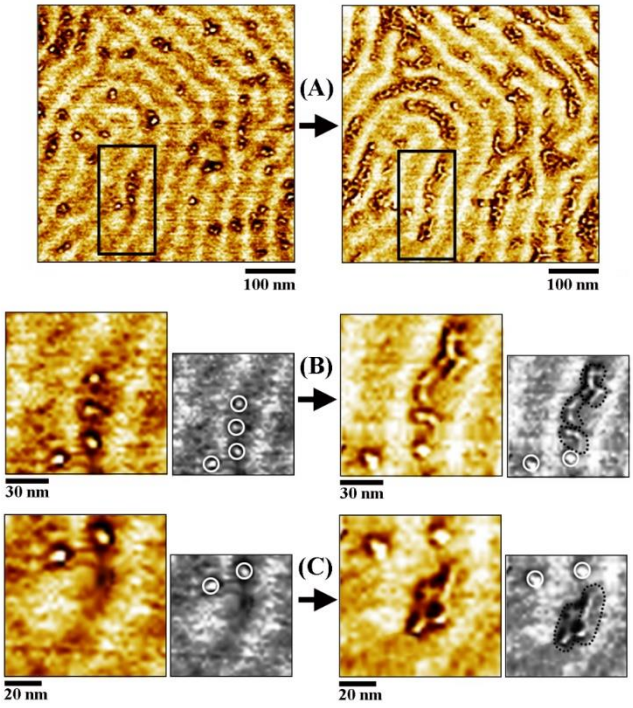

Figure 27. Atomic force microscopy phase images of representative data sets tracking individual proteins between different deposition steps for determination of distinct adsorption events associated with each protein. (A) AFM panels acquired from an identical PS-b-PMMA location are shown side by side for direct comparison of the dynamic events occurring on the same polymeric surface area after the introduction of an IgG solution (left) and subsequent exposure to a Fg solution (right). (B and C) Different examples of serial protein adsorption events are displayed in the higher magnification AFM panels, revealing the distinctive activities of the individual IgG molecules found inside the inserted box in (A). For clarity, each colored AFM phase scan is also shown in grey scale image. In (B), the sequential adsorption event led to the displacement of two IgG molecules originally adsorbed on the surface by three Fg molecules. In (C), the two initially adsorbed IgG molecules remained on the PS-b-PMMA surface, whereas the two new Fg molecules took up empty surface sites void of IgG.

4.2.4 Five Common Competitive Adsorption Events

Furthermore, I carefully evaluated a large set of AFM images (over 100 of 2x2 μm^2 frames) obtained from the same PS-b-PMMA areas before and after the two-stage deposition process of IgG followed by Fg. Each kind of adsorption event that the proteins engaged in was catalogued to classify main types of sequential adsorption pathways. Five different pathways were identified and summarized in Figure 28, where Figure 28(A) shows AFM data that present all five of the predominant adsorption pathways, and Figure 28(B) shows their schematic illustrations. The sequential adsorption process can result in cases where the initially bound protein species are left persistently adsorbed on the BCP surface even after the introduction of a 2^{nd} protein species (i, persistent adsorption). The process can also lead to desorption of initially adsorbed protein species, generating empty surface sites (ii, desorption with new empty sites). Alternatively, the process can lead to the replacement of initially adsorbed protein species by the 2^{nd} stage protein molecules (iii, replacement/exchange). In addition, the sequential adsorption process can trigger the 2^{nd} stage species to adsorb in close proximity to the initially bound proteins (iv, cooperative adsorption). Finally, the process can produce adsorption of the 2^{nd} protein species on empty surface sites away from the initially bound proteins (v, noncooperative adsorption). The analysis criteria I used to differentiate the two cases of (iv) cooperative versus (v) noncooperative adsorption was the diameter of the 1^{st} stage protein. Hence, in the aforementioned IgG → Fg adsorption, the binding event was considered as cooperative if Fg appeared within 15 nm of surface-bound IgG in any direction. In Figure 28(A), the different examples of these sequential adsorption pathways are marked as (i) through (v), next to each protein that underwent the specified process.

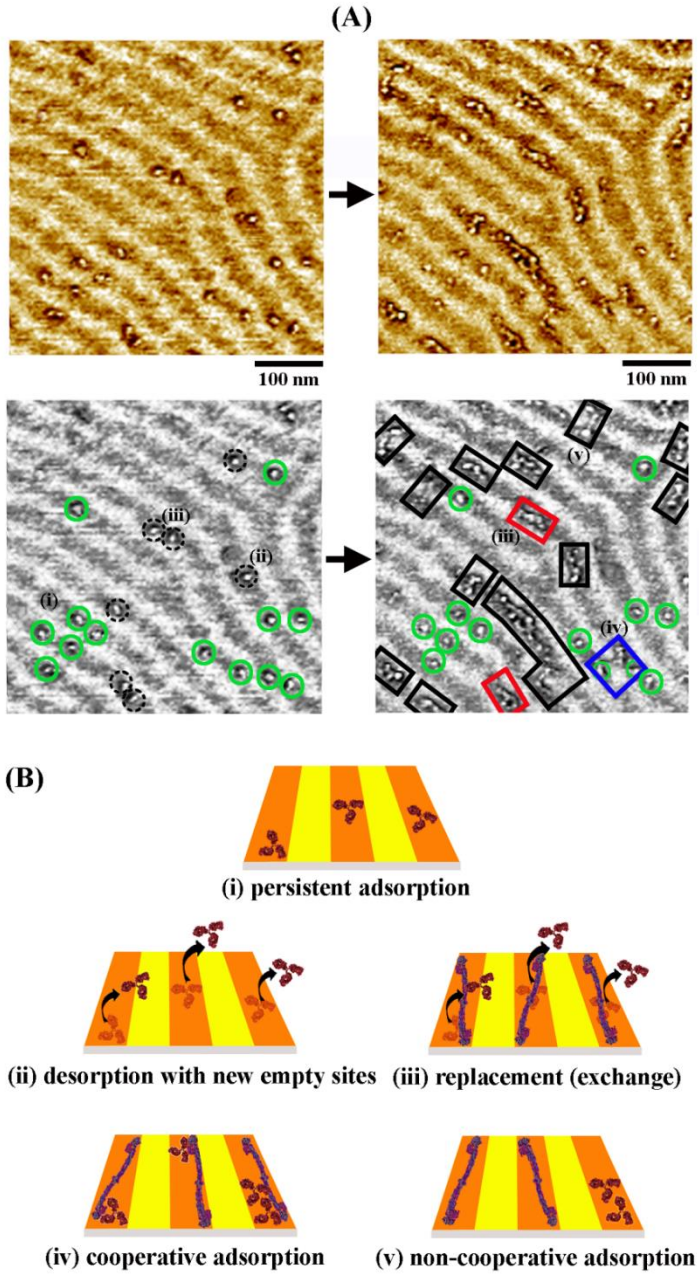

Figure 28. The five representative pathways that are commonly found in sequential protein adsorption events. (A) Representative AFM phase panels and their corresponding gray scale images showing protein adsorption evolution via the five different pathways. Proteins involved in the frequently observed adsorption events are marked using following color code: IgG molecules remain as undisturbed on the BCP surface after the exposure to a Fg solution (i, solid green circles), IgG molecules desorb after the Fg introduction, resulting in either empty surface sites (ii, black dashed circles) or sites now occupied by Fg (iii, red boxes), Fg molecules adsorb in close proximity to the initially bound IgG (iv, blue boxes), and at empty sites originally unoccupied by IgG (v, black boxes). (B) Schematics illustrating the five common protein adsorption pathways discussed above. The dynamic process of sequential protein adsorption can lead to (i) persistent adsorption, (ii) desorption with new empty sites, (iii) replacement/exchange, (iv) cooperative adsorption, and (v) noncooperative adsorption.

4.2.5 Three Stage Tracking of Individual Proteins

Next, I carried out three successive protein depositions of varying sequences for AFM tracking of individual proteins. The series of AFM panels displayed in Figure 29 correspond to the sequential protein deposition of IgG (1st stage) followed by Fg (2nd stage) and then by IgG (3rd stage) to a PS-b-PMMA surface, whereas the data set in Figure 30 pertains to the solution deposition of IgG (1st stage) followed by PBS (2nd stage) and subsequently by Fg (3rd stage). The high propensity of Fg replacing IgG, but not the reverse exchange, can be clearly seen in the IgG → Fg → IgG series in Figure 29. The transition from the 1st → 2nd stage yielded quite a few IgG molecules replaced by Fg molecules. On the contrary, the ensuing transition from the 2nd → 3rd stage caused no desorption of the Fg molecules adsorbed in the 2nd stage. This behavior was observed regardless of the specific pathways taken by the Fg molecules that led to their initial surface adsorption. The color-coded boxes in Figure 29 mark the exact type of the adsorption pathway utilized by given Fg molecules during the 2nd stage. The cases of Fg replacing IgG, cooperative Fg adsorption, and noncooperative Fg adsorption are indicated in red, blue, and black, respectively. Regardless of their initial adsorption pathways, all Fg molecules remained bound on the PS-b-PMMA surface and, subsequent IgG adsorption in the 3rd stage took place by landing on freely available surface sites. In the sequential treatment series of IgG → PBS → Fg in Figure 30, it is evident that no desorption of the initially adsorbed IgG molecules occurred during the 2nd stage of neat buffer treatment. In contrast, further introduction of Fg solution in the 3rd stage drove the persistently adsorbed IgG molecules to detach from the surface, even leading to IgG replacement by Fg.

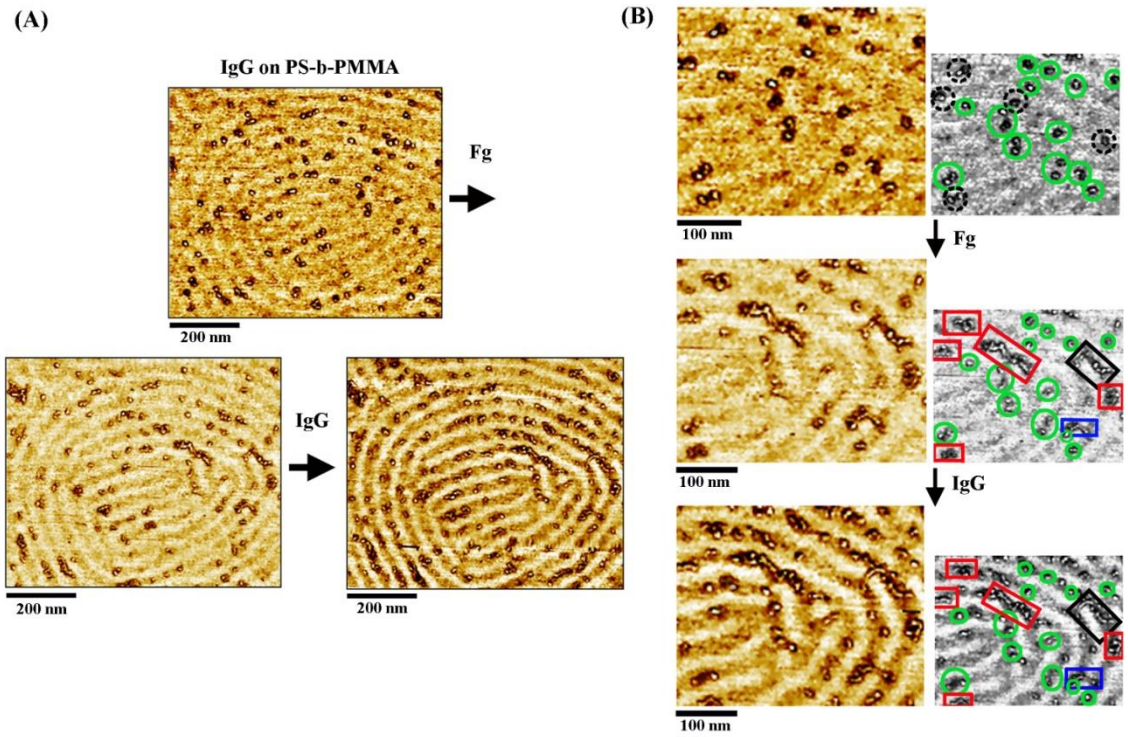

Figure 29. (A) Representative atomic force microscopy images displaying the same PS-b-PMMA areas consecutively exposed to a protein solution of immunoglobulin G (1st stage), fibrinogen (2nd stage), and immunoglobulin G (3rd stage). (B) A zoomed-in area of (A) is shown. The colored circles and boxes in the grey scale panels denote the different categories of the protein adsorption pathways, as detailed in Figure 28 with the same color code. From the sequence of AFM phase panels, it is evident that quite a few IgG molecules enclosed in red boxes were exchanged with Fg molecules after the 2nd stage. In contrast, no Fg adsorbed during the 2nd stage (red: exchange, blue: cooperative adsorption, white: noncooperative adsorption) desorbed after the ensuing IgG deposition in the 3rd stage. All Fg molecules stayed bound when comparing the 2nd and 3rd stage data. IgG molecules newly appearing on the surface after the 3rd stage adsorbed onto empty surface sitesthat are free of IgG or Fg from the previous stages.

4.2.6 Dominant Protein Exchange Direction and Adsorption/Desorption Tendency

In hemostasis, thrombosis, and biomaterials, bulk scale adsorption profiles of plasma proteins such as immunoglobulins and Fg have been extensively investigated.[4–7,9,127,209] In these studies, a protein exchange process that can occur on solid surfaces upon their exposure to different protein species under a competitive environment is now known as the Vroman effect.[4,8,202] In brief, the Vroman process refers to the protein exchange phenomenon where early adsorbers (the more abundant, faster, and lower molecular weight species) are replaced by later arriving, larger species with higher surface affinity over time. However, the majority of the previous studies on Vroman

exchange had to infer these molecular-level surface events indirectly from ensemble-averaged, spectroscopic, or optical signals. This was due to the fact that the techniques commonly used to study Vroman effect in the past relied on measuring the changes in resonance frequency,[19,99] surface plasmon resonance reflectivity,[101–103] IR absorption frequency,[19,27,31] fluorescence intensity,[89–92] and refractive index.[99,100,209] Although effective in providing ensemble-averaged signals, adsorption events taking place at the individual biomolecule level can only be deduced from collective protein signals. Yet, single protein behaviors can deviate significantly from the collective attributes of protein ensembles.[216–218] Furthermore, the Vroman exchange process was reported to occur on some but not all surfaces. It was demonstrated that, for a ternary mixture of serum albumin (SA), IgG, and Fg, no exchange of the initially bound species of SA and IgG by Fg was seen on a hydrophobic surface of hexamethyldisiloxane, whereas the initially adsorbed species were completely replaced by Fg on the hydrophilic surfaces, such as positively charged diaminocyclohexane and negatively charged acrylic acid.[7,208] Hence, it is not yet entirely clear how the effect will scale down to competitive protein adsorption cases occurring onto BCP nanodomain surfaces that can exhibit varying degrees of hydrophobicity/philicity.

In these aspects, my results in Figure 29 demonstrate that the protein exchange process of IgG by Fg indeed occurs on the nanoscale surfaces of PS-b-PMMA. More importantly, I provide direct experimental evidence at the single protein level that, regardless of the relative abundance of the two proteins, many events of Fg replacing IgG can indeed occur on PS-b-PMMA whereas no Fg molecules can be replaced by IgG. As further evidenced by data in Figure 30, such desorption/replacement of surface-bound IgG was triggered by the introduction of Fg, not by simply being exposed to a buffer solution. None of the initially bound IgG molecules left the BCP surface after the PBS treatment during the sequential introduction of IgG → PBS → Fg in Figure

30. On the contrary, it can be seen that some of those same IgG molecules, which persisted on the BCP after the 2nd stage, were readily desorbed and replaced by Fg in the 3rd stage. For Fg, no cases of desorption were observed upon its initial adsorption to the BCP surface, regardless of the next treatment involving IgG or neat buffer. Based on these observations, the AFM data in Figures 30 and 31 reveal the dominant protein exchange direction and adsorption/desorption tendencies of IgG and Fg on PS-b-PMMA through direct visualization of the pertinent events at the individual protein level.

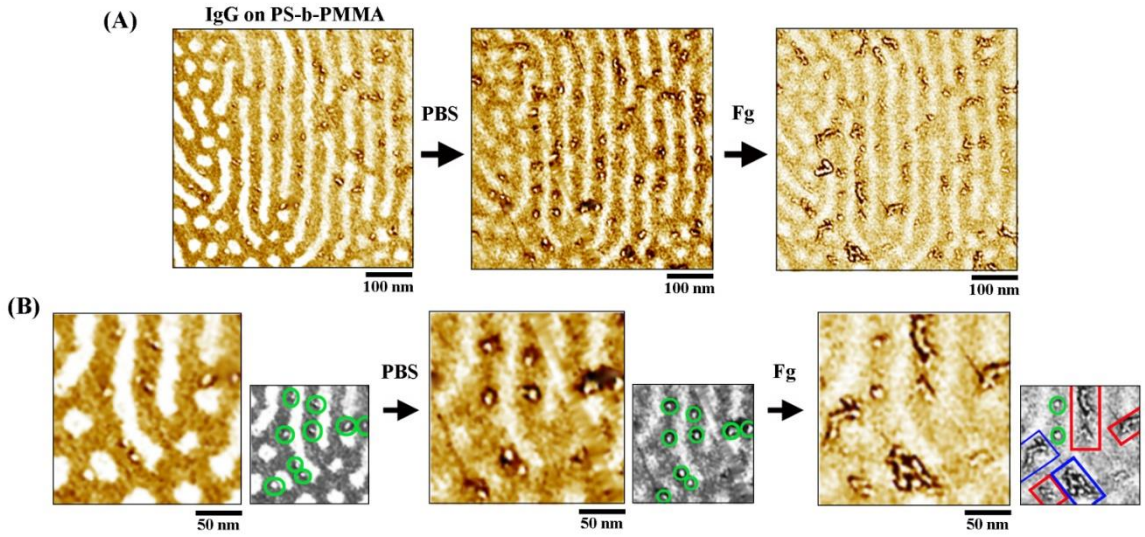

Figure 30. (A) The representative atomic force microscopy phase scans display typical protein adsorption behaviors observed from the sequential exposure of a PS-b-PMMA surface to a solution containing immunoglobulin G (1st stage), phosphate-buffered saline (2nd stage), and fibrinogen (3rd stage). (B) To better guide the eye for tracking individual proteins between each stage, the zoomed-in panels of an area in (A) are provided. The different categories of the protein adsorption pathways are marked for each protein using the same color code in Figure 28. After the 2nd stage of the neat buffer treatment, it can be seen that all IgG molecules adsorbed initially after the 1st stage remained bound on the surface. In contrast, the ensuing exposure of these surface-bound IgG molecules to Fg in the 3rd stage yielded many instances of IgG desorption and replacement.

4.2.7 Post-Adsorption Protein Rearrangement

I further examined the conformational changes associated with the average heights and widths of individual IgG proteins on PS-b-PMMA undergoing sequential solution treatments. Figure 31 shows a correlated data set including the AFM images and the line analysis results of IgG molecules adsorbed on the BCP surface before and after a sequential treatment. The scatter

plots in Figure 31(B and D) track the average height and width of IgG molecules, which are each assigned a specified identification number (ID), before and after their exposure to a Fg solution (Figure 31(A and B)) and to a neat PBS buffer (Figure 31(C and D)). For each protein, the height/width versus distance measurements were taken along six lines rotated by every 30°, bisecting the center of the protein. The size of the error bar associated with the width, therefore, can serve as an indication of the anisotropy of the protein footprint on the surface, i.e. the two-dimensional (2D) spread of a given IgG molecule. The scatter plots in Figure 31(B) show that the protein height decreased for the majority of the IgG molecules after the Fg treatment, whereas the overall width and the associated shape anisotropy increased. A similar trend was observed under the PBS buffer treatment. The average height of many IgG molecules displayed in Figure 31(B) decreased while their width increased. Although a representative data set is shown in Figure 31, the same trends were seen from a large data set. From ~250 IgG molecules upon exposure to a Fg solution, the average height decreased from its original value of 1.75 ± 0.20 nm to 1.56 ± 0.26 nm, whereas their average width changed from 14.65 ± 1.38 nm to 17.21 ± 1.65 nm. (Errors are standard deviations associated with the overall means from the IgG molecules) The mean height and width of each IgG molecule was obtained by averaging the respective values measured along the six different lines. Combined, these observations show that IgG molecules are initially adsorbed taller and narrower on the PS-b-PMMA surface and proceed to spread out in different lateral directions. Overall, this rearrangement process makes the IgG molecules to adapt a lower and more widespread configuration on the surface during subsequent solution treatment. I note that this post-adsorption conformational change of IgG occurred to be predominantly non-symmetrical. This anisotropic spreading frequently induced a slight elongation of the initially sphere-shaped IgG, making it appear v-shaped (IgG2, IgG8, IgG12, and IgG13 in Figure 31(A)).

Additionally, my data show that the post-adsorption rearrangement of IgG is a reversible process. Although not as frequently observed as the anisotropic spreading of sphere- to v-shaped transition, the reverse conformational change indeed occurs as demonstrated by IgG6 and IgG10 in Figure 31(A) where the molecule is more spatially isotropic in the later stage image.

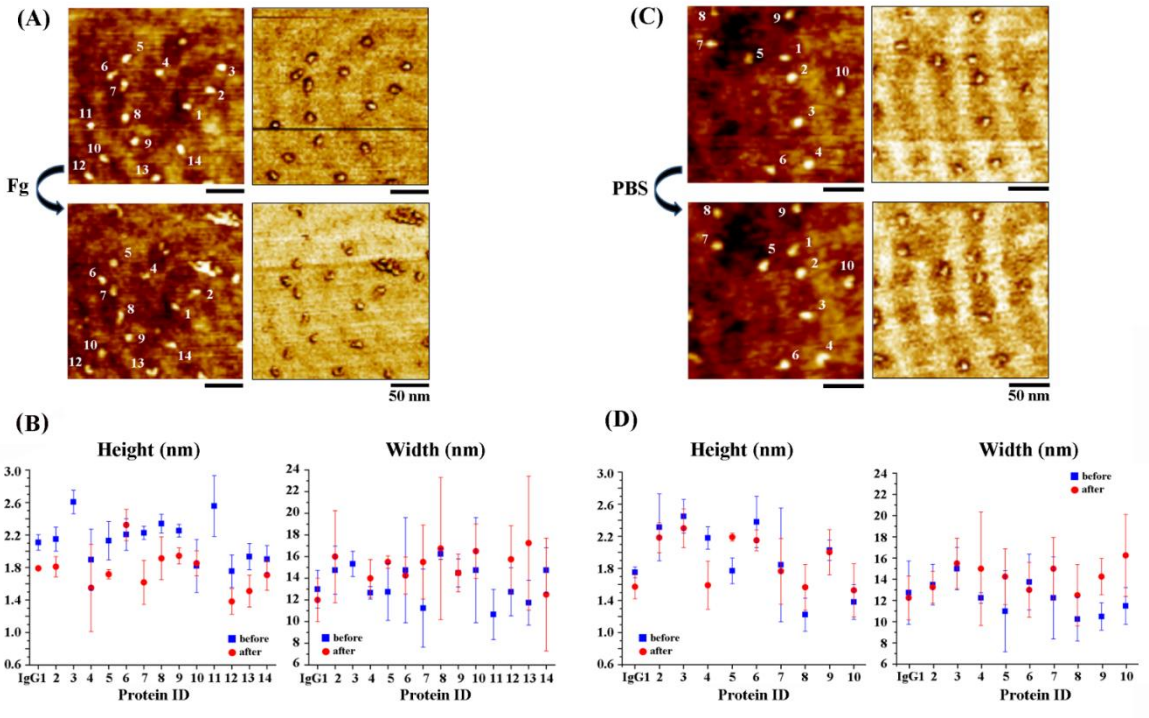

Figure 31. Individual immunoglobulin G molecules on a PS-b-PMMA surface were followed between different sequential adsorption treatments and their changes in height and width were analyzed. Each pair of AFM panels shown contains topographic (left) and phase (right) images. The two AFM panels on the left side of the arrow display IgG molecules adsorbed onto the PS-b-PMMA surface. The other two panels on the right side of the arrow are the scans after the following solution deposition of (A and B) Fg and (C and D) PBS. The line measurement profiles provided under the AFM data correspond to the average values of height and width measured from the individual proteins before (data in blue) and after (data in red) the indicated solution treatment. The width and height of each IgG molecule with the specified identification number (ID) were tracked between treatments for the line analysis plots. The error bars are from length analysis along six independent lines bisecting a given protein and serve as a measure for the protein shape anisotropy on the surface.

Direct evidence of post-adsorption conformational and orientational changes of single proteins has not been readily available so far, though such processes are widely adapted to explain reversible/irreversible protein adsorption and commonly assumed in various protein adsorption mechanisms.[5,11,92,104,217] My AFM data explicitly showing post-adsorption rearrangement processes associated with individual proteins on the nanoscale surface are significant in this regard.

In order to put these direct AFM tracking results in the context of pre-existing protein adsorption models, three models in the literature whose mechanisms include post-adsorption protein rearrangement as observed in my experiments are considered.[11,92,104,219–224] They are two-state, multi-state, and roll-over models.[14,92,221] According to a two-state adsorption model,[225] proteins can adsorb via a serial (reversible) or a parallel (both reversible and irreversible) route. In both routes, a surface-induced conformational change leads to a larger surface footprint of the adsorbed protein which, in turn, makes the protein irreversible for desorption due to its increased surface affinity upon restructuring. Similar scenarios of increasing protein footprints are also considered in a multiple-state adsorption model[221] whose mechanism permits the reversible existence of more than two distinct protein conformations on the surface. In the rollover model,[92] the orientation of proteins is thought to change on the surface from its initial 'end-on' to 'side-on' attachment over time. From the fact that I observed reversible post-adsorption conformational changes from IgG and that multiple distinctive shapes of IgG were identified upon rearrangement; the multi-stage model seems to describe my sequential adsorption processes the closest.

4.2.8 Protein Mobility on Surface and Self-Association Degree

Surface diffusion of adsorbed proteins was found to be negligible in my system, occurring at a much slower timescale than that of the conformational rearrangement. In the case of Fg, no protein diffusion to other surface sites was observed from my data. This lack of diffusion may be due to the conformation that Fg takes upon adsorption. All surface-adsorbed Fg displayed the protein long axis parallel to the surface, taking a 'lying-down' ('side-on') configuration, and no cases of 'standing-up' ('end-on') Fg were seen. This 'lying-down' configuration may cause a high energetic penalty for Fg to undergo surface detachment/reattachment, greatly decreasing its mobility on the BCP surface. Similar to my observation, a bulk scale study based on fluorescence

has also shown that there is no surface diffusion associated with Fg both on hydrophobic and hydrophilic surfaces.[226] For IgG, some instances of lateral translation were observed on the BCP surface. However, it should be noted that only a very small fraction (~ a few %) of IgG molecules moved on the surface and their average travel distance was less than the diameter of the protein, placing them on the same PS nanodomain they were originally found. The largest diffusion constant measured for IgG in my experiment was ~$5x10^{-15}$ cm^2/s. This value is comparable to the previously reported diffusion constant for another globular protein, lysozyme, which has a value of $9x10^{-16}$ cm^2/s.[224] Thus, during a post-adsorption evolution, surface-induced conformational change plays a much more important role than 2D protein diffusion in my system.

I also noticed that the adsorption behaviors of IgG and Fg differed in that self-association was frequently observed for Fg, but not for IgG. Self-association refers to protein adsorbing near its own kind, distinct from cooperative adsorption events pointing to the case of protein adsorbing near a protein of another kind. The large self-association effect of Fg adsorption is evident in the AFM data presented in Figures 26 and 27, where subsequent-stage Fg adsorption resulted in local regions of a higher Fg density due to self-association. The propensity was observed regardless of whether the BCP surface initially contained IgG or Fg. However, subsequent-stage IgG adsorption to the BCP surface containing either preadsorbed IgG or Fg molecules did not seem to induce the same level of self-association as Fg.

Pre-existing adsorption mechanisms such as clustering and tracking indicate similar self-association processes of proteins on surfaces.[11,222,223] In the surface cluster model, each i-mer (monomer, dimer, trimer..) attracts an incoming protein either directly next to the i-mer via a piggyback pathway or by diffusing towards an already-present cluster on the surface.[223] In comparison, the tracking model assumes that the approaching bulk proteins are attracted vertically

but repelled in the lateral direction by preadsorbed proteins and, thus, the sum of all electrostatic potentials is considered for tracking and guiding of adsorbing proteins in the vicinity of preadsorbed proteins.[11,222] Based on my observation of the extremely restricted lateral diffusion of Fg and no local/global formation of vertically stacked Fg molecules, the tracking model seems to better explain the sequential adsorption events taking place in my system.

4.2.9 Influence of Preadsorbed Surface on Subsequent Stage Protein Adsorption

The presence of already existing protein species on the surface from a prior stage may entirely change the adsorption behaviors of the subsequent stage protein species. In order to examine the potential effect of pristine versus preadsorbed PS-b-PMMA surfaces on subsequent stage protein adsorption, a large set of AFM data were collected from 5 independent samples subject to serial solution treatments. The single protein tracking data were then analyzed according to the different adsorption pathways as shown in Figure 28. The analysis was carried out by tracking at least 15 different locations of 2 x 2 μm^2 in size per sample. The plots shown in Figure 32 were subsequently obtained from the samples that were first treated with IgG then Fg. The y-axis of the top to bottom graphs in Figure 32(A), sharing the common x-axis as the number of preadsorbed IgG molecules, displays the total number of adsorbed Fg molecules, the number of Fg molecules adsorbed noncooperatively on isolated sites, the number of Fg adsorbed cooperatively adjacent to preadsorbed IgG, and the number of Fg molecules replacing IgG, respectively, all in units of counts per μm^2. A strong correlation was found between the number of newly adsorbed Fg molecules and the number of preadsorbed IgG proteins, see Figure 32(A). In Figure 32(B), the same four classes of Fg counts are charted on the y-axis, but this time using the bulk Fg solution concentration in $\mu g/mL$ as the common x-axis instead. Even for the same bulk Fg concentration, the number of newly adsorbed Fg molecules varied greatly on the different

BCP surfaces containing varying IgG amounts. The data in Figure 32(B) indicate that the subsequent stage Fg adsorption is less affected by the bulk Fg concentration than the preabsorbed IgG amount. Henceforth, I will refer to this behavior, where the amount of preadsorbed protein rather than the bulk concentration of the newly arriving species dictates the amount of protein adsorption in subsequent steps, as preadsorbed surface-associated behavior.

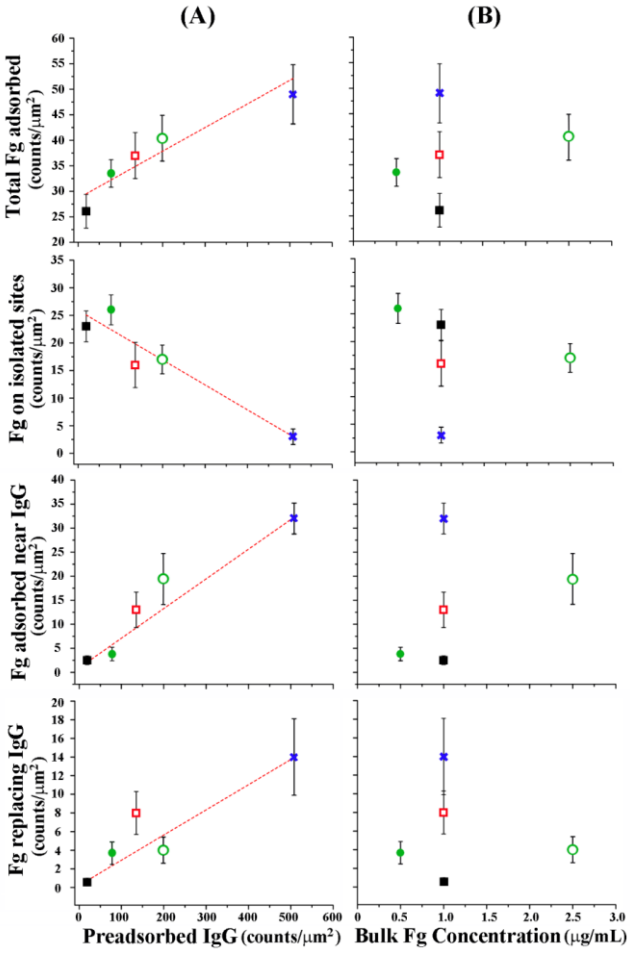

Figure 32. Preadsorbed surface-associated adsorption behavior identified from the sequential protein deposition experiment of immunoglobulin G followed by fibrinogen. (A) From top to bottom, the four graphs plot the number of preadsorbed IgG molecules versus the total number of adsorbed Fg, the number of noncooperatively adsorbed Fg, the number of cooperatively adsorbed Fg, and the number of Fg molecules replacing preadsorbed IgG in the unit of counts (molecules) per μm^2. A highly linear correlation, either positive or negative depending on the adsorption pathway taken, was found between the adsorbed Fg molecules and the number of preadsorbed IgG proteins on PS-b-PMMA. As a guide to the eye, linear fits through the data points are inserted along the data. (B) The same four classes of Fg counts are charted as a function of bulk Fg solution concentration in μg/mL. No correlation between the surface-adsorbed Fg amounts and the bulk Fg concentration was found.

Figure 33 further compares the distinctively different protein adsorption behaviors when they were introduced as an initial adsorber versus as a subsequent-stage adsorber to a PS-b-PMMA surface containing preadsorbed proteins. I carried out control experiments where protein adsorption profiles were attained after depositing IgG or Fg onto a clean BCP surface. Figure 33(A) displays the highly linear correlation between the adsorbed IgG amounts versus bulk IgG concentration found on a clean PS-b-PMMA surface. Similarly, on a neat BCP template, a strong linear relationship was observed between the surface-adsorbed Fg counts and Fg solution concentration, Figure 33(B). However, in the sequential protein deposition case of IgG → Fg, the amount of Fg adsorbed onto the surface of IgG-decorated BCP showed strong dependence on the preadsorbed IgG molecules, rather than the bulk Fg concentration. The concentrations of the IgG and Fg solutions used as the initial adsorber in my sequential adsorption experiments were kept intentionally low. This condition ensured that, if deposited onto a pristine PS-b-PMMA surface, the protein adsorption profiles will be linearly dependent on the bulk concentration as shown in Figure 33(A) and (B). The different adsorption outcomes yielded by the same protein of Fg on a neat versus decorated BCP surface can be clearly seen by comparing the two plots displayed in Figure 33(B) and (D). The linearity observed from Fg as the 1st adsorber species (Figure 33(B)) was no longer present when it was introduced as a 2nd absorber (Figure 33(D)). Data in Figure 33(C) show that, with increasing counts of preadsorbed IgG, the percent frequency of subsequent Fg adsorption via cooperative (blue) and exchange (red) pathways rise more or less linearly, whereas the case of noncooperative Fg adsorption (black) decreases. For instance, on a PS-b-PMMA surface containing 200 IgG/μm^2 versus 500 IgG/μm^2, the occurrence frequency of the cooperative, exchange, and noncooperative Fg adsorption types changed from approximately 50 %, 10 %, and 40 % to 65 %, 30 %, and 5 % of the total Fg adsorbed, respectively.

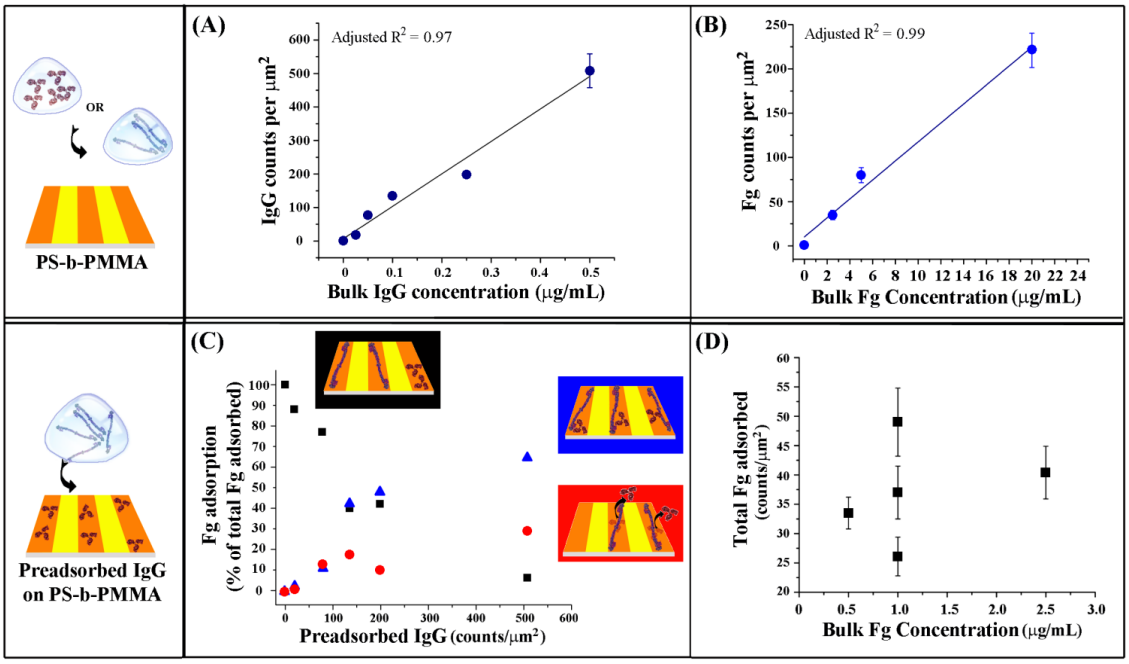

Figure 33. The protein adsorption behaviors found on neat versus preadsorbed PS-b-PMMA surfaces are summarized. (A and B) The control data were obtained by examining the case of (A) IgG and (B) Fg adsorption onto a clean PS-b-PMMA substrate with no preadsorbed proteins. (A) The plot of surface-adsorbed IgG counts versus bulk IgG solution concentrations shows a high linearity under the dilute concentration regime I used. (B) The surface-adsorbed Fg counts also increase linearly with the bulk Fg solution concentration for the concentration range employed. (C and D) The results correspond to the preadsorbed surface-associated adsorption behavior of Fg. (C) The occurrence frequencies of noncooperative Fg adsorption, cooperative Fg adsorption, and Fg replacing IgG are plotted. They are shown in black, blue, and red, respectively, in terms of its percent value with respect to the total Fg counts on the surface. Fg adsorption onto the IgG-decorated PS-b-PMMA surface is strongly dependent on the preadsorbed IgG amount. (D) The plot displays the total adsorbed Fg counts versus bulk concentration. Although the Fg solution concentrations used in the consecutive deposition experiments were well within the regime yielding a highly linear correlation between the adsorbed amounts versus the bulk concentration when deposited onto an untreated PS-b-PMMA surface as shown in (B), such linear relationship was no longer present in the case of the sequential Fg adsorption to IgG treated PS-b-PMMA.

At pH 7.4, which I used for all my adsorption experiments, the two proteins and the PS-b-PMMA surface are all charged negatively as they have isoelectric points (pIs) of 5.8-7.2 for IgG, 5.2 for Fg, 3.5-5 for PS, and 2-4 for PMMA.[9,227,228] From the electrostatic interaction point of view, the PS-b-PMMA surface precovered with IgG molecules will present more neutral or positively charged surface for the subsequent protein species to bind relative to the more negatively charged environment of a pristine PS-b-PMMA surface. This, in turn, may shift the energetic landscape of the surface such that the IgG decorated BCP surface is more attractive to the next

stage protein adsorption than the pristine BCP surface. My experimental results seem to indicate that, even at a low density of preadsorbed IgG molecules of less than 500 molecules per μm^2 (surface coverage of less than 10%), the energetic landscape of the PS-b-PMMA surface may be altered enough to dominate the adsorption characteristics of the subsequent stage protein adsorbers.

4.2.10 MC Simulations

The data in Figure 33 clearly point to the increased occurrence frequency of the cooperative and replacement events for Fg when they encounter more preadsorbed IgG proteins on the surface. I further substantiated the experimental outcomes for the different sequential adsorption cases with MC simulations of a simple model based on attractive and repulsive forces existing between the different protein particles and the underlying surface. The energetic considerations of protein-protein repulsion and protein-surface attraction used in the simple model of my MC simulations are discussed in detail in the Methods section. The simulations were then carried out for different 2D box scenarios,[229] an initially empty box (cases similar to Figure 33(A and B)) versus a box with a certain amount of preadsorbed proteins (cases shown in Figure 33(C and D)). IgG and Fg molecules were treated as small and large circular disks of 0.6σ and 1.2σ in size, respectively. σ is a unit length associated with the arithmetic mean of the diameters of the two proteins. The specified size difference for the two disks modelling IgG and Fg are chosen in my simulations to be consistent with the previously used estimations for IgG and 'lying-down' Fg.[210] Per my experimental observations, proteins are not allowed to move laterally once adsorbed on the surface and can only be desorbed in the simulations. Subsequently, changes occurring in the 2D box such as cooperative, noncooperative, and replacement events of the protein disks are examined.

Figure 34(A) plots the adsorption results by plotting the number of proteins per unit surface (counts/σ^2) as a function of the MC steps performed for the small proteins adsorbing/desorbing

in an empty 2D box. After an initial increase, the counts/σ^2 value reaches a steady state which does not change significantly despite the new adsorption/desorption events continuously occurring over the whole duration of the simulation. In Figure 34(B), such steady state value is plotted as a function of N_{max} where N is the number of proteins found on the surface, displaying a linear dependence up to a certain N_{max} value beyond which it reaches a plateau. This plateauing trend is due to the finite size of the simulation box that limits the maximum surface coverage while considering the protein-protein steric repulsion.[230,231] The same trends are qualitatively obtained when I considered the large proteins adsorbing/desorbing to/from an empty substrate as well (data not shown). Between the two cases of only the small protein and only the large protein adsorption onto an initially empty box, the differences were in the protein size-dependent adsorption strength and the magnitude of its steric repulsion. I kept the unit energy-related parameter of $\frac{k_B T}{\varepsilon}$ as 10^{-3} where ε is the interaction strength that I used as energy unit in the simulation, k_B is the Boltzmann constant, and T is the temperature. All simulation data and discussion in this paper correspond to this interaction energy regime. From the outcomes of single adsorbers in a clean box as shown in Figure 34, I also determined the simulation conditions for bulk concentrations and MC steps that best reflect the experimental conditions of low surface coverage and dilute bulk concentrations, leading to the linear dependence regimes in Figure 33(A) and (B). These simulation conditions were then used in subsequent computations to evaluate sequential adsorption cases.

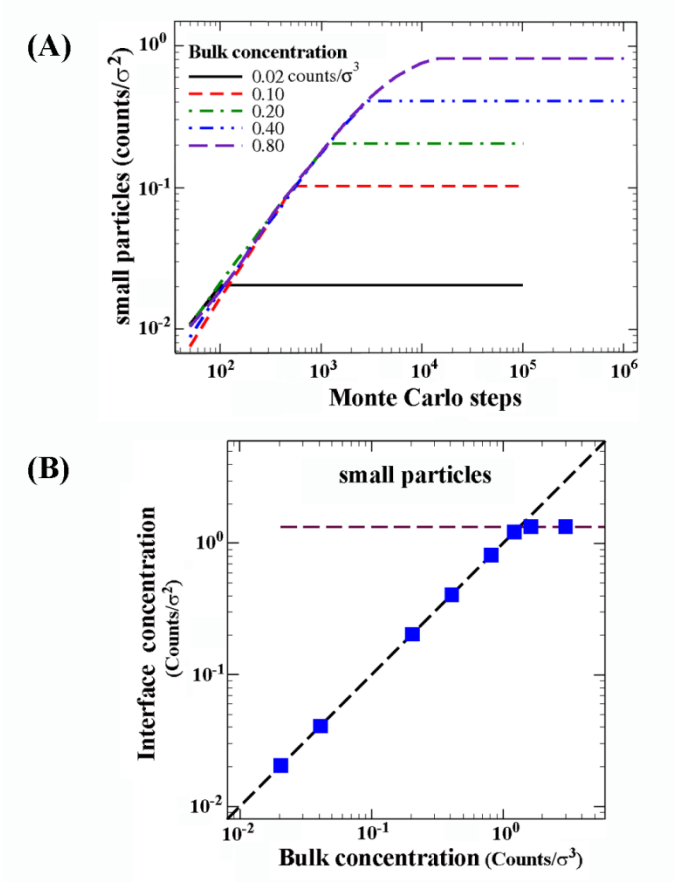

Figure 34. Monte Carlo simulation results showing the bulk concentration-dependent protein adsorption onto an initially empty 2D box. (A) The plots corresponding to different bulk concentrations display the number of small protein particles per unit surface adsorbed as a function of the MC steps in the MC simulations. A similar trend of bulk concentration-dependent behaviors was also adsorbed in the simulations of the large protein particles (data not shown). (B) The steady-state concentration of surface-adsorbed small particles as a function of the bulk concentration.

Accordingly, I performed a set of MC simulations in which I preadsorbed small proteins onto the surface before large proteins were introduced. Large proteins in this simulation set can be adsorbed and desorbed whereas the pre-bound, small proteins on the surface can only be desorbed. Illustrative snapshots of initial and final surface configurations from the simulations are provided in Figure 35(A). By analyzing the location of new large proteins with respect to the locations of the preadsorbed small proteins, I identified various adsorption events resulting from the simulation considerations and further compared them with the experimental findings. Indeed, adsorption cases in which large proteins adsorb in areas with no small proteins nearby were seen

in the simulation, consistent with the experimental observation of the noncooperative adsorption events. An example of such cases is indicated in the black square in the right panel of Figure 35(A). I identified adsorption cases from the simulation corresponding to the experimentally observed, cooperative behavior as well. An example of this case, large proteins adsorbing in close proximity of preadsorbed small proteins, is seen in the blue square in Figure 35(A). In addition, I found protein replacement events in the simulations as marked with the red square in Figure 35(A). Same as the experimental observations, adsorption of large proteins in these cases can displace one or more, preadsorbed, small proteins from the surface.

A statistical analysis of simulations was subsequently performed starting from 50 statistically independent initial samples. I compared the first and last configurations of each MC simulation and extracted the percentage of large proteins adsorbed on the substrate that belong to each case of cooperative, noncooperative, and replacement event. In the simulation, I considered that a large protein replaced one or more small proteins if at least one of the small proteins, located within a distance of 0.9σ from the adsorption loci in the initial configuration, was absent in the final configuration. If at least one small protein was present initially within the distance 1.5σ from the adsorption loci of a large protein and the large protein did not replace any small protein, I considered this a cooperative adsorption case. Finally, I classified the adsorption of a large protein as noncooperative, if none of the above conditions were satisfied. As a result, the sum of all distinct cases is always equal to the total number of large proteins adsorbed on the surface. The data obtained are subsequently plotted in Figure 35(B) as a function of the number of preadsorbed small proteins on the surface.

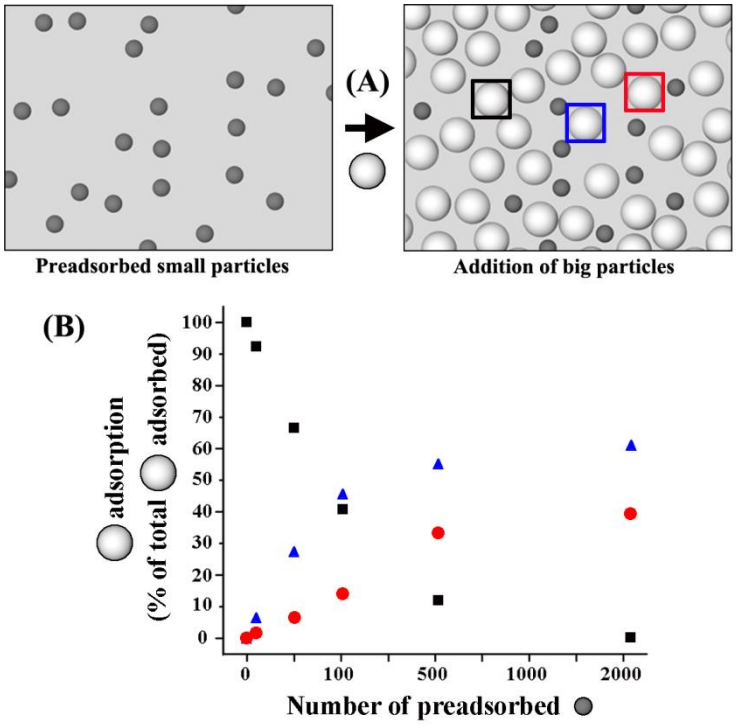

Figure 35. Monte Carlo simulation outcomes showing large protein adsorption onto a 2D box preadsorbed with small proteins. (A) Snapshots from the simulations starting from preadsorbed small protein particles (left) and showing representative cases (right) of large particles being adsorbed. It can be clearly seen that the MC simulation results also reveal the experimentally observed cases of large particles adsorbing near other large particles (black square), close to preadsorbed small particles (blue), or by substituting a preadsorbed small particle (red). (B) Occurrence frequencies of the large particle adsorption events found on the substrate are plotted as a function of the number of preadsorbed small particles. The frequencies for the three different cases of large particle adsorption are displayed in percentages relative to the total number of large particle adsorption events.

When compared to the data obtained from direct AFM tracking of sequential adsorption events in Figure 33(C), the MC simulation results in Figure 35 show similar overall trends in the Fg adsorption frequency between the cooperative, noncooperative, and replacement events as a function of preadsorbed particles. The good agreement between the experimental and simulation data suggests that the simplified MC simulation considerations of protein-protein repulsion and protein-polymer surface attraction can be effectively used to estimate the general trend in the different pathways of sequential protein adsorption in a qualitative manner. Quantitative comparisons between the experimental and simulation outcomes will require multilevel considerations, which is currently under progress. In this regard, the direct evidence of the

dominant sequential protein adsorption tendencies and key characteristics found in my experiments may serve as useful guides. Specifically, additional simulational considerations such as the shape anisotropy difference between the two proteins, the varying self-association degree between proteins of the same kind, and the surface-induced conformational rearrangement may enable quantitative correlations to my experimental outcomes from competitive protein adsorption.

4.3 Summary

I have revealed the major adsorption/desorption/replacement events and dominant pathways occurring in sequential protein adsorption onto a BCP surface and carried out MC simulations to further substantiate the experimental findings. AFM tracking of individual proteins adsorbed/desorbed on the same BCP surface locations between different treatments enabled me to unambiguously determine various adsorption-induced protein behaviors such as the occurrence frequency associated with specific adsorption pathway, post-adsorption conformational rearrangement adapted by given proteins, protein mobility on surface, self-association tendency during adsorption, and directionality in protein exchange. I have also showed that the adsorption profiles of subsequent stage proteins onto BCP surfaces with preadsorbed proteins differ dramatically from those cases without pretreatment. As a result, I have provided direct experimental evidence at the single protein level that was not readily available in the past, especially for systems involving multiple proteins on nanoscale BCP surfaces. Such experimental proof may promote a new mechanistic understanding of competitive protein adsorption, validation of existing adsorption mechanisms, and design of new biomaterials and biosensors. Therefore, my endeavors will be significant not only for advancing our fundamental knowledge on protein adsorption, but also for promoting technological applications of protein-polymer interfaces in the areas of biomaterials, biosensors/devices, and cell/tissue culture platforms.

4.4 Methods

4.4.1 Experimental Method

The periodic nanodomain surfaces of PS and PMMA blocks were prepared from PS-b-PMMA diblock copolymer (71% PS by weight) with an average molecular weight of 71.4 kDa and a polydispersity of 1.06 which was obtained from Polymer Source Inc. (Montreal, Canada). Silicon wafers were obtained from Silicon Quest, Inc. (San Jose, CA) and prepared into 1 by 1 cm^2 pieces. They were cleaned with ethanol, acetone, and toluene and spun dry before coating with the BCP. An ultrathin film of the BCP was produced by spincasting a 2 % (w/v) solution of the specified BCP in toluene onto the pre-cleaned Si surfaces at 3500 rpm for 1 min. The BCP substrate was subsequently annealed in an Ar atmosphere at 240 °C for 8 h with a transient ramp-up rate of 5 °C/min and a cooling rate of 2 °C/min. This thermal annealing process induced phase separation of the PS and PMMA chains in the BCP, yielding periodically alternating and chemically varying nanodomains known as half-cylinders and exposing repeating stripes of PS and PMMA blocks at the air/polymer interface with repeat units of 45 nm (PS to PS distance).[147]

Whole molecule bovine IgG and human plasma Fg were received from VWR Scientific Inc. (West Chester, PA) in a lyophilized form and reconstituted in PBS buffer (10 mM mixture of Na_2HPO_4 and NaH_2PO_4, 140 mM NaCl, 3 mM KCl, pH 7.4). The reconstituted protein solutions were then diluted to various concentrations ranging from 0.01 μg/mL to 25 μg/mL in PBS. A 10 μL volume of IgG or Fg solution with a desired concentration was deposited on the polymeric substrate for a period of 20 s to 15 min. The sample surfaces were then carefully rinsed with PBS multiple times and gently dried under a stream of N_2 prior to AFM imaging. For multistage protein deposition, the protein solution of interest was subsequently applied on the BCP containing preadsorbed protein species from the prior deposition step. Between each solution treatment, the

sample was rinsed with an ample amount of PBS and dried with N_2. A MultiMode 8 AFM interfaced with a Nanoscope V controller (Bruker Corp., Santa Barbara, CA) was used to collect the topography and phase images from the same BCP surface areas. The same set of IgG and Fg proteins on the same locations of PS-b-PMMA were tracked by performing high resolution AFM imaging between different solution treatments. Faithful protein tracking to record sequentially occurring adsorption events was possible by unambiguously resolving both the individual IgG and Fg protein molecules as well as the distinct nanoscopic details of underlying polymeric nanodomains after each deposition step. AFM was operated in a soft tapping mode at a scan speed of 1 Hz or lower, using Si tips with a typical resonant frequency of 60-70 kHz and a spring constant of ~1 N/m.

4.4.2 Simulational Method

MC simulations were carried out to further examine the experimental outcomes of preadsorbed surface-dependence on subsequent stage protein adsorption. Proteins were simply considered as circular disks which interact with one another via steric repulsion as defined below,

$$U(r_{ij}) = \varepsilon \left(\frac{\sigma}{r_{ij}}\right)^{12}$$

r_{ij} is their center-to-center distance, σ is the arithmetic mean of the diameters σ_i and σ_j of proteins i and j, respectively, and ε is the interaction strength that I used as energy unit in the simulations. To facilitate the numerical implementation with the use of periodic boundary conditions, the potential function was truncated at $r_c = 2.5\,\sigma_{ij}$ (where the interaction energy is already negligible with respect to ε) and a small constant term was added to $U(r_{ij})$ to ensure that it smoothly reaches the zero-value at r_c.[229] I used a 2D simulation box to mimic the polymer surface. Protein interactions with the polymer surface were subsequently modeled by reflecting

that, proportional to their size, proteins can adsorb on the polymer surface with an energy gain of ΔE as shown below.[230]

$$\Delta E\ (\sigma_i\ ) = \ -\varepsilon\ \left(\frac{\sigma_i}{\sigma}\right)^2$$

A MC step corresponds to the attempt to adsorb and desorb a protein chosen at random to and from the substrate. The total protein-protein interaction energy for N numbers of proteins on the substrate U_N can be expressed as the following.

$$U_N = \sum_{i=1}^{N-1} \sum_{j=i+1}^{N} U(r_{ij})$$

Using a Metropolis MC algorithm,[229] the acceptance probability for a new protein to be adsorbed or desorbed is written as below.

$$W(N \to N+1) = \ W(N+1 \to N) = \ \ \min[1, e^{-\frac{(\Delta U + \Delta E)}{k_B T}}]$$

$$\Delta U = \ U_{N+1} - \ U_N$$

k_B is the Boltzmann constant and T is the temperature. By setting ε as the unit energy, I controlled the parameter of $\frac{k_B T}{\varepsilon}$ that quantifies, in the simulations, the strength of the protein-protein interactions and of the surface-protein interactions with respect to room temperature. All data discussed below refer to $\frac{k_B T}{\varepsilon} \ll 1$, corresponding to a strong affinity between the surface and the proteins, and have been obtained for a squared simulation box of a linear size $L = 70\sigma$. I also used σ as the unit length and, to mimic the interplay between two different protein types in the experiments. I considered disks of two different diameters, 0.6σ and 1.2σ, respectively. The diameters of 0.6σ and 1.2σ chosen in this study are consistent with the previously used size estimations for IgG and 'lying-down' Fg, respectively.[210] In each simulation, I attempted to adsorb/desorb proteins of N_{max}, corresponding to a given bulk concentration.

5 Conclusions and Future Outlooks

The fundamentals of the protein adsorption and assembly behavior have been thoroughly investigated on chemically nanopatterned PS-b-PMMA block copolymer surfaces at the single molecular level in my dissertation studies through direct AFM imaging. Through these efforts, I have successfully mediated the protein assembly and packing behavior and have revealed the protein competitive adsorption principles at nanoscopic surfaces. I herein provide a brief summary of my research results to highlight my contributions to the development of biomaterials.

Chapter Two outlines my effort to achieve ordered protein packing at nanoscale through bottom-up approach. I examined the influence that changes on the periodicity and alignment of the phase-separated polymeric nanodomains have on the adsorption and packing characteristics of Fg molecules during their surface assembly. I have revealed the distinct adsorption configurations and the characteristic organization behaviors of both individual Fg molecules and Fg molecule assemblies on various BCP surfaces including sm PS-b-PMMA, com PS-b-PMMA, PS-r-PMMA, and dsa PS-b-PMMA via high resolution AFM imaging. My experimental results demonstrated that the physical dimension and alignment of the underlying surface nanofeatures can be used to control protein adsorption configuration and the protein packing density and alignments. To further substantiate the bioactivity of the surface-assembled proteins, I have demonstrated that the adsorbed Fg molecules on BCP can guide the selective seed and growth of calcium phosphate nanoparticles. I have also proven the retained biofunctionality of the BCP-bound Fg molecules by successfully activating microglial cells. The combined outcomes of this study may provide insights into the fundamental understanding of controlling protein adsorption behavior at both low surface coverage and surface saturation scenarios via bottom-up methods. My results also provide a facile approach to achieve protein nanopatterning with well-defined protein packing structure and retained biofunctionality.

In Chapter Three, I revealed the multicomponent protein adsorption processes at a nanoscale surface regime and investigated the competitive adsorption behavior of a binary protein mixture including BSA and Fg on both PS homopolymer and nanopatterned PS-b-PMMA surface. To achieve this, I used AFM to clearly resolve the nanoscopic topological details of both the protein molecules and the underlying surface nanofeatures. On both macroscopic and nanoscopic surfaces, the exchange process of the initially bound BSA protein being subsequentially replaced by the later adsorbed Fg was confirmed through direct imaging. Furthermore, I have identified the key stages of the turnover process from a BSA-dominant phase to Fg-dominant phase at different protein concentrations and systematically compared the time-dependent protein displacement event between the macroscopic and nanoscopic surfaces. In contrast to the result on the chemically homogeneous PS surface, BSA on the BCP surface with nanoscopic chemical heterogeneity was found to have a significantly prolonged residence time before displacement by Fg. I further discussed the molecular origin of this phenomenon, which is explained by the presence of the chemical interfaces between the PS and the PMMA nanodomains. The amphiphilic nature of the nanopatterned chemical interfaces provides more stable attachment for both hydrophobic and hydrophilic binding moieties on the protein, disfavoring their displacement from the surface. My research outcomes of this study presented for the first time at the molecular level the effect nanoscopic surface features have on the competitive protein adsorption behavior and may provide valuable insights in developing miniaturized biomaterials, biosensors, and biomedical devices.

In Chapter Four, I scrutinized the protein exchange phenomenon in sequential adsorption events through direct visual tacking at the nanoscale. I performed AFM imaging on the same surface sites at each adsorption stage and tracked individual protein molecules for their adsorption and desorption behaviors. I explicitly determined the major protein exchange pathways in the model system of IgG and Fg adsorbing onto nanopatterned PS-b-PMMA surface. I discussed the various adsorption-induced protein behaviors including the occurrence frequency of the specific adsorption pathway, post-adsorption conformational rearrangement adapted by certain proteins, protein mobility on the surface, tendency to self-associate

during adsorption, and directionality in protein exchange. I have also demonstrated via statistical results and MC simulations the prominent effect that preadsorbed protein has on the adsorption profile of the subsequently adsorbed protein at the surface. My research outcome in this chapter provides mechanistic insights into the competitive protein adsorption characteristics at single protein level through direct experimental evidence that was not readily feasible in the past, especially for studies at nanoscale surfaces. My results may also promote the applicational developments of various biomaterials and biomedical devices.

The collective results of my endeavor in these research works have demonstrated the great potential surface nanopatterned BCPs have in the field of protein adsorption. The nanoscopic surface chemical features of BCP can be applied not only as a scaffold for the guided protein nanoarray formation but also as an ideal template for time-resolved protein adsorption studies. These research outcomes can promote a fundamental understanding of protein adsorption on nanoscale surfaces and may shed light into the development of miniaturized biomaterials, more compact and sensitive biosensors, and various other biodevices. Future studies that combine nanopatterned BCP surfaces and high-resolution AFM techniques may provide more detailed protein adsorption investigations such as sub-protein level adsorption characteristics, protein adsorption kinetics using time-resolved single-molecular imaging, and protein-protein interaction in the surface adsorption event.

6 Bibliography

1. Sridharan, R., Cameron, A. R., Kelly, D. J., Kearney, C. J. & O'Brien, F. J. Biomaterial based modulation of macrophage polarization: A review and suggested design principles. *Mater. Today* **18,** 313–325 (2015).
2. Ratner, B. D. & Bryant, S. J. Biomaterials: Where We Have Been and Where We Are Going. *Annu. Rev. Biomed. Eng.* **6,** 41–75 (2004).
3. Vroman, L. & Adams, A. L. Findings with the recording ellipsometer suggesting rapid exchange of specific plasma proteins at liquid/solid interfaces. *Surf. Sci.* **16,** 438–446 (1969).
4. Vroman, L. & Adams, A. L. Identification of rapid changes at plasma–solid interfaces. *J. Biomed. Mater. Res.* **3,** 43–67 (1969).
5. Kidoaki, S. & Matsuda, T. Adhesion forces of the blood plasma proteins on self-assembled monolayer surfaces of alkanethiolates with different functional groups measured by an atomic force microscope. *Langmuir* **15,** 7639–7646 (1999).
6. Jung, S.-Y. *et al.* The Vroman effect: a molecular level description of fibrinogen displacement. *J. Am. Chem. Soc.* **125,** 12782–12786 (2003).
7. Lassen, B. & Malmsten, M. Competitive protein adsorption at plasma polymer surfaces. *J. Colloid Interface Sci.* **186,** 9–16 (1997).
8. Krishnan, A., Siedlecki, C. A. & Vogler, E. A. Mixology of protein solutions and the Vroman effect. *Langmuir* **20,** 5071–5078 (2004).
9. Kawai, T. *Clinical aspects of the plasma proteins*. (Springer Science & Business Media, 2013).
10. Latour, R. Biomaterials: protein-surface interactions. *... Biomater. Biomed. Eng.* 1–15 (2005). doi:10.1081/E-EBBE-120041856

11. Rabe, M., Verdes, D. & Seeger, S. Understanding protein adsorption phenomena at solid surfaces. *Adv. Colloid Interface Sci.* **162,** 87–106 (2011).

12. Peng, Z. G., Hidajat, K. & Uddin, M. S. Adsorption of bovine serum albumin on nanosized magnetic particles. *J. Colloid Interface Sci.* **271,** 277–283 (2004).

13. Engel, M. F. M., van Mierlo, C. P. M. & Visser, A. J. W. G. Kinetic and structural characterization of adsorption-induced unfolding of bovine $α$-lactalbumin. *J. Biol. Chem.* **277,** 10922–10930 (2002).

14. Billsten, P., Wahlgren, M., Arnebrant, T., McGuire, J. & Elwing, H. Structural changes of T4 lysozyme upon adsorption to silica nanoparticles measured by circular dichroism. *J. Colloid Interface Sci.* **175,** 77–82 (1995).

15. Moulin, A. M., O'shea, S. J., Badley, R. A., Doyle, P. & Welland, M. E. Measuring surface-induced conformational changes in proteins. *Langmuir* **15,** 8776–8779 (1999).

16. Giacomelli, C. E. & Norde, W. The adsorption--desorption cycle. Reversibility of the BSA--silica system. *J. Colloid Interface Sci.* **233,** 234–240 (2001).

17. Dee, K. C., Puleo, D. A. & Bizios, R. An introduction to tissue-biomaterial interactions. *Cell Mol. Biol.* **8,** 419–425 (2004).

18. van der Veen, M., Norde, W. & Stuart, M. C. Electrostatic interactions in protein adsorption probed by comparing lysozyme and succinylated lysozyme. *Colloids Surfaces B Biointerfaces* **35,** 33–40 (2004).

19. Roach, P., Farrar, D. & Perry, C. C. Interpretation of protein adsorption: surface-induced conformational changes. *J. Am. Chem. Soc.* **127,** 8168–8173 (2005).

20. Pamuła, E. & Rouxhet, P. G. Influence of surface properties of carbon fibres on the adsorption of catalase. *Carbon N. Y.* **43,** 1432–1438 (2005).

21. Raffaini, G. & Ganazzoli, F. Protein adsorption on a hydrophobic surface: a molecular dynamics study of lysozyme on graphite. *Langmuir* **26,** 5679–5689 (2009).

22. Vasina, E. N., Paszek, E., Nicolau Jr, D. V & Nicolau, D. V. The BAD project: data mining, database and prediction of protein adsorption on surfaces. *Lab Chip* **9,** 891–900 (2009).

23. Baptista-Pires, L. *et al.* Electrocatalytic tuning of biosensing response through electrostatic or hydrophobic enzyme--graphene oxide interactions. *Biosens. Bioelectron.* **61,** 655–662 (2014).

24. Firkowska-Boden, I., Zhang, X. & Jandt, K. D. Controlling Protein Adsorption through Nanostructured Polymeric Surfaces. *Adv. Healthc. Mater.* **7,** 1–19 (2018).

25. Lundqvist, M., Sethson, I. & Jonsson, B.-H. Protein adsorption onto silica nanoparticles: conformational changes depend on the particles' curvature and the protein stability. *Langmuir* **20,** 10639–10647 (2004).

26. Cai, K., Bossert, J. & Jandt, K. D. Does the nanometre scale topography of titanium influence protein adsorption and cell proliferation? *Colloids surfaces B Biointerfaces* **49,** 136–144 (2006).

27. Roach, P., Farrar, D. & Perry, C. C. Surface tailoring for controlled protein adsorption: effect of topography at the nanometer scale and chemistry. *J. Am. Chem. Soc.* **128,** 3939–3945 (2006).

28. Gagner, J. E., Qian, X., Lopez, M. M., Dordick, J. S. & Siegel, R. W. Effect of gold nanoparticle structure on the conformation and function of adsorbed proteins. *Biomaterials* **33,** 8503–8516 (2012).

29. dos Santos, E. A., Farina, M., Soares, G. A. & Anselme, K. Surface energy of hydroxyapatite and β-tricalcium phosphate ceramics driving serum protein adsorption and

osteoblast adhesion. *J. Mater. Sci. Mater. Med.* **19,** 2307–2316 (2007).

30. Cai, K. *et al.* Surface functionalized titanium thin films: zeta-potential, protein adsorption and cell proliferation. *Colloids Surfaces B Biointerfaces* **50,** 1–8 (2006).

31. Han, M., Sethuraman, A., Kane, R. S. & Belfort, G. Nanometer-scale roughness having little effect on the amount or structure of adsorbed protein. *Langmuir* **19,** 9868–9872 (2003).

32. Hammarin, G., Persson, H., Dabkowska, A. P. & Prinz, C. N. Enhanced laminin adsorption on nanowires compared to flat surfaces. *Colloids Surfaces B Biointerfaces* **122,** 85–89 (2014).

33. Jeon, S. I., Lee, J. H., Andrade, J. D. & De Gennes, P. Protein—surface interactions in the presence of polyethylene oxide: I. Simplified theory. *J. Colloid Interface Sci.* **142,** 149–158 (1991).

34. Gref, R. *et al.* 'Stealth'corona-core nanoparticles surface modified by polyethylene glycol (PEG): influences of the corona (PEG chain length and surface density) and of the core composition on phagocytic uptake and plasma protein adsorption. *Colloids Surfaces B Biointerfaces* **18,** 301–313 (2000).

35. Ma, H., Hyun, J., Stiller, P. & Chilkoti, A. 'Non-Fouling' Oligo (ethylene glycol)-Functionalized Polymer Brushes Synthesized by Surface-Initiated Atom Transfer Radical Polymerization. *Adv. Mater.* **16,** 338–341 (2004).

36. Ladd, J., Zhang, Z., Chen, S., Hower, J. C. & Jiang, S. Zwitterionic polymers exhibiting high resistance to nonspecific protein adsorption from human serum and plasma. *Biomacromolecules* **9,** 1357–1361 (2008).

37. Halperin, A. Polymer brushes that resist adsorption of model proteins: design parameters. *Langmuir* **15,** 2525–2533 (1999).

38. Elter, P., Lange, R. & Beck, U. Electrostatic and Dispersion Interactions during Protein Adsorption on Topographic Nanostructures. *Langmuir* **27,** 8767–8775 (2011).

39. Hartvig, R. A., van de Weert, M., Østergaard, J., Jorgensen, L. & Jensen, H. Protein Adsorption at Charged Surfaces: The Role of Electrostatic Interactions and Interfacial Charge Regulation. *Langmuir* **27,** 2634–2643 (2011).

40. Wiseman, M. E. & Frank, C. W. Antibody Adsorption and Orientation on Hydrophobic Surfaces. *Langmuir* **28,** 1765–1774 (2012).

41. Hay, D. I. & Moreno, E. C. Differential adsorption and chemical affinities of proteins for apatitic surfaces. *J. Dent. Res.* **58,** 930–942 (1979).

42. Liu, Y., Layrolle, P., de Bruijn, J., van Blitterswijk, C. & de Groot, K. Biomimetic coprecipitation of calcium phosphate and bovine serum albumin on titanium alloy. *J. Biomed. Mater. Res. Part A* **57,** 327–335 (2001).

43. Feng, B., Chen, J. & Zhang, X. Interaction of calcium and phosphate in apatite coating on titanium with serum albumin. *Biomaterials* **23,** 2499–2507 (2002).

44. Tatkare, D. Biomaterials Market by Type (Metallic, Polymeric, Ceramic, and Natural) and Application (Cardiovascular, Dental, Orthopedic, Wound Healing, Plastic, Surgery, Ophthalmology, Tissue Engineering) - Global Opportunity Analysis and Industry Forecast, 2014 - 20. **5285,** 1–15 (2016).

45. Lau, K. H. A., Bang, J., Kim, D. H. & Knoll, W. Self-assembly of protein nanoarrays on block copolymer templates. *Adv. Funct. Mater.* **18,** 3148–3157 (2008).

46. Jeong, C. K. *et al.* Electrical biomolecule detection using nanopatterned silicon via block copolymer lithography. *Small* **10,** 337–343 (2014).

47. Zhao, L. *et al.* Enzyme-Triggered Defined Protein Nanoarrays: Efficient Light-Harvesting

Systems to Mimic Chloroplasts. *ACS Nano* **11,** 938–945 (2017).

48. Lee, M. *et al.* Protein nanoarray on Prolinker surface constructed by atomic force microscopy dip-pen nanolithography for analysis of protein interaction. *Proteomics* **6,** 1094–1103 (2006).

49. Nam, J. M. *et al.* Bioactive protein nanoarrays on nickel oxide surfaces formed by dip-pen nanolithography. *Angew. Chemie - Int. Ed.* **43,** 1246–1249 (2004).

50. Lee, K. B., Park, S. J., Mirkin, C. A., Smith, J. C. & Mrksich, M. C. N. Protein Nanoarrays Generated by Dip-Pen Nanolithography. *Science (80-.).* **295,** 1702–1705 (2002).

51. Wu, B. & Kumar, A. Extreme ultraviolet lithography: A review. *J. Vac. Sci. Technol. B Microelectron. Nanom. Struct.* **25,** 1743 (2007).

52. Bloomstein, T. M., Marchant, M. F., Deneault, S., Hardy, D. E. & Rothschild, M. 22-nm immersion interference lithography. *Opt. Express* **14,** 6434 (2006).

53. Bloomstein, T. M. Critical issues in 157 nm lithography. *J. Vac. Sci. Technol. B Microelectron. Nanom. Struct.* **16,** 3154 (1998).

54. Park, M. Block Copolymer Lithography: Periodic Arrays of 1011 Holes in 1 Square Centimeter. *Science (80-.).* **276,** 1401–1404 (1997).

55. Shin, D.-S. *et al.* Protein patterning by maskless photolithography on hydrophilic polymer-grafted surface. *Biosens. Bioelectron.* **19,** 485–494 (2003).

56. Menard, E. *et al.* Micro- and Nanopatterning Techniques for Organic Electronic and Optoelectronic Systems. *Chem. Rev.* **107,** 1117–1160 (2007).

57. Hoff, J. D., Cheng, L.-J., Meyhöfer, E., Guo, L. J. & Hunt, A. J. Nanoscale Protein Patterning by Imprint Lithography. *Nano Lett.* **4,** 853–857 (2004).

58. Hua, F. *et al.* Polymer Imprint Lithography with Molecular-Scale Resolution. *Nano Lett.* **4,**

2467–2471 (2004).

59. Chou, S. Y. Sub-10 nm imprint lithography and applications. *J. Vac. Sci. Technol. B Microelectron. Nanom. Struct.* **15,** 2897 (1997).

60. Broers, A. N., Hoole, A. C. F. & Ryan, J. M. Electron beam lithography—Resolution limits. *Microelectron. Eng.* **32,** 131–142 (1996).

61. Rundqvist, J., Hoh, J. H. & Haviland, D. B. Directed Immobilization of Protein-Coated Nanospheres to Nanometer-Scale Patterns Fabricated by Electron Beam Lithography of Poly(ethylene glycol) Self-Assembled Monolayers. *Langmuir* **22,** 5100–5107 (2006).

62. Harnett, C. K., Satyalakshmi, K. M. & Craighead, H. G. Bioactive Templates Fabricated by Low-Energy Electron Beam Lithography of Self-Assembled Monolayers. *Langmuir* **17,** 178–182 (2001).

63. Denis, F. A., Pallandre, A., Nysten, B., Jonas, A. M. & Dupont-Gillain, C. C. Alignment and assembly of adsorbed collagen molecules induced by anisotropic chemical nanopatterns. *Small* **1,** 984–991 (2005).

64. Delaney, J. T., Smith, P. J. & Schubert, U. S. Inkjet printing of proteins. *Soft Matter* **5,** 4866 (2009).

65. Nie, Z. & Kumacheva, E. Patterning surfaces with functional polymers. *Nat. Mater.* **7,** 277–290 (2008).

66. Weeks, B. L., Vaughn, M. W. & DeYoreo, J. J. Direct Imaging of Meniscus Formation in Atomic Force Microscopy Using Environmental Scanning Electron Microscopy. *Langmuir* **21,** 8096–8098 (2005).

67. Piner, R. D., Zhu, J., Xu, F., Hong, S. & Mirkin, C. A. 'Dip-Pen' Nanolithography. *Science (80-.).* **283,** 661–663 (1999).

68. Valiokas, R., Vaitekonis, Š., Klenkar, G., Trinkūnas, G. & Liedberg, B. Selective Recruitment of Membrane Protein Complexes onto Gold Substrates Patterned by Dip-Pen Nanolithography. *Langmuir* **22,** 3456–3460 (2006).

69. Lee, S. W. *et al.* Biologically Active Protein Nanoarrays Generated Using Parallel Dip-Pen Nanolithography. *Adv. Mater.* **18,** 1133–1136 (2006).

70. Mendes, P. M., Yeung, C. L. & Preece, J. A. Bio-nanopatterning of Surfaces. *Nanoscale Res. Lett.* **2,** 373–384 (2007).

71. Christman, K. L., Enriquez-Rios, V. D. & Maynard, H. D. Nanopatterning proteins and peptides. *Soft Matter* **2,** 928 (2006).

72. Bates, F. S. & Fredrickson, G. H. Block copolymer thermodynamics: theory and experiment. *Annu. Rev. Phys. Chem.* **41,** 525–557 (1990).

73. Fredrickson, G. H. & Bates, F. S. Dynamics of Block Copolymers: Theory and Experiment. *Annu. Rev. Mater. Sci.* **26,** 501–550 (1996).

74. Cheng, J. Y. *et al.* Simple and Versatile Methods To Integrate Directed Self-Assembly with Optical Lithography Using a Polarity- Switched Photoresist. **4,** 4815–4823 (2010).

75. Liu, C.-C. *et al.* Fabrication of Lithographically Defined Chemically Patterned Polymer Brushes and Mats. *Macromolecules* **44,** 1876–1885 (2011).

76. Kim, S. O. *et al.* Epitaxial self-assembly of block copolymers on lithographically defined nanopatterned substrates. *Nature* **424,** 411–414 (2003).

77. Bhushan, B. & Schricker, S. R. A review of block copolymer-based biomaterials that control protein and cell interactions. *J. Biomed. Mater. Res. - Part A* **102,** 2467–2480 (2014).

78. Darling, S. B. Directing the self-assembly of block copolymers. *Prog. Polym. Sci.* **32,** 1152–1204 (2007).

79. Absolom, D. R., Zingg, W. & Neumann, A. W. Protein adsorption to polymer particles: Role of surface properties. *J. Biomed. Mater. Res.* **21,** 161–171 (1987).

80. Van Damme, H. S., Beugeling, T., Ratering, M. T. & Feijen, J. Protein adsorption from plasma onto poly(n-alkyl methacrylate) surfaces. *J. Biomater. Sci. Polym. Ed.* **3,** 69–84 (1992).

81. Kumar, N., Parajuli, O., Gupta, A. & Hahm, J. I. Elucidation of Protein Adsorption Behavior on Polymeric Surfaces: Toward High-Density, High-Payload Protein Templates. *Langmuir* **24,** 2688–2694 (2008).

82. Hahm, J.-I. Fundamentals of Nanoscale Polymer-Protein Interactions and Potential Contributions to Solid-State Nanobioarrays. *Langmuir* (2014). doi:10.1021/la404481t

83. Parajuli, O., Gupta, A., Kumar, N. & Hahm, J. Evaluation of Enzymatic Activity on Nanoscale Polystyrene-block-Polymethylmethacrylate Diblock Copolymer Domains. *J. Phys. Chem. B* **111,** 14022–14027 (2007).

84. Song, S., Ravensbergen, K., Alabanza, A., Soldin, D. & Hahm, J. I. Distinct adsorption configurations and self-Assembly characteristics of fibrinogen on chemically uniform and alternating surfaces including block copolymer nanodomains. *ACS Nano* **8,** 5257–5269 (2014).

85. Koo, J. *et al.* Control of Anti-Thrombogenic Properties: Surface-Induced Self-Assembly of Fibrinogen Fibers. *Biomacromolecules* **13,** 1259–1268 (2012).

86. Hahm, J. I. Functional polymers in protein detection platforms: Optical, electrochemical, electrical, mass-sensitive, and magnetic biosensors. *Sensors* **11,** 3327–3355 (2011).

87. Shashkova, S. & Leake, M. C. Single-molecule fluorescence microscopy review : shedding new light on old problems. *Biosci. Rep.* **37,** (2017).

88. AMBROSE, E. J. A Surface Contact Microscope for the study of Cell Movements. *Nature* **178,** 1194 (1956).

89. Cheng, Y. L., Darst, S. A. & Robertson, C. R. Bovine serum albumin adsorption and desorption rates on solid surfaces with varying surface properties. *J. Colloid Interface Sci.* **118,** 212–223 (1987).

90. Wertz, C. F. & Santore, M. M. Effect of Surface Hydrophobicity on Adsorption and Relaxation Kinetics of Albumin and Fibrinogen: Single-Species and Competitive Behavior. *Langmuir* **17,** 3006–3016 (2001).

91. Wertz, C. F. & Santore, M. M. Adsorption and relaxation kinetics of albumin and fibrinogen on hydrophobic surfaces: single-species and competitive behavior. *Langmuir* **15,** 8884–8894 (1999).

92. Wertz, C. F. & Santore, M. M. Adsorption and reorientation kinetics of lysozyme on hydrophobic surfaces. *Langmuir* **18,** 1190–1199 (2002).

93. Förster, T. . Transfer Mechanisms of Electronic Excitation Energy. *Radiat. Res. Suppl.* **2,** 326–339 (1960).

94. Hussain, S. A. An introduction to fluorescence resonance energy transfer (FRET). *arXiv Prepr. arXiv0908.1815* (2009).

95. Liao, J., Xiong, Z., Way, G. & Madarha, V. Novel Quantitative FRET technology to Determine Protein Interaction Dissociation Constant and Enzymatic Kinetics in Solution for SUMOylation Cascade. *FASEB J.* **30,** 819.11-819.11 (2016).

96. Langdon, B. B., Kastantin, M., Walder, R. & Schwartz, D. K. Interfacial Protein − Protein Associations. (2014).

97. von Voithenberg, L. & Lamb, D. C. Single Pair Förster Resonance Energy Transfer: A

Versatile Tool To Investigate Protein Conformational Dynamics. *BioEssays* **40,** 1700078--n/a (2018).

98. Chung, H. S., Piana-Agostinetti, S., Shaw, D. E. & Eaton, W. A. Structural origin of slow diffusion in protein folding. *Science (80-.).* **349,** 1504 LP-1510 (2015).

99. Rechendorff, K., Hovgaard, M. B., Foss, M., Zhdanov, V. P. & Besenbacher, F. Enhancement of protein adsorption induced by surface roughness. *Langmuir* **22,** 10885–10888 (2006).

100. Ying, P., Yu, Y., Jin, G. & Tao, Z. Competitive protein adsorption studied with atomic force microscopy and imaging ellipsometry. *Colloids Surfaces B Biointerfaces* **32,** 1–10 (2003).

101. Green, R. J., Davies, J., Davies, M. C., Roberts, C. J. & Tendler, S. J. B. Surface plasmon resonance for real time in situ analysis of protein adsorption to polymer surfaces. *Biomaterials* **18,** 405–413 (1997).

102. Breault-turcot, J., Chaurand, P. & Masson, J.-F. Unravelling nonspecific adsorption of complex protein mixture on surfaces with SPR and MS. *Anal. Chem.* **86,** 9612–9619 (2014).

103. Arima, Y. & Iwata, H. Effects of surface functional groups on protein adsorption and subsequent cell adhesion using self-assembled monolayers. *J. Mater. Chem.* **17,** 4079–4087 (2007).

104. Calonder, C., Tie, Y. & Van Tassel, P. R. History dependence of protein adsorption kinetics. *Proc. Natl. Acad. Sci.* **98,** 10664–10669 (2001).

105. Ball, V. & Ramsden, J. J. Absence of surface exclusion in the first stage of lysozyme adsorption is driven through electrostatic self-assembly. *J. Phys. Chem. B* **101,** 5465–5469 (1997).

106. Tie, Y., Calonder, C. & Van Tassel, P. R. Protein adsorption: kinetics and history

dependence. *J. Colloid Interface Sci.* **268,** 1–11 (2003).

107. Dolatshahi-Pirouz, A. *et al.* Bovine serum albumin adsorption on nano-rough platinum surfaces studied by QCM-D. *Colloids Surfaces B Biointerfaces* **66,** 53–59 (2008).

108. Xu, H., Bjerneld, E. J., Käll, M. & Börjesson, L. Spectroscopy of single hemoglobin molecules by surface enhanced Raman scattering. *Phys. Rev. Lett.* **83,** 4357 (1999).

109. Podstawka, E., Ozaki, Y. & Proniewicz, L. M. Adsorption of S—S Containing Proteins on a Colloidal Silver Surface Studied by Surface-Enhanced Raman Spectroscopy. *Appl. Spectrosc.* **58,** 1147–1156 (2004).

110. Han, X. X., Huang, G. G., Zhao, B. & Ozaki, Y. Label-free highly sensitive detection of proteins in aqueous solutions using surface-enhanced Raman scattering. *Anal. Chem.* **81,** 3329–3333 (2009).

111. Cui, L., Yao, M., Ren, B. & Zhang, K. S. Sensitive and versatile detection of the fouling process and fouling propensity of proteins on polyvinylidene fluoride membranes via surface-enhanced Raman spectroscopy. *Anal. Chem.* **83,** 1709–1716 (2011).

112. Ray, S. & Shard, A. G. Quantitative Analysis of Adsorbed Proteins by X-ray Photoelectron Spectroscopy. *Anal. Chem.* **83,** 8659–8666 (2011).

113. Morin, C. *et al.* Selective adsorption of protein on polymer surfaces studied by soft X-ray photoemission electron microscopy. *J. Electron Spectros. Relat. Phenomena* **137–140,** 785–794 (2004).

114. Li, L. *et al.* X-ray Microscopy Studies of Protein Adsorption on a Phase-Segregated Polystyrene/Polymethyl Methacrylate Surface. 1. Concentration and Exposure-Time Dependence for Albumin Adsorption. *J. Phys. Chem. B* **110,** 16763–16773 (2006).

115. Leung, B. O. *et al.* X-ray Spectromicroscopy Study of Protein Adsorption to a Polystyrene

- Polylactide Blend. 1838–1845 (2009).

116. Meyer, G. & Amer, N. M. Simultaneous measurement of lateral and normal forces with an optical-beam-deflection atomic force microscope. *Appl. Phys. Lett.* **57,** 2089–2091 (1990).

117. Grafström, S. Analysis of lateral force effects on the topography in scanning force microscopy. *J. Vac. Sci. Technol. B Microelectron. Nanom. Struct.* **12,** 1559 (1994).

118. Warmack, R. J., Zheng, X. -Y., Thundat, T. & Allison, D. P. Friction effects in the deflection of atomic force microscope cantilevers. *Rev. Sci. Instrum.* **65,** 394–399 (1994).

119. Möller, C., Allen, M., Elings, V., Engel, A. & Müller, D. J. Tapping-Mode Atomic Force Microscopy Produces Faithful High-Resolution Images of Protein Surfaces. *Biophys. J.* **77,** 1150–1158 (1999).

120. Sit, P. S. & Marchant, R. Surface-dependent Conformations of Human Fibrinogen Observed by Atomic Force Microscopy under Aqueous Conditions. *Thromb. Haemost.* **82,** 1053–1060 (1999).

121. San Paulo, A. & García, R. High-Resolution Imaging of Antibodies by Tapping-Mode Atomic Force Microscopy: Attractive and Repulsive Tip-Sample Interaction Regimes. *Biophys. J.* **78,** 1599–1605 (2000).

122. Hahm, J., Lopes, W. A., Jaeger, H. M. & Sibener, S. J. Defect evolution in ultrathin films of polystyrene-block-polymethylmethacrylate diblock copolymers observed by atomic force microscopy. *J. Chem. Phys.* **109,** 10111–10114 (1998).

123. Wang, Y., Song, R., Li, Y. & Shen, J. Understanding tapping-mode atomic force microscopy data on the surface of soft block copolymers. *Surf. Sci.* **530,** 136–148 (2003).

124. Siedlecki, C. a & Marchant, R. E. Atomic force microscopy for characterization of the biomaterial interface. *Biomaterials* **19,** 441–454 (1998).

125. Toscano, A. & Santore, M. M. Fibrinogen Adsorption on Three Silica-Based Surfaces: Conformation and Kinetics. *Langmuir* **22,** 2588–2597 (2006).

126. Keller, T. F. *et al.* How the Surface Nanostructure of Polyethylene Affects Protein Assembly and Orientation. *ACS Nano* **5,** 3120–3131 (2011).

127. Cavic, B. A. & Thompson, M. Adsorptions of Plasma Proteins and Their Elutabilities from a Polysiloxane Surface Studied by an On-Line Acoustic Wave Sensor. *Anal. Chem.* **72,** 1523–1531 (2000).

128. Hall, C. E. The Fibrinogen Molecule: Its Size, Shape, and Mode of Polymerization. *J. Cell Biol.* **5,** 11–27 (1959).

129. Weisel, J. W., Phillips, G. N. & Cohen, C. A model from electron microscopy for the molecular structure of fibrinogen and fibrin. *Nature* **289,** 263–267 (1981).

130. Weisel, J., Stauffacher, C., Bullitt, E. & Cohen, C. A model for fibrinogen: domains and sequence. *Science (80-.).* **230,** 1388–1391 (1985).

131. Tapon-Bretaudiere, J. Hemostasis and Thrombosis. Basic Principles and Clinical Practice, Fourth Edition. Robert W. Colman, Jack Hirsh, Victor J. Marder, Alexander W. Clowes, and James N. George, eds. Philadelphia, PA: Lippincott Williams & Wilkins, 2001, 1578 pp., $249.00, har. *Clin. Chem.* **49,** 345–346 (2003).

132. Yang, Z., Mochalkin, I., Veerapandian, L., Riley, M. & Doolittle, R. F. CRYSTAL STRUCTURE OF NATIVE CHICKEN FIBRINOGEN. (2000). doi:10.2210/pdb1ei3/pdb

133. Ortega-Vinuesa, J. L., Tengvall, P. & Lundström, I. Molecular packing of HSA, IgG, and fibrinogen adsorbed on silicon by AFM imaging. *Thin Solid Films* **324,** 257–273 (1998).

134. Cacciafesta, P., Humphris, A. D. L., Jandt, K. D. & Miles, M. J. Human Plasma Fibrinogen Adsorption on Ultraflat Titanium Oxide Surfaces Studied with Atomic Force Microscopy.

Langmuir **16,** 8167–8175 (2000).

135. Jandt, K. D. Atomic force microscopy of biomaterials surfaces and interfaces. *Surf. Sci.* **491,** 303–332 (2001).

136. Marchin, K. L. & Berrie, C. L. Conformational Changes in the Plasma Protein Fibrinogen upon Adsorption to Graphite and Mica Investigated by Atomic Force Microscopy. *Langmuir* **19,** 9883–9888 (2003).

137. Van De Keere, I., Willaert, R., Hubin, A. & Vereecken, J. Interaction of Human Plasma Fibrinogen with Commercially Pure Titanium as Studied with Atomic Force Microscopy and X-ray Photoelectron Spectroscopy. *Langmuir* **24,** 1844–1852 (2008).

138. Xu, L.-C. & Siedlecki, C. A. Atomic Force Microscopy Studies of the Initial Interactions between Fibrinogen and Surfaces. *Langmuir* **25,** 3675–3681 (2009).

139. Averett, L. E. & Schoenfisch, M. H. Atomic force microscope studies of fibrinogen adsorption. *Analyst* **135,** 1201 (2010).

140. Wasilewska, M. & Adamczyk, Z. Fibrinogen Adsorption on Mica Studied by AFM and in Situ Streaming Potential Measurements. *Langmuir* **27,** 686–696 (2011).

141. Protopopova, A. D. *et al.* Visualization of fibrinogen αC regions and their arrangement during fibrin network formation by high-resolution AFM. *J. Thromb. Haemost.* **13,** 570–579 (2015).

142. Veklich, Y. I., Gorkun, O. V, Medved, L. V, Nieuwenhuizen, W. & Weisel, J. W. Carboxyl-terminal portions of the alpha chains of fibrinogen and fibrin. Localization by electron microscopy and the effects of isolated alpha C fragments on polymerization. *J. Biol. Chem.* **268,** 13577–13585 (1993).

143. Kumbar, S., Laurencin, C. & Deng, M. *Natural and synthetic biomedical polymers*.

(Newnes, 2014).

144. Hahm, J. & Sibener, S. J. Cylinder Alignment in Annular Structures of Microphase-Separated Polystyrene-b-Poly(methyl methacrylate). *Langmuir* **16,** 4766–4769 (2000).

145. Hahm, J. & Sibener, S. J. Time-resolved atomic force microscopy imaging studies of asymmetric PS-b-PMMA ultrathin films: Dislocation and disclination transformations, defect mobility, and evolution of nanoscale morphology. *J. Chem. Phys.* **114,** 4730 (2001).

146. Morkved, T. L. L., Lopes, W. a. A., Hahm, J., Sibener, S. J. J. & Jaeger, H. M. M. Silicon nitride membrane substrates for the investigation of local structure in polymer thin films. *Polymer (Guildf).* **39,** 3871–3875 (1998).

147. Kumar, N. & Hahm, J. I. Nanoscale Protein Patterning Using Self-Assembled Diblock Copolymers. *Langmuir* **21,** 6652–6655 (2005).

148. Laudano, A. P., Cottrell, B. A. & Doolittle, R. F. SYNTHETIC PEPTIDES MODELED ON FIBRIN POLYMERIZATION SITES. *Ann. N. Y. Acad. Sci.* **408,** 315–329 (1983).

149. Budzynski, A. Z. & Shainoff, J. R. Fibrinogen and fibrin: Biochemistry and pathophysiology. *Crit. Rev. Oncol. Hematol.* **6,** 97–146 (1986).

150. Weisel, J. W. Fibrin assembly. Lateral aggregation and the role of the two pairs of fibrinopeptides. *Biophys. J.* **50,** 1079–1093 (1986).

151. Xie, T. *et al.* Surface Assembly Configurations and Packing Preferences of Fibrinogen Mediated by the Periodicity and Alignment Control of Block Copolymer Nanodomains. *ACS Nano* **10,** 7705–7720 (2016).

152. LAURENS, N., KOOLWIJK, P. & DE MAAT, M. P. M. Fibrin structure and wound healing. *J. Thromb. Haemost.* **4,** 932–939 (2006).

153. Yakovlev, S. *et al.* Conversion of Fibrinogen to Fibrin: Mechanism of Exposure of tPA-

and Plasminogen-Binding Sites†. *Biochemistry* **39,** 15730–15741 (2000).

154. Veklich, Y., Ang, E. K., Lorand, L. & Weisel, J. W. The complementary aggregation sites of fibrin investigated through examination of polymers of fibrinogen with fragment E. *Proc. Natl. Acad. Sci.* **95,** 1438–1442 (1998).

155. Chen, G., Ni, N., Wang, B. & Xu, B. Fibrinogen Nanofibril Growth and Self-Assembly on Au (1,1,1) Surface in the Absence of Thrombin. *ChemPhysChem* **11,** 565–568 (2009).

156. Kumar, N., Parajuli, O. & Hahm, J. I. Two-Dimensionally Self-Arranged Protein Nanoarrays on Diblock Copolymer Templates. *J. Phys. Chem. B* **111,** 4581–4587 (2007).

157. Song, S. *et al.* Nanoscale protein arrays of rich morphologies via self-assembly on chemically treated diblock copolymer surfaces. *Nanotechnology* **24,** 95601 (2013).

158. Rao, S. P. S. *et al.* Fibrinogen structure in projection at 18 Å resolution. *J. Mol. Biol.* **222,** 89–98 (1991).

159. Adamczyk, Z., Barbasz, J. & Cieśla, M. Mechanisms of Fibrinogen Adsorption at Solid Substrates. *Langmuir* **27,** 6868–6878 (2011).

160. Ortega-Vinuesa, J. L., Tengvall, P. & Lundström, I. Aggregation of HSA, IgG, and Fibrinogen on Methylated Silicon Surfaces. *J. Colloid Interface Sci.* **207,** 228–239 (1998).

161. Kalasin, S. & Santore, M. M. Non-specific adhesion on biomaterial surfaces driven by small amounts of protein adsorption. *Colloids Surfaces B Biointerfaces* **73,** 229–236 (2009).

162. Bai, Z., Filiaggi, M. J. & Dahn, J. R. Fibrinogen adsorption onto 316L stainless steel, Nitinol and titanium. *Surf. Sci.* **603,** 839–846 (2009).

163. Weisel, J. W. Cross-linked gamma-chains in fibrin fibrils bridge transversely between strands: no. *J. Thromb. Haemost.* **2,** 394–399 (2004).

164. Chernysh, I. N., Nagaswami, C. & Weisel, J. W. Visualization and identification of the

structures formed during early stages of fibrin polymerization. *Blood* **117,** 4609–4614 (2011).

165. DUCHEYNE, P. & CUCKLER, J. M. Bioactive Ceramic Prosthetic Coatings. *Clin. Orthop. Relat. Res.* **NA;,** 102???114 (1992).

166. YOSHINARI, M., OHTSUKA, Y. & DERAND, T. Thin hydroxyapatite coating produced by the ion beam dynamic mixing method. *Biomaterials* **15,** 529–535 (1994).

167. Li, T., Lee, J., Kobayashi, T. & Aoki, H. Hydroxyapatite coating by dipping method, and bone bonding strength. *J. Mater. Sci. Mater. Med.* **7,** 355–357 (1996).

168. Ducheyne, P., Radin, S., Heughebaert, M. & Heughebaert, J. C. Calcium phosphate ceramic coatings on porous titanium: effect of structure and composition on electrophoretic deposition, vacuum sintering and in vitro dissolution. *Biomaterials* **11,** 244–254 (1990).

169. Tsui, Y. C., Doyle, C. & Clyne, T. W. Plasma sprayed hydroxyapatite coatings on titanium substrates Part 1: Mechanical properties and residual stress levels. *Biomaterials* **19,** 2015–2029 (1998).

170. Haddow, D. B., James, P. F. & Van Noort, R. Characterization of sol-gel surfaces for biomedical applications. *J. Mater. Sci. Mater. Med.* **7,** 255–260 (1996).

171. He, G. *et al.* Phosphorylation of Phosphophoryn Is Crucial for Its Function as a Mediator of Biomineralization. *J. Biol. Chem.* **280,** 33109–33114 (2005).

172. Toworfe, G. K., Composto, R. J., Shapiro, I. M. & Ducheyne, P. Nucleation and growth of calcium phosphate on amine-, carboxyl- and hydroxyl-silane self-assembled monolayers. *Biomaterials* **27,** 631–642 (2006).

173. Wei, G., Reichert, J., Bossert, J. & Jandt, K. D. Novel Biopolymeric Template for the Nucleation and Growth of Hydroxyapatite Crystals Based on Self-Assembled Fibrinogen

Fibrils. *Biomacromolecules* **9,** 3258–3267 (2008).

174. Tang, L., Ugarova, T. P., Plow, E. F. & Eaton, J. W. Molecular determinants of acute inflammatory responses to biomaterials. *J. Clin. Invest.* **97,** 1329–1334 (1996).

175. Languino, L. R. *et al.* Fibrinogen mediates leukocyte adhesion to vascular endothelium through an ICAM-1-dependent pathway. *Cell* **73,** 1423–1434 (1993).

176. Herwald, H. *et al.* M Protein, a Classical Bacterial Virulence Determinant, Forms Complexes with Fibrinogen that Induce Vascular Leakage. *Cell* **116,** 367–379 (2004).

177. Flick, M. J. *et al.* Leukocyte engagement of fibrin(ogen) via the integrin receptor αMβ2/Mac-1 is critical for host inflammatory response in vivo. *J. Clin. Invest.* **113,** 1596–1606 (2004).

178. Adams, R. A. *et al.* The fibrin-derived γ377-395peptide inhibits microglia activation and suppresses relapsing paralysis in central nervous system autoimmune disease. *J. Exp. Med.* **204,** 571–582 (2007).

179. Paul, J., Strickland, S. & Melchor, J. P. Fibrin deposition accelerates neurovascular damage and neuroinflammation in mouse models of Alzheimer's disease. *J. Exp. Med.* **204,** 1999–2008 (2007).

180. Davalos, D. *et al.* Fibrinogen-induced perivascular microglial clustering is required for the development of axonal damage in neuroinflammation. *Nat. Commun.* **3,** (2012).

181. Flick, M. J., Du, X. & Degen, J. L. Fibrin(ogen)-αMβ2 Interactions Regulate Leukocyte Function and Innate Immunity In Vivo. *Exp. Biol. Med.* **229,** 1105–1110 (2004).

182. Roy, A., Fung, Y. K., Liu, X. & Pahan, K. Up-regulation of Microglial CD11b Expression by Nitric Oxide. *J. Biol. Chem.* **281,** 14971–14980 (2006).

183. Ischiropoulos, H. & Beckman, J. S. Oxidative stress and nitration in neurodegeneration:

Cause, effect, or association? *J. Clin. Invest.* **111,** 163–169 (2003).

184. Han, E. *et al.* Photopatternable Imaging Layers for Controlling Block Copolymer Microdomain Orientation. *Adv. Mater.* **19,** 4448–4452 (2007).

185. He, G., Dahl, T., Veis, A. & George, A. Nucleation of apatite crystals in vitro by self-assembled dentin matrix protein 1. *Nat. Mater.* **2,** 552–558 (2003).

186. Daniele, S. G., Edwards, A. A. & Maguire-Zeiss, K. A. Isolation of Cortical Microglia with Preserved Immunophenotype and Functionality From Murine Neonates. *J. Vis. Exp.* (2014). doi:10.3791/51005

187. ANDRADE, J. D. & HLADY, V. Plasma Protein Adsorption: The Big Twelve. *Ann. N. Y. Acad. Sci.* **516,** 158–172 (1987).

188. Friedrichs, B. Th. Peters. Jr.: All about Albumin. Biochemistry, Genetics, and Medical Applications. XX and 432 pages, numerous figures and tables. Academic Press, Inc., San Diego, California, 1996. Price: 85.00 US $. *Food / Nahrung* **41,** 382 (1997).

189. Curry, S., Mandelkow, H., Brick, P. & Franks, N. Crystal structure of human serum albumin complexed with fatty acid reveals an asymmetric distribution of binding sites. *Nat. Struct. Biol.* **5,** 827–835 (1998).

190. Carter, D. C. & Ho, J. X. Structure of Serum Albumin. *Lipoproteins, Apolipoproteins, and Lipases* 153–203 (1994). doi:10.1016/s0065-3233(08)60640-3

191. Majorek, K. A. *et al.* Structural and immunologic characterization of bovine, horse, and rabbit serum albumins. *Mol. Immunol.* **52,** 174–182 (2012).

192. Yang, Z., Mochalkin, I., Veerapandian, L., Riley, M. & Doolittle, R. F. Crystal structure of native chicken fibrinogen at 5.5-A resolution. *Proc. Natl. Acad. Sci.* **97,** 3907–3912 (2000).

193. Boulos, S. P. *et al.* Nanoparticle–Protein Interactions: A Thermodynamic and Kinetic Study

of the Adsorption of Bovine Serum Albumin to Gold Nanoparticle Surfaces. *Langmuir* **29,** 14984–14996 (2013).

194. Michel, R., Pasche, S., Textor, M. & Castner, D. G. Influence of PEG Architecture on Protein Adsorption and Conformation. *Langmuir* **21,** 12327–12332 (2005).

195. Yang, Z., Galloway, J. A. & Yu, H. Protein Interactions with Poly(ethylene glycol) Self-Assembled Monolayers on Glass Substrates: Diffusion and Adsorption. *Langmuir* **15,** 8405–8411 (1999).

196. Herrmann, M. *et al.* Fibronectin, Fibrinogen, and Laminin Act as Mediators of Adherence of Clinical Staphylococcal Isolates to Foreign Material. *J. Infect. Dis.* **158,** 693–701 (1988).

197. Heuberger, M., Drobek, T. & Spencer, N. D. Interaction Forces and Morphology of a Protein-Resistant Poly(ethylene glycol) Layer. *Biophys. J.* **88,** 495–504 (2005).

198. Chen, X. *et al.* Recognition of Protein Adsorption onto Polymer Surfaces by Scanning Force Microscopy and Probe−Surface Adhesion Measurements with Protein-Coated Probes. *Langmuir* **13,** 4106–4111 (1997).

199. Szleifer, I. Polymers and proteins: interactions at interfaces. *Curr. Opin. Solid State Mater. Sci.* **2,** 337–344 (1997).

200. Slack, S. M. & Horbett, T. A. The Vroman Effect. *ACS Symposium Series* 112–128 (1995). doi:10.1021/bk-1995-0602.ch008

201. VROMAN, L., ADAMS, A. L., KLINGS, M. & FISCHER, G. Fibrinogen, Globulins, Albumin and Plasma at Interfaces. *Applied Chemistry at Protein Interfaces* 255–289 (1975). doi:10.1021/ba-1975-0145.ch012

202. Hirsh, S. L. *et al.* The Vroman effect: Competitive protein exchange with dynamic multilayer protein aggregates. *Colloids Surfaces B Biointerfaces* **103,** 395–404 (2013).

203. Lau, K. H. A., Bang, J., Hawker, C. J., Dong, H. K. & Knoll, W. Modulation of protein-surface interactions on nanopatterned polymer films. *Biomacromolecules* **10,** 1061–1066 (2009).

204. Leung, B. O., Wang, J., Brash, J. L. & Hitchcock, A. P. Imaging Hydrated Albumin on a Polystyrene−Poly(methyl methacrylate) Blend Surface with X-ray Spectromicroscopy. *Langmuir* **25,** 13332–13335 (2009).

205. Leung, B. O. *et al.* X-ray Spectromicroscopy Study of Protein Adsorption to a Polystyrene−Polylactide Blend. *Biomacromolecules* **10,** 1838–1845 (2009).

206. Poljak, R. J. X-Ray Diffraction Studies of Immunoglobulins. *Advances in Immunology Volume 21* 1–33 (1975). doi:10.1016/s0065-2776(08)60217-5

207. Elgert, K. D. *Immunology: understanding the immune system*. (John Wiley & Sons, 2009).

208. Lassen, B. & Malmsten, M. Competitive Protein Adsorption Studied with TIRF and Ellipsometry. *J. Colloid Interface Sci.* **179,** 470–477 (1996).

209. Schmaier, A. H. *et al.* The effect of high molecular weight kininogen on surface-adsorbed fibrinogen. *Thromb. Res.* **33,** 51–67 (1984).

210. Vilaseca, P., Dawson, K. A. & Franzese, G. Understanding and modulating the competitive surface-adsorption of proteins through coarse-grained molecular dynamics simulations. *Soft Matter* **9,** 6978 (2013).

211. van Oss, C. J. Review of:'The Vroman Effect', C.H. Bamford, S.L. Cooper and T. Tsuruia, eds., VSP Publishers, Utrecht, 1992; hardbound, pp. xii + 191, $55. *J. Dispers. Sci. Technol.* **14,** 396–397 (1993).

212. Joo, J. Y., Amin, M. L., Rajangam, T. & An, S. S. A. Fibrinogen as a promising material for various biomedical applications. *Mol. Cell. Toxicol.* **11,** 1–9 (2015).

213. Knickerbocker, T. & MacBeath, G. Detecting and Quantifying Multiple Proteins in Clinical Samples in High-Throughput Using Antibody Microarrays. *Protein Microarray for Disease Analysis* 3–13 (2011). doi:10.1007/978-1-61779-043-0_1

214. Templin, M. F. *et al.* Protein microarray technology. *Trends Biotechnol.* **20,** 160–166 (2002).

215. Xu, Q. & Lam, K. S. Protein and Chemical Microarrays—Powerful Tools for Proteomics. *J. Biomed. Biotechnol.* **2003,** 257–266 (2003).

216. Day, R. & Daggett, V. Ensemble versus single-molecule protein unfolding. *Proc. Natl. Acad. Sci.* **102,** 13445–13450 (2005).

217. McLoughlin, S. Y., Kastantin, M., Schwartz, D. K. & Kaar, J. L. Single-molecule resolution of protein structure and interfacial dynamics on biomaterial surfaces. *Proc. Natl. Acad. Sci.* **110,** 19396–19401 (2013).

218. Tinoco, I. & Gonzalez, R. L. Biological mechanisms, one molecule at a time. *Genes Dev.* **25,** 1205–1231 (2011).

219. Gray, J. J. The interaction of proteins with solid surfaces. *Curr. Opin. Struct. Biol.* **14,** 110–115 (2004).

220. NAKANISHI, K. *et al.* REVIEW On the Adsorption of Proteins on Solid Surfaces, a Common but Very Complicated Phenomenon. *J. Biosci. Bioeng.* **91,** 233–244 (2001).

221. SZOLLOSI, G., DERENYI, I. & VOROS, J. Reversible mesoscopic model of protein adsorption: From equilibrium to dynamics. *Phys. A Stat. Mech. its Appl.* **343,** 359–375 (2004).

222. Rabe, M., Verdes, D., Zimmermann, J. & Seeger, S. Surface organization and cooperativity during nonspecific protein adsorption events. *J. Phys. Chem. B* **112,** 13971–13980 (2008).

223. Minton, A. P. Effects of Excluded Surface Area and Adsorbate Clustering on Surface

Adsorption of Proteins. II. Kinetic Models. *Biophys. J.* **80,** 1641–1648 (2001).

224. Mulheran, P. A., Pellenc, D., Bennett, R. A., Green, R. J. & Sperrin, M. Mechanisms and Dynamics of Protein Clustering on a Solid Surface. *Phys. Rev. Lett.* **100,** (2008).

225. McGuire, J., Wahlgren, M. C. & Arnebrant, T. Structural Stability Effects on the Adsorption and Dodecyltrimethylammonium Bromide-Mediated Elutability of Bacteriophage T4 Lysozyme at Silica Surfaces. *J. Colloid Interface Sci.* **170,** 182–192 (1995).

226. Nygren, H., Alaeddin, S., Lundström, I. & Magnusson, K.-E. Effect of surface wettability on protein adsorption and lateral diffusion. Analysis of data and a statistical model. *Biophys. Chem.* **49,** 263–272 (1994).

227. Bolt, P. S., Goodwin, J. W. & Ottewill, R. H. Studies on the Preparation and Characterization of Monodisperse Polystyrene Latices. VI. Preparation of Zwitterionic Latices†. *Langmuir* **21,** 9911–9916 (2005).

228. Beattie, J. K. The intrinsic charge on hydrophobic microfluidic substrates. *Lab Chip* **6,** 1409 (2006).

229. Frenkel, D. & Smit, B. Molecular Dynamics Simulations. *Understanding Molecular Simulation* 63–107 (2002). doi:10.1016/b978-012267351-1/50006-7

230. Schwenke, K. & Del Gado, E. Soft repulsive interactions, particle rearrangements and size selection in the self-assembly of nanoparticles at liquid interfaces. *Faraday Discuss.* **181,** 261–280 (2015).

231. Schwenke, K., Isa, L. & Del Gado, E. Assembly of Nanoparticles at Liquid Interfaces: Crowding and Ordering. *Langmuir* **30,** 3069–3074 (2014).